8-2022

Multi-Scale Vertebral-Kinematics Based Simulation Pipeline of the Human Spine With Application to Spine Tissues Analysis

Mohd Jaradat
mjarada@clemson.edu

MULTI-SCALE VERTEBRAL-KINEMATICS BASED SIMULATION PIPELINE OF THE HUMAN SPINE WITH APPLICATION TO SPINE TISSUES ANALYSIS

A Dissertation
Presented to
the Graduate School of
Clemson University

In Partial Fulfillment
of the Requirements for the Degree
Doctor of Philosophy
Bioengineering

---

by
Mohd G. Jaradat
August 2022

Accepted by:
Dr. Melinda K. Harman, Committee Chair
Dr. Hai Yao
Dr. Jeremy Mercuri
Dr. Timothy McHenry

ABSTRACT

Vertebral kinematics, or the relative motion between vertebrae due to muscle contractions and other loading conditions, are the physical cause of stresses and deformations in spine tissues. Abnormal vertebral kinematics contribute to clinical instability and altered intervertebral disc pressure. In the presence of spinal stenosis, or narrowing of the spinal canal, it is suspected that abnormal kinematics can contribute to injury or compression of the spinal cord. These conditions are underlying factors in the 15% to 45% annual prevalence of low back pain. While medical imaging is commonly used to assess overall spine alignment and detect clinical instability and stenosis in static postures, *in vivo* measurement of vertebral kinematics during dynamic motion is difficult and alternative approaches are needed.

Computational simulations based on musculoskeletal dynamics (MSD) and finite element (FE) modeling are widely used to understand the biomechanics of human movement and their role in musculoskeletal injuries and disorders. This dissertation addresses the technical gap that simulations of body-level motions have proven inadequate for understanding organ-level behavior of the spine, such as individual vertebral kinematics and intervertebral disc pressure, or predicting stenosis risks.

The broad objective of this dissertation is to develop an analytical tool for understanding spine tissues' behavior in response to vertebral kinematics and spine pathology over a range of body postures. It proposes a novel pipeline of computational models based on the prediction of individual vertebral kinematics from measurable body-level motions, using MSD simulations to drive the vertebrae in corresponding organ-level spine FE models. This work accomplished the following three aims.

In Aim 1, a reformulated elastic surface node (ESN) lumbar MSD model is developed for use in MSD simulations. The ESN MSD model modifies the lumbar spine within an existing MSD model by removing non-physiological kinematic constraints and including elastic intervertebral disc behavior. The ESN MSD model was scaled using subject-specific anthropometrics and validated to predict *in vivo* vertebral kinematics and intervertebral disc pressures in the lumbar spine during trunk flexion/extension.

In Aim 2, the subject-specific ESN MSD model of the lumbar spine is integrated into a novel simulation pipeline that automatically maps it to a kinematics-driven FE model (KD-FEM). The KD-FEM consists of the lumbar vertebrae that are scaled to the subject-specific geometries and actuated by the subject-specific vertebral kinematics from the ESN MSD model for different activities. The simulation pipeline is validated for its ability to predict *in vivo*, subject-specific intervertebral disc pressures at the L_4L_5 vertebral level during flexion motion and load carrying postures.

In Aim 3, a detailed multi-layered multi-phase lumbar canal FE model is integrated into the KD-FEM to quantify risks to spinal canal tissues due to vertebral kinematics and progressive canal narrowing (stenosis). This approach enables distinct computation of proposed stenosis measures, including cerebrospinal fluid pressure, cauda equina deformation and related stresses/pressure/strains, among others. Model outputs include stenosis measures during trunk flexion motion and comparison of three clinically relevant degrees of progressive stenosis of the bony vertebral foramen at the L_4 level.

The simulation pipeline developed in this dissertation is intended to be coupled with traditional symptoms-based clinical assessments. The broader innovation is its potential for

identifying biomechanical factors contributing to clinical instability, abnormal intervertebral disc pressures, and risks due to abnormal vertebral kinematics and progressive stenosis.

ACKNOWLEDGMENTS

I would like to acknowledge Dr. Melinda Harman, my advisor, for being my mentor and advocate in my research and beyond. I acknowledge her providing the appropriate environment for research success through continuous support and dedication. I would like to thank my committee members, Dr. Hai Yao, Dr. Jeremy Mercuri, and Dr. Timothy McHenry for their care, support, and offering their expertise for my research.

TABLE OF CONTENTS

Page

Table of Contents (Continued)

Page

LIST OF TABLES

LIST OF FIGURES

List of Figures (Continued)

Figure Page

List of Figures (Continued)

Figure Page

List of Figures (Continued)

Figure Page

CHAPTER ONE

INTRODUCTION AND REASEARCH AIMS

Vertebral kinematics (VKS), or the relative motion between vertebrae due to muscle contractions and other loading conditions, are the physical cause of stresses and deformations in spine tissues. Abnormal VKS contribute to clinical instability and altered intervertebral disc (IVD) pressure, which is a known feature in subjects with disc degeneration. In the presence of spinal stenosis, or narrowing of the spinal canal, it is suspected that abnormal kinematics can contribute to injury or compression of the spinal cord. These conditions are underlying factors in the 15% to 45% annual prevalence of low back pain and spinal canal issues. While medical imaging is commonly used to assess overall spine alignment and detect clinical instability and stenosis in static postures, *in vivo* measurement of VKS during dynamic motion is difficult. However, such approaches for measuring VKS are not widely used clinically, and common medical imaging systems only capture spinal postures in the imaging field, which limits the types of motions that can be analyzed. Alternative approaches for computing individual VKS during dynamic body-level motions are needed to identify biomechanical factors contributing to clinical instability, abnormal IVD pressures, and risks due to abnormal VKS and progressive stenosis.

Computational simulations based on musculoskeletal dynamics (MSD) and finite element (FE) modeling are widely used to understand the biomechanics of human movement and their role in musculoskeletal injuries and disorders. In general, MSD systems combine quantitative body-level motions and external loads that provide an indirect approach for assessing organ-level biomechanics that are otherwise difficult to measure. FE models assess organ-level biomechanics by combining isolated body segments with detailed material properties of tissues under controlled load and motion conditions. MSD systems implement rigid-body dynamics to non-invasively and

reliably estimate internal loads for individual body segments. However, applying computational simulations to spine biomechanics is challenging. Realistic load and motion conditions are difficult to apply and algorithms in computational simulations rely on simplified representations of spinal tissues and vertebral loads and motions. For example, algorithms in MSD systems necessarily rely on kinematic constraints between vertebrae to minimize soft tissue artifacts and other discontinuities and are generally formulated for describing overall body postures and organ-level kinematics. Such approaches have proven inadequate for understanding organ-level behavior of the spine. There is urgent need for alternative computational approaches that enable more realistic VKS and IVD pressure computations in MSD simulations.

Broad Objectives and Specific Aims

This dissertation addresses the technical gap that simulations of body-level motions have proven inadequate for understanding organ-level behavior of the spine, such as individual VKS and IVD pressure, or predicting stenosis risks. The broad objective of this dissertation research is to develop an analytical tool for understanding spine tissues' behavior in response to VKS and spine pathology over a range of body postures. It proposes a novel pipeline of computational models based on the prediction of individual VKS from measurable body-level motions, using MSD simulations to drive the vertebrae in corresponding spine FE models. This objective was achieved by accomplishing the following three aims.

Aim 1

In Aim 1, a reformulated elastic surface node (ESN) lumbar model is developed for use in MSD simulations. The MSD ESN model will modify the lumbar spine in an existing MSD model by removing non-physiological kinematic constraints and including elastic IVD behavior. Two lumbar spine models will be compared: i) the default joint and rhythm (DJR) MSD model that is

included in the standard full-body MSD model; and ii) the ESN MSD model that was reformulated from the DJR MSD model to address the technical parameters limiting VKS and IVD pressure calculations. Both the DJR and ESN MSD models will be scaled using subject-specific anthropometrics and will be validated to predict published *in vivo* VKS and IVD pressures in the lumbar spine during trunk flexion/extension. The reformulated ESN MSD lumbar spine model will support prediction of VKS and IVD pressures during dynamic motion and has potential for identifying biomechanical factors contributing to abnormal IVD pressures and clinical instability.

Aim 2

In Aim 2, the subject-specific ESN MSD model of the lumbar spine is integrated into a novel simulation pipeline that automatically maps it to a kinematics-driven FE model (KD-FEM). The KD-FEM consists of the lumbar vertebrae that are scaled to the subject-specific geometries and actuated by the subject-specific vertebral kinematics from the ESN MSD model for different activities. The work in Aim 2 will utilize the ESN MSD model and the predicted individual VKS and IVD pressure in spine soft tissue FE modeling to further understanding of the tissues' behavior during motion. The key outcome of this work will be to establish a novel pipeline of simulations, 3D modeling, and scripting tools, to automatically map the subject-specific ESN MSD lumbar model into an equivalent kinematics-driven FE model (KD-FEM). The KD-FEM will consist of the lumbar vertebrae that are scaled to the subject-specific geometries and actuated by the individual VKS from the ESN MSD model for different activities. This approach is in contrast with the common methods of assessing spine tissues behavior using load-driven FE models. The simulation pipeline will be validated for its ability to predict *in vivo*, subject-specific IVD pressures at the L4-L5 vertebral level during flexion motion and load carrying postures. That is, IVD pressures calculated in the subject-specific KD-FEM combined with the ESN MSD lumbar spine

model developed in Aim 1 will be compared to: i) *in vivo* IVD pressure measurements from a published study; and ii) IVD pressure calculations from a subject-specific default MSD model that includes body-level motion inputs from an *in vivo* motion capture study of different activities.

Aim 3

In Aim 3, a detailed multi-layered multi-phase lumbar canal FE model is integrated into the KD-FEM to quantify risks to spinal canal tissues due to VKS and progressive canal narrowing (stenosis). This approach contrasts with commonly oversimplified canal models in literature. This approach will enable distinct computation of proposed stenosis measures: cerebrospinal fluid pressure, cauda equina deformation and related stresses/pressure/strains, and dura-equina contact, Model outputs will include the stenosis measures during trunk flexion motion and comparison of three clinically relevant degrees of progressive stenosis of the bony vertebral foramen at the L_4 level.

The technical aspects of this dissertation will present a versatile computational modeling tool that provides an alternative approach for computing individual VKS during dynamic body-level motions. It will generate analytical assessments representing spine soft tissue pathology and will enable dynamic quantification of risks during motion. It will validate the use of MSD systems for computing realistic VKS from body-level motions, using them to actuate FE models of the lumbar spine, and capturing the impact of pathological conditions like progressive stenosis. In future work, algorithms representing specific tissues can be embedded into the KD-FEM pipeline, such as IVD models or detailed canal geometry, which will function as an independent approach for evaluating those models under load and motion conditions with realistic VKS.

The broader innovation of this dissertation is its potential for identifying biomechanical factors contributing to clinical instability, abnormal intervertebral disc pressures, and risks due to

abnormal vertebral kinematics and progressive stenosis. The simulation pipeline is intended to be coupled with traditional symptoms-based clinical assessments. In future work, the simulation pipeline can be generalized for a larger variety of body types and daily activities and validated for robust application in a clinical work frame. Implementation would require only minimal patient inputs of simple anthropometrics measurements, rudimentary vertebral geometries from available clinical radiographs or MRI scans, and simple motion captured postures or ranges of motion. In this manner, it has potential to aid patient education related to activity precautions and support decisions for treatment options.

CHAPTER TWO

PREDICTING UNCONSTRAINED VERTEBRAL KINEMATICS IN MUSCULOSKELETAL DYNAMICS SIMULATIONS FROM BODY-LEVEL EXTENSION-FLEXTION MOTION: VALIDATION OF A REFORMULATED LUMBAR SPINE MODEL

Introduction

Vertebral kinematics (VKS), or the relative motion between vertebrae due to muscle contractions and other loading conditions, are the physical cause of stresses and deformations in spine tissues. Abnormal VKS in the lumbar spine contribute to clinical instability and both conditions are underlying factors in the 15% to 45% annual prevalence of low back pain (Manchikanti et al., 2009; Panjabi et al., 2003). In addition, abnormal VKS are linked to altered intervertebral disc (IVD) pressure (Cunningham et al., 1997; Schmoelz et al., 2006), which is a known feature in subjects with disc degeneration (Sato et al., 1999).

While flexion-extension radiographs are commonly used to assess overall spine alignment and detect clinical instability, *in vivo* measurement of VKS during dynamic motion is difficult. VKS can be measured using medical imaging, such as dual-plane fluoroscopy or magnetic resonance imaging, combined with computational image processing or modeling techniques (Aiyangar et al., 2014; Anderst et al., 2016; Cheng et al., 2016; Fujii et al., 2007; Kaneoka et al., 1999; Li et al., 2009; Lin et al., 2014; Staub et al., 2015; Wang et al., 2009; Wang et al., 2011; Wang et al., 2020; Yeager et al., 2013). However, such approaches are not widely used clinically, and common medical imaging systems only capture spinal postures in the imaging field, which limits the types of motions that can be analyzed. Alternative approaches for computing VKS during dynamic body-level motions are needed to identify biomechanical factors contributing to abnormal IVD pressures and clinical instability.

Musculoskeletal dynamics (MSD) simulations are widely used to understand the biomechanics of human movement and their role in musculoskeletal injuries and disorders (Drake et al., 2006; El-Rich et al., 2004; Grujicic et al., 2010; Han et al., 2012; Raabe et al., 2016; Stambolian et al., 2016; Tae Soo et al., 2010). For example, the AnyBody Modeling System (Damsguaard et al., 2006) and OpenSim (Delp et al., 2007) are well-documented script-based mathematical MSD systems that implement rigid-body dynamics to estimate internal loads that are otherwise difficult to measure for individual body segments from kinematics inputs. When combined with marker-based motion capture systems measuring body-level motions and external body loads, these MSD systems provide an indirect approach to non-invasively assess the average loads on individual body segments (Bassani et al., 2017; Alemi et al., 2021). However, algorithms in MSD systems necessarily rely on non-realistic kinematic constraints between articulating segments to minimize soft tissue artifacts and other discontinuities (Hicks et al., 2015) and are generally formulated for describing overall body postures and organ-level kinematics (e.g. lumbar spine) rather than predicting realistic individual VKS (Alemi et al., 2021).

Alternative approaches are needed to enable more realistic VKS and IVD pressure predictions in MSD simulations. Existing algorithms in the Anybody Modeling System use spherical joints connecting rigid vertebrae segments and spinal rhythm definitions (Arshad et al., 2016), which non-physiologically constrain vertebral translation and define VKS as a function of the organ-level lumbar spine motion, that is, the thorax-pelvis rotation input at the thorax anatomical frame. In this manner, relative intervertebral motions in the spinal units are prescribed inputs into the system rather than computed results determined from the behavior of muscles, ligaments, IVD stiffness, and other physiological parameters. The spherical joint does not replicate physiological load bearing through the upper and lower surfaces of the vertebrae endplate surfaces

and its definition lacks the IVD stiffness that has direct influence on the VKS and IVD pressures. Reformulating the lumbar spine model to overcome these limiting technical parameters will support prediction of VKS and IVD pressures during dynamic motion and has potential for identifying biomechanical factors contributing to abnormal IVD pressures and clinical instability.

The purpose of the current study was to develop and validate a reformulated spine model for predicting VKS and IVD pressures in the lumbar spine during trunk flexion/extension in MSD simulations. Two lumbar spine models were compared: i) the default joint and rhythm (DJR) MSD model that is included in the standard full-body MSD model available through the AnyBody Managed Model Repository; and ii) the elastic surface node (ESN) model that was reformulated in the current study from the DJR MSD model to address technical parameters limiting VKS and IVD pressure calculations. Both the DJR and ESN MSD models were scaled using subject-specific anthropometrics reported by Wilke et al. (1999; 2001). Calculated IVD pressures were validated against subject-specific *in vivo* IVD pressure measurements published by Wilke et al. (1999; 2001) and calculated IVD pressures reported by Bassani et al. (2017) for trunk flexion-extension. Calculated VKS were validated using the *in vivo* sagittal plane rotations of individual lumbar vertebrae ($L_1 - Sacrum$) reported by Wong et al. (2006), Alemi, et al. (2021) and Rozumalski et al. (2008). Calculated compressive and shear loads in L_4L_5 unit were compared with previous models reported by Arshad et al. (2016) that use the subject-specific anthropometrics of Wilke et al. (1999; 2001).

Methods

This study used the standard MSD human body model available through the AnyBody Managed Model Repository (©2020 AnyBody Technology A/S, Aalborg, Denmark). The full-body MSD model contains over 100 rigid bone segments constrained by joints assigned different

degrees of freedom and stiffness and over 900 muscles. The full-body MSD model establishes mechanical equilibrium mathematically using inverse dynamics and optimization to calculate muscle forces by minimizing muscle recruitment activation as demanded by movement between sequential poses (Damsgaard et al., 2006; Rasmussen et al., 2001). Individual body segments (e.g., legs, arms, trunk) for the full-body MSD model were assembled in the AnyBody framework, initially assigned default parameters and standard scaling to the 50th percentile sizes for a European male (Rasmussen et al., 2005), and posed in a standing position.

Default Joint and Rhythm (DJR) MSD Spine Model

The DJR MSD spine model is part of the full-body MSD model, consisting of a cervical spine model (7 articulated vertebrae and 136 muscle fascicles), a thoracic spine model is modeled as a single lumped segment starting from T_1 to T_{12}, and an enhanced lumbar spine model (5 articulated vertebrae and 188 muscle fascicles) that included lumbar spine ligaments and facet joints. This DJR MSD spine model has been described in detail (De Zee et al., 2007; Ignasiak et al., 2016) and validated for the trunk flexion/extension activity used in the current study (Arshad et al., 2016; Han et al., 2012). However, it includes the following modeling assumptions and constraints that limit its use for realistic VKS predictions.

Spherical joint constraints:

Each spinal unit in the DJR MSD spine model includes a spherical joint defined by two nodes rigidly connected to the opposing vertebrae segments (Fig. 2.1). The spherical joint constrains the two nodes to be coincident during motion through a non-physiological reaction force $\vec{F}_J$ between the nodes, which is defined as the force vector the lower node exerts on the upper node measured from the lower node's frame.

This constrains the relative intervertebral translation in each spinal unit to a rigid 3 degrees of freedom rotation about the joint node and constrains the vertebral center of rotation to the node. Each node has an internally defined coordinate system (C-sys) frame associated with it to represent the motion of a given spinal unit, with the general C-sys convention orienting the positive x-axis in the anterior direction, the positive y-axis in the superior direction, and the positive z-axis in the lateral direction. The term "node rotation" refers to the rotation of the C-sys frame and the term "joint rotation" refers to the rotation of the upper joint node measured with respect to the lower joint node (Fig. 2.1). The joint rotation matrix $\overline{\overline{M}}$ was defined as a rotation vector $\vec{R}$ using the system function RotVector

$$\vec{R} = \theta\, \vec{u}_R \tag{2.1}$$

where the rotation angle θ represents the rotation angle about a rotation axis unit vector $\vec{u}_R$, which is an eigenvector of the rotation matrix corresponding to the eigenvalue of 1. This rotation vector can be determined from the rotation matrix $\overline{\overline{M}}$ of the joint. While this approach is a good approximation for joint load calculations, it is non-physiological (White et al., 1978) because it constrains the translations and rotations of the given spinal unit and lacks the definition of elastic behavior of the IVD in either translation or rotation between the vertebrae.

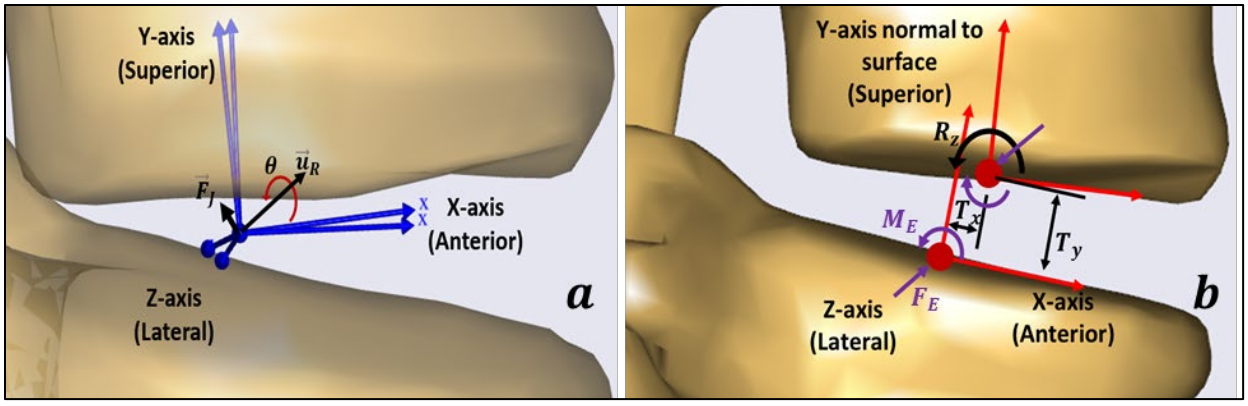

Fig. 2.1a. Spinal units in the DJR MSD model include the spherical joint's two coincident nodes, their local C-sys frames, joint rotation's rotation vector and angle, and joint reaction force. **Fig. 2.1b.** Spinal units in the ESN MSD model include surface nodes at endplates centers, their surface-aligned C-sys frames (in red), spinal unit VKS measures definitions (in black), and stiffness forces and moments (in purple).

Spinal rhythm prescribing the joint rotations:

The DJR MSD spine model defined a kinematic driver, that is the spinal rhythm, to prescribe the joint rotation vectors $\vec{R}$ for each lumbar spinal unit as a fixed percentage of the rotation vector $\vec{R}_{J_{T12}\,J_1}$ of $T_{12}L_1$ spinal unit (Table 2.1). Mathematically, for example in the L_4L_5 spinal unit, the rotation vector was prescribed as

$$\vec{R}_{J_4J_5} = \left(0.40205\, R_{J_{T12}\,J_1\,X},\ 0.3132395\, R_{J_{T12}\,J_1\,Y},\ 0.40205\, R_{J_{T12}\,J_1\,Z}\right) \tag{2.2}$$

Table 2.1
Spinal rhythm: Spinal units' rotation vector ratios of $T_{12}L_1$ unit rotation

Spinal unit	$\vec{R}_{J_{T12}J_1\,X}$	$\vec{R}_{J_{T12}J_1\,Y}$	$\vec{R}_{J_{T12}J_1\,Z}$
$\vec{R}_{J_{T12}J_1}$	1	1	1
$\vec{R}_{J_1J_2}$	0.9131695	0.8263391	0.9131695
$\vec{R}_{J_2J_3}$	0.7462112	0.6660833	0.7462112
$\vec{R}_{J_3J_4}$	0.5784718	0.4908604	0.5784718
$\vec{R}_{J_4J_5}$	0.4020500	0.3132395	0.4020500
$\vec{R}_{J_5J_{Sacrum}}$	0.2276759	0.1421123	0.2276759
$\vec{R}_{Sacrum}$ $_{Pelvis}$	0.0710562	0	0.0710562

Thorax-pelvis rotation inputs and the continuity constraint:

The MSD system actuates flexion-extension motion of the DJR MSD lumbar spine model using the rotational motion between the thoracolumbar joint and pelvis segment as input. The thorax-pelvis rotation vector $\vec{R}_{A_{Thorax}A_{Pelvis}}$ defined this motion as the rotation of the anatomical frame rigidly connected to the rigid thorax spine segment relative to the pelvis anatomical frame (Fig. 2.2). Additionally, the MSD system internally defined the necessary continuity constraint enforcing that all lumbar joints' rotations, starting from the pelvis anatomical frame, accumulate to the total thorax-pelvis rotation. The thorax-pelvis rotation matrix can be mathematically expressed in terms of the rotation matrices of each spinal unit as

$$\bar{\bar{M}}_{A_{Thorax}A_{Pelvis}} = \bar{\bar{M}}_{A_{Pelvis}} * \bar{\bar{M}}_{J_{Pelvis}A_{Pelvis}} * \bar{\bar{M}}_{J_{Sacrum}J_{Pelvis}} * \bar{\bar{M}}_{J_5J_{Sacrum}} * \bar{\bar{M}}_{J_4J_5} * \bar{\bar{M}}_{J_3J_4} * \bar{\bar{M}}_{J_2J_3} * \bar{\bar{M}}_{J_1J_2} * \bar{\bar{M}}_{J_{T12}J_1} * \bar{\bar{M}}_{A_{Thorax}J_{T12}} \quad (2.3)$$

where $\bar{\bar{M}}_{J_{Pelvis}A_{Pelvis}}$ is the rotation matrix between the pelvis joint node J_{Pelvis} in the pelvis-sacrum spinal unit and the pelvis anatomical frame (A_{Pelvis}), $\bar{\bar{M}}_{A_{Thorax}J_{T12}}$ is the rotation matrix between the thorax anatomical frame (A_{Thorax}) and T_{12} joint node J_{T12} in $T_{12}L_1$ unit, and $\bar{\bar{M}}_{A_{Pelvis}}$ equals the identity matrix ($\bar{\bar{M}}_{A_{Pelvis}} = I$). Anybody software uses rotation vector formulation $\vec{R}$ rather than the general matrix form in Eq. 2.3 despite that the vector summation of the rotation vectors is invalid due to the sequence of rotation issue. It is concluded from the rhythm and continuity constraints that the lumbar joint rotations are prescribed inputs into the system rather than computational results determined from the role of muscles, ligaments, inertias, and IVD stiffness.

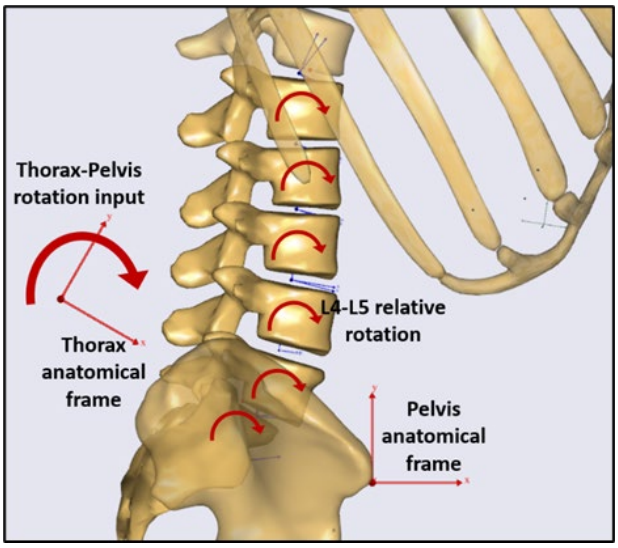

Fig. 2.2. The thorax-pelvis rotation between thorax anatomic frame and pelvis anatomic frame and the continuity sum constraint in the DJR MSD model

Default solvers and the DJR equilibrium configuration:

Using formulations from rigid-body dynamics and the necessary constraints described in the previous sections, the MSD system defines two default solvers: the kinematics solver and the inverse dynamics solver. The kinematics solver determines relative vertebral kinematics in the spinal units, hereafter DJR VKS, using body-level kinematics input, specifically the thorax-pelvis rotation vector $\vec{R}_{A_{Thorax}A_{Pelvis}}$.

This solver determines the DJR VKS using the kinematics imposed by the default joint and rhythm, DJR, constraints. The inverse dynamics solver determines the loads on each individual vertebrae that are the joint reactions, inertias, muscles, and ligaments' forces and moments using the DJR VKS and the anthropometrics. The inverse dynamics solver uses optimization to solve for these DJR loads because the problem is statically indeterminate, with the number of unknown forces and moments acting on each vertebra is larger than the number of equilibrium equations. The solver minimizes the sum of all muscles' activities, which are the ratio of the current load to

the full-strength load of each muscle, as the cost function while including the equilibrium equations of the vertebrae as mathematical constraints. The resulting solutions from these two solvers, namely the DJR VKS and DJR loads define the DJR equilibrium configuration as having the joint reactions in static (or dynamic) equilibrium with the vertebral loads while excluding any elastic behavior in the joints or spinal units.

Elastic Surface Node (ESN) Spine Model

The ESN MSD spine model was developed by reformulating the existing DJR MSD spine model to remove constraints necessary for rigid-body dynamics and enable elastic behavior in the spinal units. Theoretically, removal of the DJR constraints and application of appropriate stiffness forces and moments will enable a new elastic equilibrium configuration that is different from the DJR MSD model. That is, the IVD stiffness forces and moments should support the spinal unit and be in equilibrium with the internal vertebral loads generated by the muscles, ligaments and inertias. However, this new elastic configuration cannot be determined by the kinematic and inverse-dynamics solvers because they are based on the rigid-body dynamics and the DJR kinematics constraints described in the previous sections (spherical joint constraints, spinal rhythm rotations, and continuity constraint).

Therefore, reformulation for the ESN MSD spine model to support an elastic equilibrium configuration includes removing the constraints imposed by the spherical joints and spinal rhythm definition, redefining VKS based on novel vertebral endplate surface nodes, mathematically representing IVD stiffness between adjacent vertebral endplate surfaces, and implementing a force-dependent-kinematics (FDK) solver combined with a novel kinematic driver formulated based on the surface nodes (hereafter, SN driver).

Deactivation of the default spherical joint constraints and spinal rhythm definition:

The default spherical joint constraints were deactivated in the Anybody software by setting the constraint type to *Soft* in the joints' definitions to allow the SN driver to overwrite them. This caused the model to be kinematically over determined; therefore, the over-determinate kinematic solver was used. The spinal rhythm definition was deactivated by setting its definition to *OFF* in the main file.

Endplate surface nodes and their VKS measures:

In the vertebrae segments' definitions in the Anybody software, the modeling tool **AnyRefNode** was used to create rigidly connected nodes and associated C-sys frames on the geometric center of the endplates' surfaces for all lumbar spine units (Fig. 2.1b). These endplate surface nodes enabled definition, and measuring, of VKS in each spinal unit as the translation vector $\vec{T}$ and the rotation vector $\vec{R}$ of the upper surface node's C-sys frame measured from the lower surface nodes' C-sys frame. The Anybody software measure tool **AnyKinLinear** was used to measure $\vec{T}$ and **AnyKinRotational** with the rotation vector measuring option 'RotVector' was used to measure $\vec{R}$ (Fig. 2.1b).

IVD elastic stiffness between the surface nodes:

The stiffness forces and moments were applied in opposite directions between the surface nodes of the lumbar spinal units using the force modeling tool **AnyForce**. The VKS measures of the translation vector $\vec{T}$ and the rotation vector $\vec{R}$ were referenced in the tool definition. The force tool applied a force vector $\vec{F}_E$ and a moment vector $\vec{M}_E$ to both of the surface nodes proportional to the VKS measures' magnitudes (Fig. 2.1b), which is applied relative to the lower surface node frame corresponding to the VKS measures' convention. The force vector $\vec{F}_E$ was determined by

multiplying each component of $\vec{T}$ by the corresponding translational stiffness function E_i in that component's direction (compression, lateral, anterior, and posterior shear), represented as

$$\vec{F}_E = \left(E_{ant\ shear}\ or\ E_{post\ shear}\right) T_X\ \vec{\imath} + E_{comp}\ T_Y\ \vec{\jmath} + E_{lat\ shear}\ T_Z\ \vec{k}. \quad (2.4)$$

The translational stiffness functions were polynomials fit from published data (Weisse et al., 2012) (Table 2.2) as functions of $\vec{T}$ components, implemented using the **AnyFunPolynomial** tool. The moment vector $\vec{M}_E$ was determined by multiplying each component of $\vec{R}$ by the corresponding rotational stiffness function M_i in that component's direction (lateral bending, axial rotation, extension, and flexion), represented as

$$\vec{M}_E = M_{lat}R_X\ \vec{\imath} + M_{axial}R_Y\ \vec{\jmath} + \left(M_{ext}R_Z\ or\ M_{flex}R_Z\right)\vec{k} \quad (2.5)$$

The rotational stiffness functions were polynomials fit from published data (Heuer et al., 2007) (Table 2.2) as functions of the $\vec{R}$ components. The computed stiffness forces and moments were made negative (multiplied by -1) to resist relative vertebral motions. The Anybody software conditional function tool **iffun** was used to distinguish between the anterior or posterior shear forces, and the flexion or extension moments. The formulated stiffness functions represented the IVD behavior in the unloaded state by including the zero-force IVD heights from a published *in vitro* study (Mirab et al., 2017). The zero-shear forces were assumed at zero T_X and T_Z distances, and the zero-moment IVD rotations at zero rotations. These formulations were applied to all lumbar spinal units.

Table 2.2
The ESN MSD model applied non-linear stiffness functions and compressive zero-load IVD heights between the surface nodes

	Non-linear stiffness polynomial fit (θ in degrees)					
Flexion (N.m) $\theta_Z = -ve$	$M_{flex} = 0.1885 - 0.1876\,\theta_Z + 0.163\,\theta_Z^2$					
Extension (N.m) $\theta_Z = +ve$	$M_{ext} = 0.0296 - 0.9036\,\theta_Z - 0.229\,\theta_Z^2$					
Axial rotation (N.m)	$M_{axial} = -2.5569\,\theta_Y - 0.02899\,\theta_Y^3$					
Lateral bending (N.m)	$M_{lat} = -0.76169\,\theta_X - 0.024036\,\theta_X^3$					
Compressive stiffness (N/m)	$E_{comp} = 4.0 \times 10^5 - 3.92 \times 10^8\,T_Y + 2.455 \times 10^{12}\,T_Y^2$					
Anterior shear stiffness (N/m)	$E_{ant\,shear} = 3.45 \times 10^5 + 2.005 \times 10^8\,T_X - 6.0942 \times 10^9\,T_X^2$					
Posterior shear stiffness (N/m)	$E_{post\,shear} = 6.8 \times 10^4 + 1.325 \times 10^8\,T_X + 7.8125 \times 10^9\,T_X^2$					
Lateral shear stiffness (N/m)	$E_{lat\,shear} = 1.11 \times 10^5 + 4.235 \times 10^8\,T_Z - 7.41 \times 10^{10}\,T_Z^2$					
Zero-load IVD heights (m)	$L_5Sacrum$	L_4L_5	L_3L_4	L_2L_3	L_1L_2	$T_{12}L_1$
	0.00896	0.00736	0.00906	0.00868	0.00741	0.00671*

* Estimated magnitude

Force-Dependent-Kinematics (FDK) Solver:

In the ESN MSD spine model, the FDK solver was used to determine the elastic-joint ESN equilibrium configuration, which is different than the DJR equilibrium configuration, at which the elastic potential energy stored in the elastic joint is minimum. The FDK solver determines minimum potential energy configurations by creating an optimization problem that includes the equilibrium equations as mathematical constraints. The FDK solver uses the DJR equilibrium configuration as initial configuration to start solving for the elastic configuration; this DJR configuration is determined by the two default solvers, kinematics and inverse dynamics, using the DJR constraints and kinematics. However, in the reformulated ESN MSD model the DJR constraints were removed and, therefore the DJR equilibrium configuration is indeterminate by the default solvers. A novel kinematic driver was created to solve this problem.

Novel Kinematic Driver:

In general, a kinematic driver is a mathematical tool that prescribes magnitudes to kinematic measures during the simulation. Since the DJR constraints had been removed in the ESN MSD model, mathematical formulations were manually derived to predetermine these DJR kinematics in terms of the surface nodes. A novel kinematic driver, the SN driver, was developed using the mathematical tool **AnyKinEqSimpleDriver** to implement or prescribe these DJR kinematics directly to the FDK solver as the initial configuration.

The DJR kinematics mathematical formulations were manually derived in the form of the joint rotation angles in terms of the thorax-pelvis extension-flexion input rotation. These formulations were then used to formulate the DJR kinematics in terms of the novel surface nodes' translations and rotations. The joint rotation angles were formulated using the continuity constraint equation, Eq. 2.3, that can take the form of angle-summation for extension-flexion motion. This is due to that the Z-axes of all frames are initially and remain aligned during pure the Z-rotation; therefore, all the rotation vectors in lumbar spine can take the form of $\vec{R} = (0, 0, \theta_Z)$. The continuity constraint between J_{T12} and J_{Pelvis} C-sys frames can take the angle-summation form

$$\theta_{J_{T12}J_{Pelvis}\,Z} = \theta_{J_{Sacrum}J_{Pelvis}\,Z} + \theta_{J_5J_{Sacrum}\,Z} + \theta_{J_4J_5\,Z} + \theta_{J_3J_4\,Z} + \theta_{J_2J_3\,Z} + \theta_{J_1J_2\,Z} + \theta_{J_{T12}J_1\,Z} = 3.93863456\,\theta_{T_{12}L_1\,Z} \quad (2.6)$$

where the rhythm constraint equations in the Z-direction (Table 2.1) were used to express the rotations in terms of $\theta_{T_{12}L_1\,Z}$. Similarly, the thorax-pelvis input can be written as

$$\vec{R}_{A_{Thorax}A_{Pelvis}} = (0, 0, \theta_{A_{Thorax}A_{Pelvis}\,Z}) \quad (2.7)$$

The rotations $\vec{R}_{A_{Thorax}J_{T12}}$ and $\vec{R}_{J_{Pelvis}A_{Pelvis}}$ are constants ((0.0, 0.0, 0.1369624) and (0.0, 0.0, 0.1161103 rad), respectively), as subject-specific invariants because they are on the same

vertebrae. They were premeasured as model parameters and input to the system. Therefore, the continuity constraint between A_{Thorax} and A_{Pelvis} frames can take the angle-summation form of

$$\theta_{A_{Thorax}A_{Pelvis}\,Z} = \theta_{J_{T12}J_{Pelvis}\,Z} + \theta_{A_{Thorax}J_{T12}\,Z} + \theta_{J_{Pelvis}A_{Pelvis}\,Z} = 3.938634560_{J_{T12}J_1\,Z} + \theta_{A_{Thorax}J_{T12}\,Z} + \theta_{J_{Pelvis}A_{Pelvis}\,Z} \quad (2.8)$$

Joint rotation vectors $\vec{R}$ for individual spinal units in the DJR MSD lumbar spine (Table 2.1) were combined with Eq. 2.8 to derive equations defining the joint rotation angle about the Z-axis directly from the thorax-pelvis rotation input. Using the L_4L_5 spinal unit as an example, the relation $\theta_{J_4J_5\,Z} = 0.40205\,\theta_{J_{T12}J_1\,Z}$ and Eq. 2.8 yield the L_4L_5 joint rotation angle about the z-axis as a function of the thorax-pelvis rotation input

$$\theta_{J_4J_5\,Z} = \frac{0.40205}{3.93863456}(\theta_{A_{Thorax}A_{Pelvis}\,Z} - \theta_{A_{Thorax}J_{T12}\,Z} - \theta_{J_{Pelvis}A_{Pelvis}\,Z}) \quad (2.9)$$

Necessary coefficients for the other lumbar joints were similarly calculated (Table 2.3).

Table 2.3
Coefficients for lumbar joints rotations corresponding to Eq. 2.9 and Eq. 2.15

Spinal unit	Coefficients
$\vec{R}_{J_{T12}J_1}$	0.2539
$\vec{R}_{J_1J_2}$	0.2318
$\vec{R}_{J_2J_3}$	0.1895
$\vec{R}_{J_3J_4}$	0.1469
$\vec{R}_{J_4J_5}$	0.1021
$\vec{R}_{J_5J_{Sacrum}}$	0.0578
$\vec{R}_{Sacrum}$ $_{Pelvis}$	0.0180

The translational DJR kinematics were formulated in terms of the surface nodes (SN DJR kinematics); using the example of L_4L_5 spinal unit, the translation vector $\vec{T}_{S_4S_5}$ (Fig. 2.3) of L_4 surface node S_4 measured from S_5 was formulated as

$$\vec{T}_{S_4S_5} = \vec{T}_{J_5S_5} + \vec{T}_{J_4J_5} + \vec{T}_{S_4J_4} * \bar{\bar{M}}_{J_4S_5} \tag{2.10}$$

where $\vec{T}_{J_5S_5}$ is the translation vector of L_5 joint node J_5 measured from S_5, $\vec{T}_{J_4J_5}$ is translation vector of L_4 joint node J_4 measured from J_5, which is zero as the nodes are coincident, and $\vec{T}_{S_4J_4}$ is for S_4 from J_4. The translations $\vec{T}_{J_5S_5}$, $\vec{T}_{S_4J_4}$ are constants, as subject-specific invariants, because they are on the same vertebrae. They were premeasured as model parameters and input to the system.

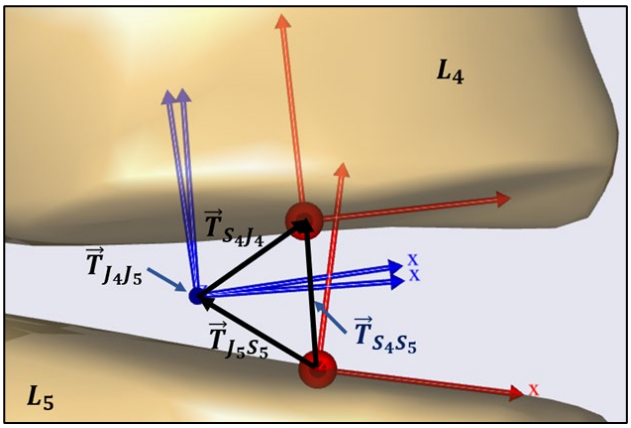

Fig. 2.3. Surface nodes' translation vector (in dark blue) in terms of joint nodes' translation vectors (in black)

The matrix $\bar{\bar{M}}_{J_4S_5}$ is used to transform the vector $\vec{T}_{S_4J_4}$ from J_4 frame to S_5 frame to unify the reference frame for correct vector addition; and is equal to,

$$\bar{\bar{M}}_{J_4S_5} = \bar{\bar{M}}_{J_5S_5} * \bar{\bar{M}}_{J_4J_5} \tag{2.11}$$

where $\bar{\bar{M}}_{J_4J_5}$ is the rotation matrix of J_4 frame measured from J_5 frame and corresponds to the default-joint rotation vector $\vec{R}_{J_4J_5}$. For the pure flexion-extension motion, and using the relation $\theta_{J_4J_5\,Z} = 0.40205\,\theta_{J_{T12}J_1\,Z}$,

$$\bar{\bar{M}}_{J_4J_5} = \begin{bmatrix} \cos(\theta_{J_4J_5\,Z}) & -\sin(\theta_{J_4J_5\,Z}) & 0 \\ \sin(\theta_{J_4J_5\,Z}) & \cos(\theta_{J_4J_5\,Z}) & 0 \\ 0 & 0 & 1 \end{bmatrix} \tag{2.12}$$

where $\bar{\bar{M}}_{J_5S_5}$ is the rotation matrix of J_5 frame measured from S_5 frame, corresponding to $\vec{R}_{J_5S_5}$, which is constant as the frames are on the same vertebra. The rotational DJR kinematics were formulated in terms of the surface nodes; using the example of L_4L_5 spinal unit, the rotation matrix of the upper surface node S_4 measured from S_5 frame is given by

$$\bar{\bar{M}}_{S_4S_5} = \bar{\bar{M}}_{J_5S_5} * \bar{\bar{M}}_{J_4J_5} * \bar{\bar{M}}_{S_4J_4} \tag{2.13}$$

where $\bar{\bar{M}}_{S_4J_4}$ is the rotation matrix of S_4 frame measured from J_4 frame, which is a constant. The matrices $\bar{\bar{M}}_{J_5S_5}$ and $\bar{\bar{M}}_{S_4J_4}$ (similarly in other lumbar joints) are also constants premeasured as subject-specific invariant parameters and input to the system. The rotation vector $\vec{R}_{S_4S_5}$ corresponding to $\bar{\bar{M}}_{S_4S_5}$ can be determined as

$$\vec{R}_{S_4S_5} = \left(0, 0, \theta_{S_4S_5\,Z}\right) = \vec{R}_{J_5S_5} + \vec{R}_{J_4J_5} + \vec{R}_{S_4J_4} = \left(0, 0, \theta_{J_5S_5\,Z}\right) + \left(0, 0, \theta_{J_4J_5\,Z}\right) + \left(0, 0, \theta_{S_4J_4\,Z}\right) \tag{2.14}$$

Using Eq. 2.9,

$$\theta_{S_4S_5\,Z} = \theta_{J_5S_5\,Z} + \frac{0.40205}{3.93863456}\left(\theta_{A_{Thorax}A_{Pelvis}\,Z} - \theta_{A_{Thorax}J_{T12}\,Z} - \theta_{J_{Pelvis}A_{Pelvis}\,Z}\right) + \theta_{S_4J_4\,Z} \tag{2.15}$$

The surface nodes C-sys frames were created aligned with the joint C-sys frames so that

$$\theta_{J_5S_5\,X} = \theta_{J_5S_5\,Y} = 0.0 \tag{2.16}$$

Similar derivations were conducted for the other lumbar units, where the coefficients of the second term in Eq. 2.15 are the same as those listed in Table 2.3. These formulated SN DJR kinematics using the drivers tool member 'DriverPos', and the FDK solver was engaged by setting the constraint-type member 'CType' to the FDK type *ForceDep* for all translation and rotation degrees of freedom (DOF) for lumbar spine units. This allows solving for the elastic behavior for these DOFs simultaneously to capture their mutual effects for lumbar spine. The driver's reaction-type

member ‘Reaction.Type’ was set to *Off* so that no unrealistic rigid reaction forces and moments between the surface nodes get created by the kinematic driver.

The sacrum-pelvis joint has no IVD stiffness and, therefore, no surface nodes were created in this unit. The default joint nodes were used with their default translational and rotational measures referenced in the driver’s definition. The DJR kinematics in terms of the joint nodes were used and the ‘CType’ was set to *Hard* for all the DOFs so that these kinematics are not changed by the FDK solver. For this sacrum-pelvis joint, the ‘Reaction.Type’ members in the driver of the rotational DOF were set to *Off* so that the muscles and ligaments would be responsible for achieving these rotations; while they were set to *On* for the translational DOF so that the joint nodes remain coincident by the reaction forces that the spherical joint creates.

The rotational measure of one of the seven lumbar units must not be included in driver’s definition to avoid over constraining the lumbar spine kinematics because the continuity constraint implicitly determines the rotational kinematics for one of the spinal units. The excluded unit measure can be arbitrary but should not be the sacrum-pelvis unit because there will be no convenient way to specify the *Hard* constraint for this unit.

Model Verification Comparing Model-Predicted IVD Pressures and *in vivo* IVD Pressure Measurements

The DJR and ESN MSD models were scaled using subject-specific anthropometrics and used to calculate IVD pressures in the L_4L_5 unit over a flexion-extension range of motion. The IVD pressures were validated against subject-specific *in vivo* L_4L_5 IVD pressure measurements reported by Wilke et al. (1999; 2001) using a pressure probe inserted in the L_4L_5 disc of a 45-year-old healthy male to measure IVD pressures during trunk flexion-extension. IVD pressures in the DJR MSD model were calculated using the joint reaction force components acting at the spherical

joint nodes normal to the endplate surfaces and the surface area of the *in vivo* measured L_4L_5 IVD. IVD pressures in the ESN MSD model were calculated using the stiffness force components acting at the surface nodes normal to the endplate surface computed using the stiffness functions and the predicted VKS.

Subject-Specific MSD Models:

Subject-specific models were adapted from the standard full-body MSD model available through the AnyBody Managed Model Repository, which has anatomical data corresponding to the 50th percentile size for a European male. The DJR and ESN MSD models were scaled to match the *in vivo* subject anthropometrics as follows.

The subject's height, weight, and fat percentage (70 kg, 173.9 cm, and 11.81%) were used in scaling the model; however, more detailed scaling was created for the segments' lengths using the subject's detailed anatomical landmarks measurements reported by the *in vivo* study, where different segments length (geometric) scaling factors were computed for the different segments. The *in vivo* study landmarks measurements had to be converted to the landmark convention of the MSD system (Table 2.4). The segments' depths and widths were scaled by the same scaling factor computed as

$$\sqrt{\frac{\text{mass scaling factor}}{\text{length (geometric) scaling factor}}} \tag{2.17}$$

The mass scaling factor is equal to the subject's weight (70 kg) divided by the standard model's weight, which was also used to scale the segments' masses. The subject's fat percentage (11.81%) was used to compute the muscle strengths. The MSD scaling method "Scaling-Length-Mass-Fat External Measurements" was used to implement these landmarks lengths and compute the scaling factors.

The lumbar geometries were further adapted to the subject by using the L5 sagittal cross-section image dimensions calibrated using the given 1.5 mm diameter of the pressure probe visible in the image. The height of L_5 was estimated from the image as 25.25 mm (average of anterior and posterior heights). The L_5 depth and height-to-depth ratio were estimated from the image as 30.75 mm (average of superior and inferior depths) and 0.821 and compared with an *in vitro* study (Chen et al., 2017) reporting the ratio as 0.79 ±0.09 in normal persons. This verifies that this in-vitro study can be used to estimate L_5 width using its reported width-to-depth ratio of 1.39 ±0.08 as 44.28 mm (30.75 × [1.39+0.05]), where the 0.05 was added to account for deviation of height-to-depth ratio from the *in vitro* study value. Finally, the depth and width of L_5 in the standard model were 28.88 and 44.0 mm, respectively; therefore, the depth and width scaling factors were calculated as 1.06475 and 1.00636, respectively, and were implemented directly in the scaling matrix of the lumbar and thorax spine code in the MSD system.

Table 2.4
Conversion between the anatomic body-landmarks measurements conventions of the MSD system and the *in vivo* study

Measurement	*In vivo* subject's landmarks	(cm)	MSD model landmarks	(cm)
Head Height	Body Height – Chin Height	23.1	Distance from chin to top of head (vertically)	23.1
Pelvis Width	Linear distance between the most proximal points of the great trochanters of the femoral bones	33.3	Distance between external bony tips of trochanter (horizontally)	36.6
Trunk Height	Distance from C7 to L5	45.6	Distance from C7 to sacrum middle bony tip (vertically)	49.7
Upper Arm Length	Distance from shoulder height to the height of elbow joint (stretched)	33.3	Distance from elbow bony tip (Bursa) to acromion bony tip along Humerus (elbow flexed 90 Deg.)	34.4
Lower Arm Length	Distance from the height of elbow joint to the wrist height (Stretched)	22.7	Distance from elbow bony tip to ulna styloid bony tip along ulna (elbow flexed 90 Deg.)	25.1
Thigh Length	Distance from the height of greater trochanter to the knee height (Tibia condyle)	47.1	Distance from top of trochanter to Epicondylus lateral along thigh	43.1
Shank Length	Distance from the knee height (tibia condyle) to the height of ankle	36.7	Distance from Condulus medial to malleolus medial along shank	36.7
Foot Length	Distance from back of heel to tip of longest toe along foot	27.0	Distance from back of heel to tip of longest toe along foot	27.0

In vivo IVD Pressure Data Adaptation:

Using the *in vivo* IVD pressure data for model validation required its conversion from thoracolumbar-sacrum rotation to the thorax-pelvis rotation $\vec{R}_{A_{Thorax}A_{Pelvis}}$ used as the motion input in the MSD system, which is the rotation of the thorax anatomical frame A_{Thorax} relative to the pelvis anatomical frame A_{Pelvis}. The thoracolumbar-sacrum rotation in current study was the rotation $\vec{R}_{A_{Thorax}\,J_{Sacrum}}$ of the thorax anatomical frame A_{Thorax} relative to the sacrum joint frame J_{Sacrum} in the L_5-Sacrum spinal unit and is given by

$$\theta_{A_{Thorax}\,J_{Sacrum}\,Z} = 3.8675784\,\theta_{J_{T12}J_1\,Z} + \theta_{A_{Thorax}J_{T12}\,Z} \tag{2.18}$$

Rearranging and substituting in Eq. 2.8, the conversion formula is given by

$$\theta_{A_{Thorax}A_{Pelvis}\,Z} = 1.01837\left(\theta_{A_{Thorax}\,J_{Sacrum}\,Z} - \theta_{A_{Thorax}J_{T12}\,Z}\right) + \theta_{J_{Pelvis}A_{Pelvis}\,Z} + \theta_{A_{Thorax}J_{T12}\,Z} \tag{2.19}$$

Since the *in vivo* study does not distinguish the forward and backward extension-flexion motion curves, the average of the two curves were computed and Eq. 2.19 was used for the conversion, resulted curve is shown in Fig. 2.4.

Predicting IVD Pressure in the DJR MSD Lumbar Model:

IVD pressure from the DJR MSD model was predicted using the spherical joint definition, specifically the (non-elastic) joint reaction force, $\vec{F}_J$. This force is responsible for the coincident-nodes constraint supporting the spinal unit and exerted by the L_5 node on L_4 node measured from L_5 node's frame (Fig. 2.1a). The components of this force acting normal to the endplates' surfaces of both vertebrae were determined by creating novel aligned joint nodes at the same default joint nodes' positions with the Y-axes of their frames normal to the endplates' surfaces. $\vec{F}_J$ was transformed relative to the aligned joint nodes frames of L_4 and L_5, respectively, as

IVD pressure from the DJR MSD model was predicted using the spherical joint definition, specifically the (non-elastic) joint reaction force, $\vec{F}_J$. This force is responsible for the coincident-nodes constraint supporting the spinal unit and exerted by the L_5 node on L_4 node measured from L_5 node's frame (Fig. 2.1a). The components of this force acting normal to the endplates' surfaces of both vertebrae were determined by creating novel aligned joint nodes at the same default joint nodes' positions with the y axes of their frames normal to the endplates' surfaces. $\vec{F}_J$ was transformed relative to the aligned joint nodes frames of L_4 and L_5, respectively, as

$$\vec{F}_{A\,L4} = \vec{F}_J * \overline{\overline{Axes}}_J^T * \overline{\overline{Axes}}_{A\,L4} \quad and \quad \vec{F}_{A\,L5} = \vec{F}_J * \overline{\overline{Axes}}_J^T * \overline{\overline{Axes}}_{A\,L5} \tag{2.20}$$

where $\overline{\overline{Axes}}_J$, $\overline{\overline{Axes}}_{A\,L4}$ and $\overline{\overline{Axes}}_{A\,L5}$ are the rotational transformation matrices for L_5 default joint node's frame, and the L_4 and L_5 aligned joint node's frames, respectively. $\overline{\overline{Axes}}$ transforms any vector measured from a local node frame to the system's global C-sys. The IVD pressure $P_{J\,L4L5}$ in the L_4L_5 joint was calculated as

$$P_{J\,L4L5} = 1.54\frac{\left|(\vec{F}_{A\,L_4})_Y\right|+\left|(\vec{F}_{A\,L_5})_Y\right|}{2(A)} \tag{2.21}$$

where A is the transverse middle cross-sectional area of the IVD ($18e^{-4}\ m^2$ for the *in vivo* subject), and the 1.54 correction factor accounts for the larger load carrying contribution of the nucleus pulposus (Brinckmann and Grootenboer, 1991; Nachemson et al., 1960).

Predicting IVD Pressure in the ESN MSD Lumbar Model:

The IVD pressure in the L_4L_5 unit was calculated using the stiffness force $\vec{F}_E$ acting on the surface nodes at the elastic equilibrium configuration. The components of the force acting normal to the endplates' surfaces of both vertebrae were used. To determine these components, $\vec{F}_E$ was transformed relative to S_4 frame as

$$\vec{F}_{E\,S_4} = \vec{F}_E * \overline{\overline{Axes}}_{S_5}^T * \overline{\overline{Axes}}_{S_4} \tag{2.22}$$

where $\overline{\overline{Axes}}_{S_4}$ and $\overline{\overline{Axes}}_{S_5}$ are the rotational transformation matrices for the S_4 and S_5 frames, respectively. $\vec{F}_E$ is already relative to S_5 frame. The IVD pressure $P_{E\,L4L5}$ in the L_4L_5 joint of the ESN MSD model was calculated with the average of the two components

$$P_{E\,L4L5} = 1.54\frac{\left|(\vec{F}_E)_Y\right|+\left|(\vec{F}_{E\,S_4})_Y\right|}{2(A)} \tag{2.23}$$

Results

Outputs for the DJR and ESN MSD models included IVD pressure at the L_4L_5 spinal unit, VKS of individual lumbar vertebrae (L_1-Sacrum), and compressive and shear loads in the in L_4L_5

unit. Calculated IVD pressures were validated using subject-specific *in vivo* IVD pressure measurements published by Wilke et al. (1999; 2001) In addition, calculated IVD pressures were compared to IVD pressure predictions reported by Bassani et al. (2017) using a full-body MSD model in the AnyBody framework to model 25° to -30° of thorax-pelvis extension-flexion performed by a subject similarly sized to the subject in Wilke et al. (1999; 2001). Calculated compressive and shear loads in the L_4L_5 unit were compared with previous models reported by Arshad et al. (2016) that used the subject-specific anthropometrics of Wilke et al. (1999; 2001). Calculated VKS were validated using the *in vivo* sagittal plane rotations of individual lumbar vertebrae (L_1-Sacrum) reported by Wong et al. (2006), Rozumalski et al. (2008), Alemi et al. (2021), and the MSD model predictions of Arshad et al. (2016).

The magnitudes and pattern of IVD pressure variations throughout the extension-flexion motion were comparable with *in vivo* measures (Fig. 2.4, Table 2.5). Predicted IVD pressure magnitudes at the L_4L_5 spinal unit ranged from 0.33 MPa to 1.02 MPa for the DJR MSD model and from 0.69 MPa to 1.12 MPa for the ESN MSD model (Table 2.5), with increasing pressure during trunk flexion (Fig. 2.4). These magnitudes are similar to the *in vivo* range of 0.51 - 1.06 MPa (Table 2.5). The IVD pressure versus thorax-pelvis angle curve for the ESN MSD model had general non-linearity (correlation coefficient R = 0.906) that was comparable to the J-shaped curve for the *in vivo* measures (R = 0.841), with a more linear trend at higher flexion angles approaching a minimum difference of 3.9 % from the *in vivo* measures at -30° flexion. Although the DJR MSD model also had non-linearity (R = 0.908), the pattern was different than the *in vivo* curve. There were discontinuities at extension greater than 10°, a minimum difference of 5.9 % from the *in vivo* measures at 2° extension, and higher linear behavior with increasing flexion angles.

The DJR and ESN MSD models performed comparably to IVD pressure predictions from a full-body, subject-specific MSD model in the AnyBody framework, as reported by Bassani et al. (2017). Difference percentages between the model predictions and *in vivo* values were calculated using

$$\%\, Difference = \frac{|P - P_{vivo}|}{Max(|P|, |P_{vivo}|)} 100\% \tag{2.24}$$

where P is the model predicted pressure and P_{vivo} is the *in vivo* pressure reported by Wilke et al. (1999; 2001). The maximum difference for the DJR MSD model was 40.1% lower at 15° extension and the maximum difference for the ESN MSD model higher by 27.3% at 4° extension. Relative to the *in vivo* curve, the overall root mean squared (RMS) value was 0.121 and 0.143 for the DJR MSD model and ESN MSD model, respectively.

The more simply scaled DJR MSD model reported by Bassani et al. (2017), had and overall similar RMS value of 0.1149 relative to the *in vivo* curve, but had greater IVD pressure variations throughout the flexion-extension motion, resulting in higher non-linearity (R = 0.717) and a broader range of pressure magnitudes (0.32 MPa to 1.11 MPa) compared to the DJR and ESN MSD models in the current study.

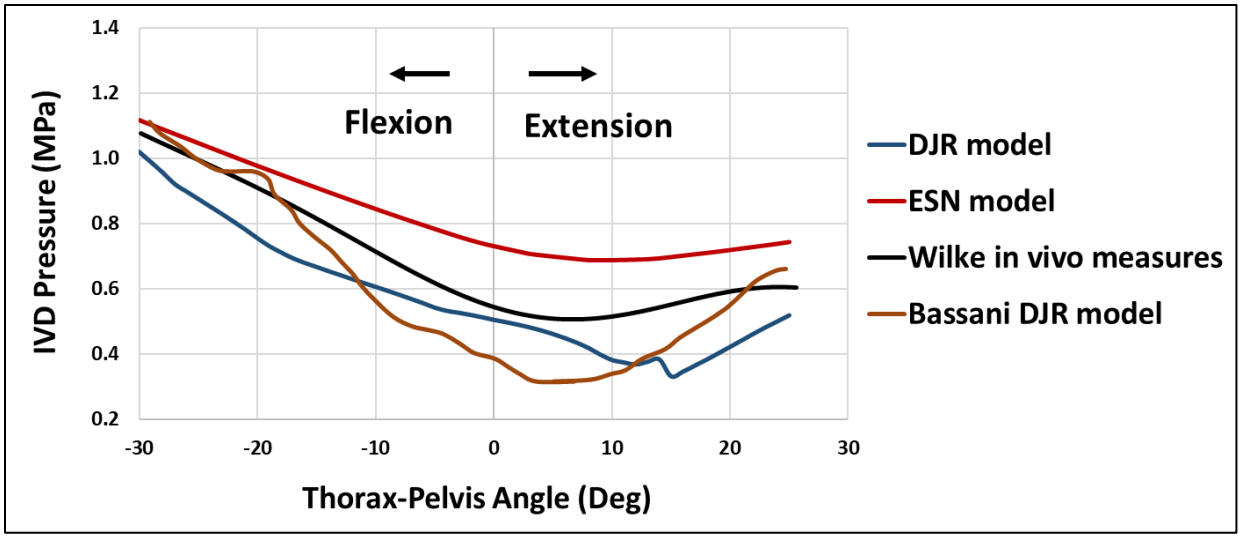

Fig. 2.4. IVD pressure predictions in L_4L_5 spinal unit. Note: The Bassani DJR model was scaled to the subject's height and weight whereas the DJR MSD model in the current study was fully scaled to the subject's anthropometrics and lumbar geometry.

Table 2.5
Comparison of IVD pressures at the L_4L_5 spinal unit calculated from the DJR and ESN MSD models during -30° to 25° of thorax-pelvis flexion-extension with subject-specific *in vivo* IVD pressure measurements (Wilke et al., 1999; 2001) and predictions from a full-body MSD model in the AnyBody framework (Bassani et al., 2017)

Source	Measure Type	Pressure Range (MPa)	Linearity (R)	RMS (MPa)
Wilke et al. (1999; 2001)	*In vivo* measure	0.51 – 1.06	0.841	Reference
Current study	Fully scaled DJR MSD model	0.33 – 1.02	0.908	0.121
Current study	Fully scaled ESN MSD model	0.69 – 1.12	0.906	0.143
Bassani et al. (2017)	Height-weight scaled DJR MSD model	0.32 – 1.11	0.717	0.115

The magnitudes and patterns of the calculated compressive and shear loads in the L_4L_5 unit of the ESN MSD model were validated against *in vivo* measurements and subject-specific MSD models from Arshad, et al. (2016). That study (Arshad, et al., 2016) implemented three spinal rhythms (SR-1, SR-2, SR-3) in a subject specific DJR MSD model scaled to the height and weight anthropometrics of Wilke et al. (1999; 2001). The loads were calculated over the range of 0° to -55° flexion of upper body inclination, which is approximately equivalent to the -30° of thorax-pelvis flexion used in the current study. The *in vivo* compressive load variations were highly linear

(R = 0.990) over the flexion range, and similar behavior was predicted by the ESN MSD model (R > 0.990) while the three spinal rhythm DJR MSD models showed less linearity (R > 0.980) especially over 0° to -7° flexion range (Fig. 2.5). The ESN MSD model predicted a narrower range of compressive load magnitudes (855.7 N to 1305.1 N) compared to the 627.0 N to 1238.0 N *in vivo* range and the 594.0 N to 1615.0 N range predicted by the three spinal rhythm models. Shear load variations were also highly linear for the ESN MSD model (R = 0.997) and the three spinal rhythm DJR MSD models (R > 0.970) (Fig. 2.5). The shear load magnitudes predicted by the ESN MSD model ranged from 52.0 N to 82.0 N and were comparable (RMS = 7.5) to the 46.0 N to 79.0 N shear loads predicted by the SR-1 spinal rhythm model.

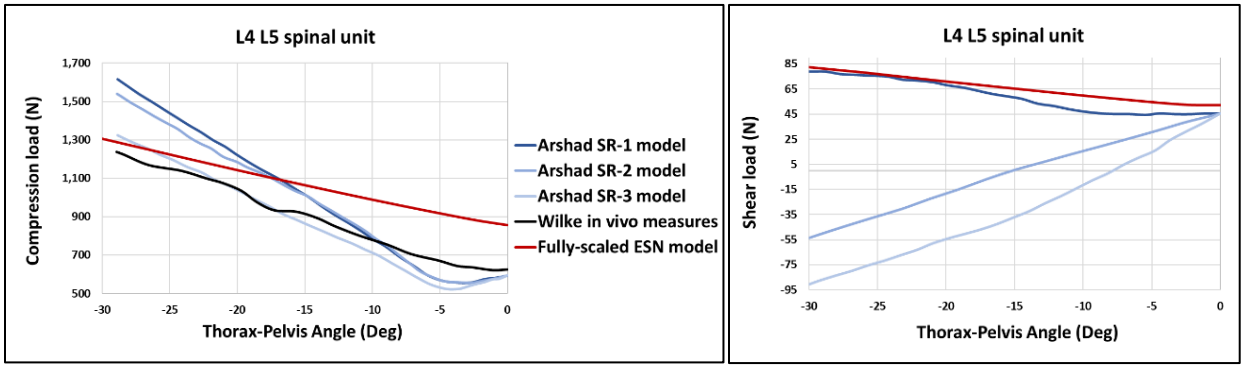

Fig. 2.5. Compression and shear loads predictions of the ESN MSD model compared with predictions of the DJR MSD models of Arshad et al. (2016) that incorporated three different spinal rhythm definitions (SR-1, SR-2, SR-3) and the Wilke et al. (1999; 2001) *in vivo* study (compressive loads only)

There were notable differences between the DJR and ESN MSD models in the calculated VKS for all lumbar units (Figs. 2.6-8). Comparing the Z-rotations (Fig. 2.6), the DJR MSD model generally underestimated the magnitude in the proximal units ($T_{12}L_1$) and overestimated the magnitude in the distal units ($L_5\ Sacrum$). The behavior in the ESN MSD model corresponds to removal of the DJR constraints and inclusion of the stiffness moments that support the spinal units

along with the muscles and ligaments. Comparing the Y-translations (Fig. 2.7), the DJR MSD model generally underestimated the magnitude in all spinal units ($T_{12}L_1$) through ($L_5\ Sacrum$). The behavior in the ESN MSD model corresponds to computation of the compressive IVD stiffness as a function of the Y-translation along with the contributions of the ligaments and muscles during the full-body MSD simulation. Comparing the X-translations (Fig. 2.8), the DJR MSD model generally underestimated the magnitude in all spinal units ($T_{12}L_1$) through ($L_5\ Sacrum$). The behavior in the ESN MSD model corresponds to computation of the shear IVD stiffness as a function of the X-translation in the absence of the spherical joint node constraint along with the contributions of the muscles and ligaments during the full-body MSD simulation. Underestimation of the Y-translation and X-translations in the DJR MSD model alters the normal distance and lateral distance between the adjacent vertebral surfaces in the spinal units that have direct effect on the stresses, strains, curvature, and the IVD pressure computations in the simulations using these VKS. Comparing the VKS predicted by the DJR and ESN MSD models, maximum deviations between the models generally occurred at the extremes of the flexion motion (-30^o) and minimum deviation generally occurred at the extreme of the extension motion (25^o). This behavior corresponds to the linearity of the predicted VKS curves, which generally results in the min/max values at the curves' terminals.

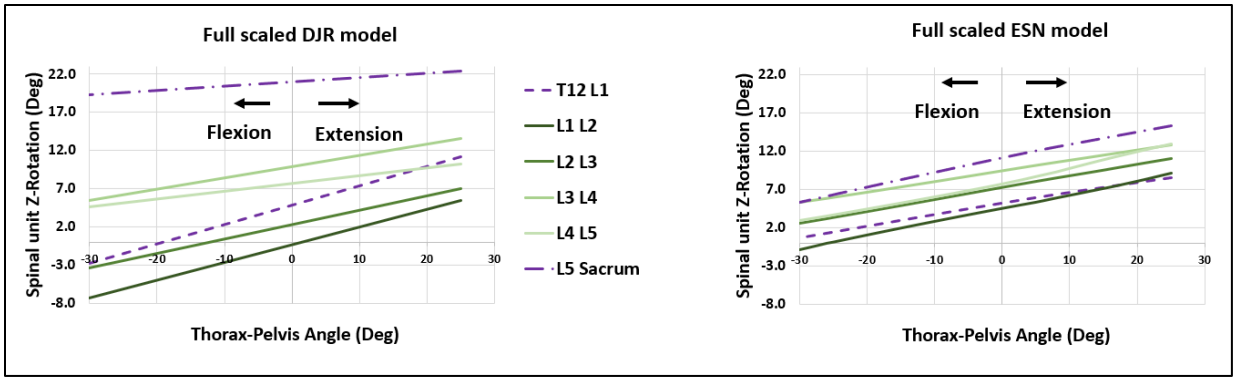

Fig. 2.6. Z-rotation VKS predictions for the DJR and ESN MSD models

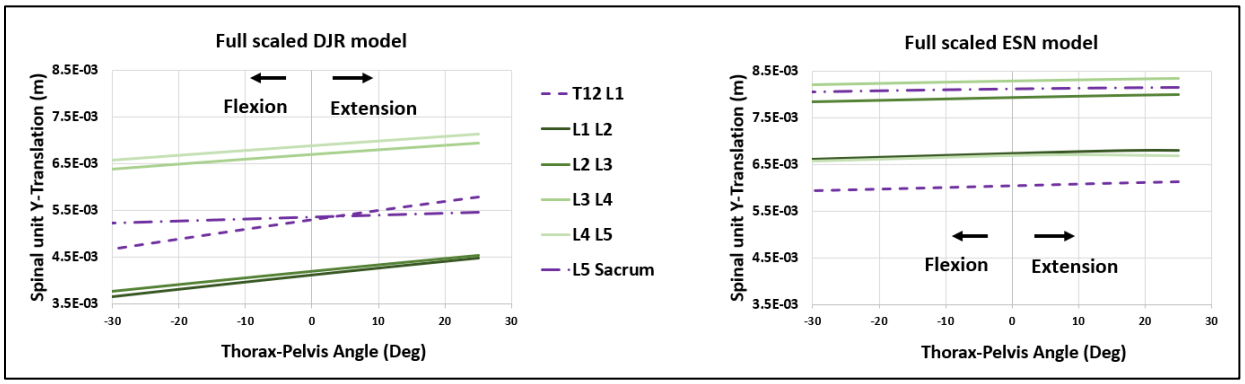

Fig. 2.7. Y-translation VKS predictions for the DJR and ESN MSD models

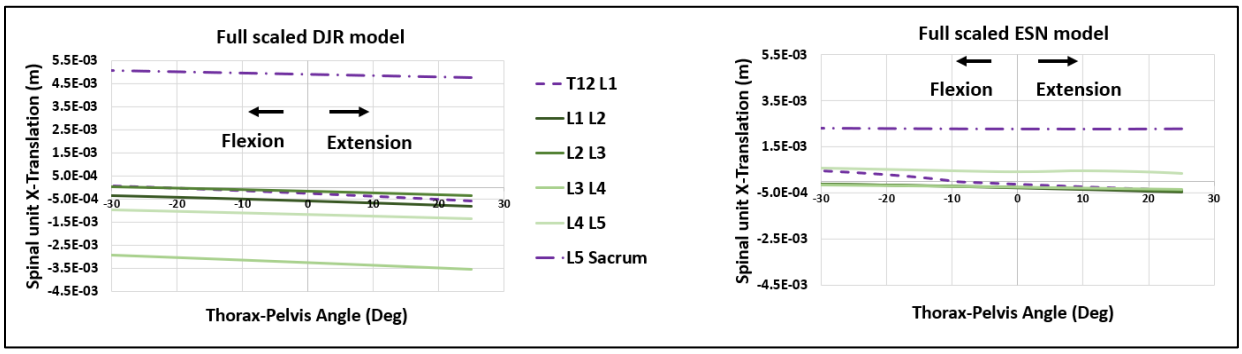

Fig. 2.8. X-translation VKS predictions for the DJR and ESN MSD models

Sagittal plane rotational VKS of the L_4L_5 unit (Z-rotation) calculated by the DJR and ESN MSD models were validated using the *in vivo* measurements reported in three studies (Alemi et al., 2021; Wong et al., 2006; Rozumalski et al., 2008). Wong et al. (2006) used automatic vertebrae segmentation and tracking to measure vertebral kinematics for flexion-extension motion of 30

healthy volunteers performing 10° to -25° of thorax-pelvis extension-flexion (Fig. 2.9). The change in rotational VKS were calculated from the DJR and ESN MSD models' predictions using the standing 0 º flexion posture as the zero reference after necessary conversion between thorax-pelvis and thorax-sacrum angles using Eq. 2.19. Variations in the L_4L_5 unit Z-rotation VKS were highly linear (R > 0.999) for both the DJR and ESN MSD models and the *in vivo* measures. However, only the ESN MSD model's predictions were comparable to the magnitudes of the *in vivo* Z-rotation VKS measurements (Wong et al., 2006) (Fig. 2.9). The DJR MSD model predictions underestimated (RMS = 0.239) the *in vivo* magnitudes by 22% at 10º extension and by 30% at -25° flexion and generally fell outside the standard deviation of the *in vivo* measures. Although predictions from the ESN MSD model overestimated the *in vivo* measures by 34% at 10º extension, predictions were within 8% over the 0° to -25° flexion range. The ESN MSD model better predicted (RMS = 0.629) *in vivo* measures, with predicted magnitudes generally within the standard deviation of the *in vivo* measures (Fig. 2.9). It is notable that the *in vivo* L_4L_5 Z-rotations varied considerably at 5° extension, which limits the strength of the validation for the extension range of motion.

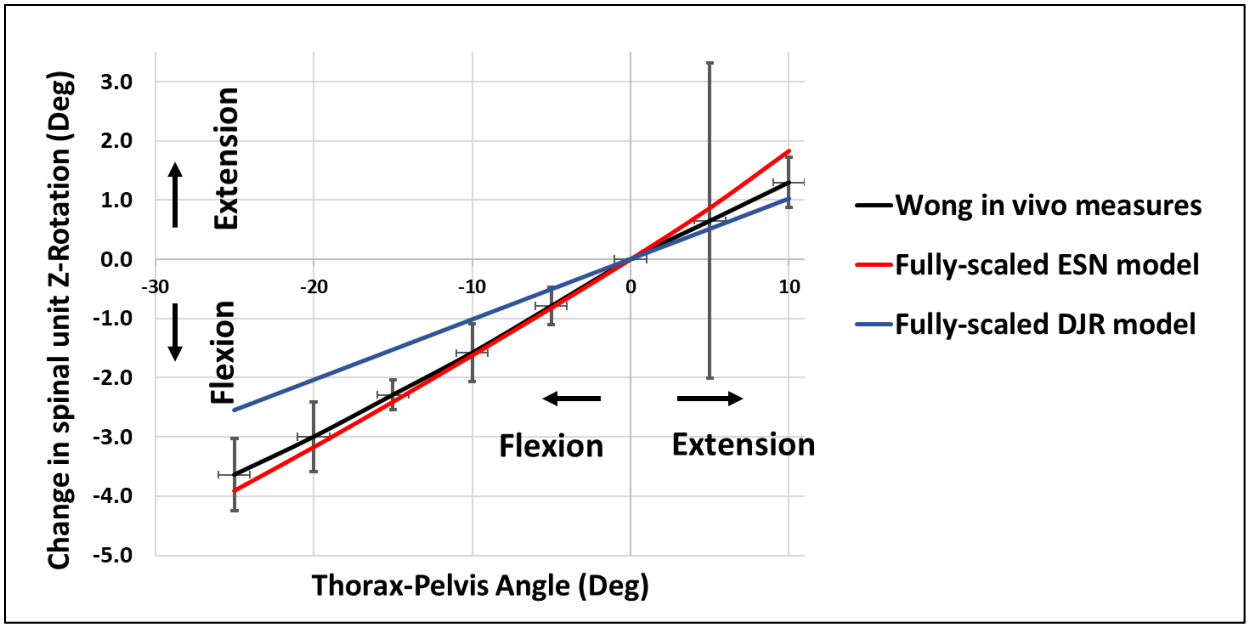

Fig. 2.9. Rotational VKS (Z-rotation) in the L_4L_5 spinal unit versus thorax-pelvis angle comparing the DJR and ESN MSD model predictions with *in vivo* measurements (Wong et al., 2006)

Similarly, the magnitude of sagittal plane rotational VKS (Z-rotation) for individual L_1-Sacrum spinal units in the ESN MSD model were represented as percentages of the overall lumbar spine rotation (L_1-Sacrum) (Fig. 2.10) and compared to *in vivo* data (Alemi et al., 2021; Rozumalski et al., 2008) and MSD spinal rhythm model predictions of Arshad, et al. (2016), as previously described. Rozumalski et al. (2008) used CT imaging and motion capture of reflective markers on wires directly implanted into the lumbar vertebrae of 10 healthy adults performing 0° to about -70° ± 14° of maximum trunk flexion. Alemi et al. (2021) reported median VKS based on six *in vivo* studies for 0° to -30° trunk flexion, and those data were recomputed to represent the lumbar rotations as percentages of L_1-sacrum rotation.

The ESN MSD model closely predicted the *in vivo* studies, with average absolute differences between the ESN MSD model and the *in vivo* data of 18.5% and 20.9% for Rozumalski et al. (2008) and Alemi et al. (2021) studies, respectively. Average absolute differences between the ESN MSD model predictions and the MSD spinal rhythm models (SR-1, SR-2, SR-3) were

larger (89.1%, 62.9%, and 48.7%, respectively). The ESN MSD model had a slightly concave up pattern in its predictions for the different spinal units from proximal to distal, with proximal and distal spinal units contributing a larger proportion of the overall sagittal plane rotation of the lumbar spine than the L_2-L_5 units. The different spinal rhythm models showed an increasing pattern (SR-1) with distal spinal units contributing to a larger proportion of the overall sagittal plane rotation of the lumbar spine, a decreasing pattern (SR-2) with a larger proportion of rotation from the proximal spinal units, and a concave down pattern (SR-3) with the L_2-L_5 units contributing to a larger proportion of the overall sagittal plane rotation of the lumbar spine.

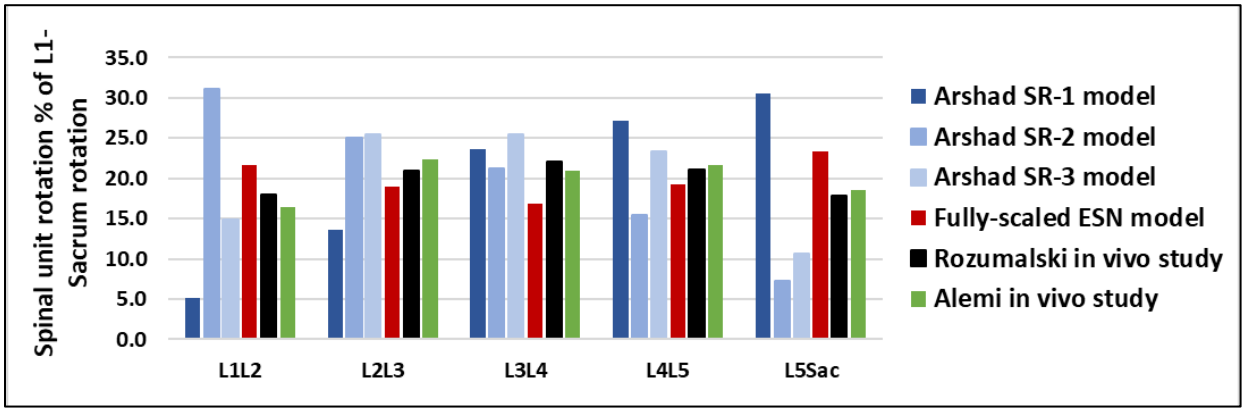

Fig. 2.10. Rotational, Z-direction, VKS predictions of ESN MSD model in lumbar spine units' comparisons with *in vivo* measurements (Alemi et al., 2021; Rozumalski et al., 2008) and DJR MSD models with three different spinal rhythms (Arshad et al., 2016)

Discussion and Conclusions

This study developed and validated a reformulated lumbar spine model for predicting individual VKS and IVD pressures during trunk extension/flexion in MSD simulations. The predictions of the reformulated ESN MSD lumbar model addressed technical parameters limiting realistic VKS in the existing lumbar model available through the AnyBody Managed Model Repository. That existing model, named the DJR MSD lumbar model in the current study, has

reliable predictions of spinal compressive loads and IVD pressure in literature (Bassani et al., 2017; De Zee et al., 2007), and comparable predictions from the DJR and ESN MSD models validate the ESN modeling approach in some aspects. However, the DJR MSD model was not suitable for predicting VKS or shear loads and this limitation was overcome by inclusion of elastic behavior in the ESN MSD model's spinal unit. The DJR and ESN MSD models were scaled to closely match subject-specific anthropometrics (Wilke et al., 1999; Wilke et al., 2001), which enabled validation of model predictions against *in vivo* measurements specific to that same subject and comparisons with other studies' models. Outputs for the DJR and ESN MSD models included IVD pressures and loads (compressive and shear) at the L_4L_5 spinal unit and VKS of individual lumbar vertebrae (L_1-Sacrum).

IVD pressure calculations were validated within the range of subject-specific IVD pressures for trunk extension-flexion (Table 2.5), including both *in vivo* measures anthropometrics (Wilke et al., 1999; Wilke et al., 2001) and previous DJR MSD model predictions (Bassani et al., 2017). RMS deviations for both the DJR and ESN MSD models were within 0.15 MPa of the *in vivo* measures, which is not unexpected given the approximately 10% variation in IVD pressure magnitudes reported in the original *in vivo* pressure data (Wilke et al., 1999; Wilke et al., 2001). Similarly, IVD pressure calculations originating from motion capture data inputs into an MSD system (Bassani et al., 2017) also show a lack of smoothness (Fig. 2.4), likely due to motion artifact in skin-mounted markers.

Calculated compressive and shear loads in L_4L_5 unit of the ESN MSD model were comparable to results from previous models (Arshad et al., 2016) that represented physiological variations in spinal rhythm and intra-abdominal pressure and used the same subject-specific anthropometrics (Wilke et al., 1999; Wilke et al., 2001) as the current study (Fig. 2.5). The ESN

MSD model's predictions of the compressive and shear loads in the L_4L_5 unit revealed its sensitivity to the influence of vertebral bone orientation on those loads. The Y-translational VKS predictions of the ESN MSD model were directly used to compute the IVD pressure magnitudes (Eq. 2.23) and compression loads using the stiffness functions. Similarly, the X-translational VKS predictions of the ESN MSD model were used to compute the shear loads using the stiffness functions. The ESN MSD model's predictions of the L_4L_5 IVD pressure were comparable to reported *in vivo* pressures for 25° extension to -30 °flexion motion, both in terms of the slopes and pressure magnitudes (Fig. 2.4). The ESN MSD model's predictions of the compressive load in the L_4L_5 unit were comparable in magnitude when compared to *in vivo* data and subject-specific MSD simulations inclusive of different spinal rhythms (Fig. 2.5). These validations are not applicable for the DJR MSD model in the current study due to the restrictions on the Y-translation by the spherical joint. The DJR MSD model showed facet joints engagement at about 14° extension (Fig. 2.4) while the ESN MSD model did not, which is due to the difference in the Z-rotation angle of L_4 vertebra relative to L_5 in the two models corresponding to the same thorax-pelvis posture of the whole lumbar spine.

The ESN MSD model's predictions of the L_4L_5 IVD pressure were comparable to reported *in vivo* pressures for 25º to -30º trunk extension-flexion, both in terms of the slopes and pressure magnitudes. Calculated shear loads in the L_4L_5 unit of the ESN MSD model were most similar to a spinal rhythm that allows for more rotation at the distal levels of the lumbar spine (SR-1), which were grossly deviated from the other two (SR2, SR3) rhythms (Fig. 2.5). This behavior indicates a strong relationship between the Z-rotations specified by the spinal rhythms and the loads acting in the anterior-posterior direction (X-axis) in the spinal unit, where inclination angles between the

vertebrae increase/decrease the force component along the X-axis that contributes to spinal unit anterior-posterior stability.

Calculated VKS were validated using *in vivo* sagittal plane rotations of individual lumbar vertebrae ($L_1 Sacrum$) reported in different studies (Alemi et al., 2021; Wong et al., 2006; Rozumalski et al., 2008). Compared to the DJR MSD model, the ESN MSD model better predicted *in vivo* measures of sagittal plane VKS (Z-rotations) for the L_4L_5 unit, most notably over the 0° to -25° flexion range (Fig. 2.9). When individual lumbar unit VKS were represented as a percentage of overall lumbar spine rotation (L_1-Sacrum), the ESN MSD model predictions were within approximately 20% of *in vivo* measures from several studies (Fig 2.10). However, the DJR MSD model predictions were less close to the *in vivo* (RMS = 0.629) than the ESN MSD model, which can be considered as a good verification for the ESN MSD model predictions because the Z-rotations of the DJR MSD model, that are prescribed by the spinal rhythm, are considered reliable in literature (Arshad et al., 2016).

The spinal rhythm is an important descriptor of spine biomechanics that links organ-level behavior of the lumbar spine to sagittal plane flexion of the upper body relative to the pelvis (Kuai et al., 2018). However, its usefulness for predicting the behavior of individual spinal units has been questioned (Arshad et al., 2016), since different definitions of the spinal rhythm (SR1, SR2, and SR3) alter the sagittal plane rotation of individual spinal units (Fig. 2.10) and directly affect the predicted compressive and shear loads (Fig. 2.5). The ESN MSD model in the current study revealed a slightly concave up pattern, with individual lumbar spinal units contributing 17% to 24% of the overall lumbar spine flexion/extension behavior. The ESN MSD model's sagittal plane VKS (Z-rotations) were comparable to *in vivo* data (Alemi et al., 2021; Rozumalski et al., 2008),

with absolute differences of approximately 20% for lumbar units' rotations in those studies and the ESN MSD model (Fig. 2.10).

Unlike direct measures of VKS and IVD pressure (Alemi et al., 2021; Wilke et al., 1999; Wilke et al., 2001; Wong et al., 2006; Rozumalski et al., 2008), the ESN MSD lumbar spine modeling approach developed in the current study does not require invasive imaging or implanted devices. Rather, it enables the computation of physiological VKS and IVD pressures from body-level motions in an MSD framework, with calculations defined as a function of different disc properties that alter these important spine characteristics. It provides the potential for studying altered disk behavior, whether due to injury or degenerative disease, by modifying the elastic properties of the disks that are defined by the stiffness functions. Such analyses are not possible with intervertebral spherical joint constraint in models using the DJR approach and the limited rotational degrees of freedom prescribed by a spinal rhythm. This ESN MSD lumbar spine can support other computational approaches for spine biomechanics like the FE analysis where the ESN-predicted VKS can be used to actuate the FE model.

Works Cited

Aiyangar, A.K., Zheng, L., Tashman, S., Anderst, W.J., Zhang, X. 2014. Capturing three-dimensional in vivo lumbar intervertebral joint kinematics using dynamic stereo-X-ray imaging. J. Biomech. Eng. 136 (1), 011004.

Alemi, M. M., Burkhart, K. A., Lynch, A. C., Allaire, B. T., Mousavi, S. J., Zhang, C., Bouxsein, M. L., Anderson, D. E. 2021. The influence of kinematic constraints on model performance during inverse kinematics analysis of the thoracolumbar spine. Front. Bioeng. Biotechnol. 9:688041.

Anderst, W.J., West, T., Donaldson, W. F., Lee, J. Y., Kang, J. D. 2016. A Longitudinal study of the six degrees of freedom cervical spine range of motion during dynamic flexion/extension and rotation after single-level anterior arthrodesis. Spine (Phila Pa 1976). 41(22).

Arshad, R., Zander, T., Dreischarf, M., Schmidt, H., 2016. Influence of lumbar spine rhythms and intra-abdominal pressure on spinal loads and trunk muscle forces during upper body inclination. Med. Eng. Phys. 38 (4), 333–338.

Bassani, Ta., Stucovitz, E., Qian, Z., Briguglio, M., Galbusera, F., 2017. Validation of the AnyBody Full Body Musculoskeletal Model in Computing Lumbar Spine Loads at L4L5 Level". 2017, April, Journal of Biomechanics 58 (2017) 89-96.

Brinckmann, P., Grootenboer, H., 1991. Change of disc height, radial disc bulge, and intradiscal pressure from discectomy: an *in vitro* investigation on human lumbar discs. Spine (Phila Pa 1976) 16 (6), 641–646.

Chen, H., Schlösser, T. P. C., Brink, R. C., Colo, D., Van Stralen, M., Shi, L., Chu, W. C. W., Heng, Ph-H., Castelein, R. M., and Cheng, J. C. Y., 2017, "The Height-Width-Depth Ratios of the Intervertebral Discs and Vertebral Bodies in Adolescent Idiopathic Scoliosis vs Controls in a Chinese Population," Scientific Reports, 7:46448.

Cheng, B., Castellvi, A. E., Davis, R. J., Lee, D. C., Lorio, M. P., Prostko, R. E. 2016. Variability in flexion extension radiographs of the lumbar spine: a comparison of uncontrolled and controlled bending. Int. J. Spine Surg. 10:20.

Cunningham, B. W., Kotani, Y., McNulty, P. S., Cappuccino, A., McAfee, P. C. 1997. The effect of spinal destabilization and instrumentation on lumbar intradiscal pressure: an *in vitro* biomechanical analysis. Spine (Phila Pa 1976). 22(22):2655-63.

Damsgaard, M., Rasmussen, J., Christensen, S. T., Surma, E., De Zee, M. 2006. Analysis of musculoskeletal systems in the AnyBody Modeling System, Simulation Modelling Practice and Theory. Volume 14, Issue 8, Pages 1100-1111.

De Zee, M., 2008. Implementation of Facet Joints in a Lumbar Spine Model. AnyBody Technology Documentations.

De Zee, M., Falla, D., Farina, D. Rasmussen, J. 2007. A detailed rigid-body cervical spine model based on inverse dynamics. Journal of Biomechanics, vol. 40 (2), pp. S284.

De Zee, M., Hansen, L., Wong, C., Rasmussen, J., Simonsen, E.B., 2007. A generic detailed rigid-body lumbar spine model. journal of biomechanics 2007; 40(6):1219-1227.

Delp, S. L., Anderson, F. C., Arnold, A. S., Loan, P., Habib, A., John, C. T., Thelen, D. G. 2007. OpenSim: open-source software to create and analyze dynamic simulations of movement. IEEE transactions on biomedical engineering, 54(11), 1940-1950.

Drake, J.D.M., Fischer, S.L., Brown, S.H.M., Callaghan, J.P., 2006. Do exercise balls provide a training advantage for trunk extensor exercises? A biomechanical evaluation. J. Manipulative. Physiol. Ther. 29 (5), 354–362.

El-Rich, M., Shirazi-Adl, A., Arjmand, N., 2004. Muscle activity, internal loads, and stability of the human spine in standing postures: combined model and in vivo studies. Spine (Phila Pa 1976) 29 (23), 2633–2642.

Fujii, R., Sakaura, H., Mukai, Y., Hosono, N., Ishii, T., Iwasaki, M. 2007. Kinematics of the lumbar spine in trunk rotation: in vivo three-dimensional analysis using magnetic resonance imaging. Eur. Spine J. 16, 1867–1874.

Grujicic, M., Pandurangan, B., Xie, X., Gramopadhye, A., Wagner, D., Ozen, M., 2010. Musculoskeletal computational analysis of the influence of car-seat design/adjustments on long-distance driving fatigue. Int. J. Ind. Ergonom. 40 (3), 345–355.

Han, K.S., Zander, T., Taylor, W.R., Rohlmann, A., 2012. An enhanced and validated generic thoraco-lumbar spine model for prediction of muscle forces. Med. Eng. Phys. 34, 709–716.

Heuer, F., Schmidt, H., Klezl, Z., Claes, L., Wilke, H-J., 2007. Stepwise reduction of functional spinal structures increases range of motion and change lordosis angle. Journal of Biomechanics 40 (2007) 271–280.

Hicks, J. L., Uchida, T. K., Seth, A., Rajagopal, A., Delp, S. L. 2015. Is my model good enough? Best practices for verification and validation of musculoskeletal models and simulations of movement. Journal of biomechanical engineering, 137(2).

Ignasiak, D., Dendorfer, S., Fergusson, S.J. 2016. Thoracolumbar spine model with articulated ribcage for the prediction of dynamic spinal loading. Journal of Biomechanics, vol. 49 (6), pp. 959-966.

Kaneoka, K., Ono, K., Inami, S., Hayashi, K. 1999. Motion analysis of cervical vertebrae during whiplash loading. Spine, volume 24, number 8, pp 763-770.

Kuai, Sh., Guan, X., Zhou, W., Zhang, R., Ji, R., Liao Z., Guo, D., Liu, W., Wang, D. 2018. Continuous lumbar spine rhythms during level walking, stair climbing and trunk flexion in people with and without lumbar disc herniation. Gait Posture, 63:296-301.

Li, G., Wang, S., Passias, P., Xia, Q., Li, G., Wood, K. 2009. Segmental in vivo vertebral motion during functional human lumbar spine activities. Eur. Spine J.18, 1013–1021.

Lin, C-C., Lu, T-W., Wang, T-M., Hsu, C-Y., Hsu, S-J., Shih, T-F. 2014. In vivo three-dimensional intervertebral kinematics of the subaxial cervical spine during seated axial rotation and lateral bending via a fluoroscopy-to-CT registration approach. Journal of Biomechanics 47(2014) 3310-3317.

Manchikanti, L., Singh, V., Datta, S., Cohen, S. P., & Hirsch, J. A. 2009. Comprehensive review of epidemiology, scope, and impact of spinal pain. Pain physician, 12(4), E35-70.

Mirab, S.M.H., Barbarestani, M., Tabatabaei, S.M., Shahsavari S., Minaeii Zangi, M.B. 2017. Measuring Dimensions of Lumbar Intervertebral Discs in Normal Subjects. Anatomical Sciences.; 14(1):3-8.

Nachemson, A. 1960. Lumbar Intradiscal Pressure. Experimental Studies on Postmortem Material. Acta Orthop. Scand. Supplementum, 43, 1–104.

Panjabi, M. M. 2003. Clinical spinal instability and low back pain. Journal of electromyography and kinesiology, 13(4), 371-379.

Raabe, M.E., Chaudhari, A.M.W., 2016. An investigation of jogging biomechanics using the full-body lumbar spine model: model development and validation. J.Biomech. 49 (7), 1238–1243.

Rasmussen, J., Damsgaard, M., Voigt, M., 2001. Muscle recruitment by the min/max criterion - a comparative numerical study. J. Biomech. 34, 409–415.

Rasmussen, J., De Zee M., Damsgaard, M., Christensen S. T., Marek, C., Siebertz, K. 2005. A General Method for Scaling Musculo-Skeletal Models. International Symposium on Computer Simulation in Biomechanics, Cleveland, Ohio, USA.

Sato, K., Kikuchi, Sh., Yonezawa, T. 1999. In vivo intradiscal pressure measurement in healthy individuals and in patients with ongoing back problems. Spine, Volume 24 - Issue 23 - p 2468.

Schmoelz, W., Huber, J. F., Nydegger, T., Claes, L., Wilke, H. J. 2006. Influence of a dynamic stabilization system on load bearing of a bridged disc: an *in vitro* study of intradiscal pressure. Eur Spine J. 15(8):1276-85.

Stambolian, D., Eltoukhy, M., Asfour, S., 2016. Development and validation of a three-dimensional dynamic biomechanical lifting model for lower back evaluation for careful box placement. Int. J. Ind. Ergon. 54, 10–18.

Staub, B. N., Holman, P. J., Reitman, C. A., Hipp, J. 2015. Sagittal plane lumbar intervertebral motion during seated flexion-extension radiographs of 658 asymptomatic non degenerated levels. J Neurosurg Spine 23:731–738.

Tae Soo, B., Museong, M., 2010. Effect of lumbar lordotic angle on lumbosacral joint during isokinetic exercise: a simulation study. Clin. Biomech. (Bristol, Avon) 25(7), 628–635.

Wang, H., Zhou, C., Yu, Y., Wang, C., Tsai, T.-Y., Han, C. 2020. Quantifying the ranges of relative motions of the intervertebral discs and facet joints in the normal cervical spine. J. Biomech. 112:110023.

Wang, S., Xia, Q., Passias, P., Li, W., Wood, K., and Li, G., 2011, “How Does Lumbar Degenerative Disc Disease Affect the Disc Deformation at the Cephalic Levels In vivo?,” Spine, 36(9), pp. E574–E581.

Wang, S., Xia, Q., Passias, P., Wood, K., and Li, G., 2009, "Measurement of Geometric Deformation of Lumbar Intervertebral Discs Under In-Vivo Weightbearing Condition," J. Biomech., 42(6), pp. 705–711.

Weisse, B., Aiyangar, A.K., Affolter, Ch., Gander, R., Terrasi, G.P., Ploeg, H., 2012. Determination of the translational and rotational stiffnesses of an L4–L5 functional spinal unit using a specimen-specific finite element model. Journal of the mechanical behavior of biomedical materials.; 13(2012)45–61.

White, A. A., Panjabi, M. M. 1978. The Basic Kinematics of the Human Spine. Spine: Volume 3 - Issue 1 - p 12-20.

Wilke, H-J., Neef, P., Caimi, M., Hoogland, T., Claes, L., 1999. New In vivo Measurements of Pressures in the Intervertebral Disc in Daily Life. SPINE Volume 24, Number 8, pp 755–762, 1999.

Wilke, H-J., Neef, P., Hinz, B., Seidel, H., Claes, L., 2001. Intradiscal Pressure Together with Anthropometric Data – A Data Set for Validation of Models". Clinical biomechanics 16 supplement No. 1 (2001) S111-S126.

Wong, K. W. N., Luk, K. D. K., Leong, J. C. Y., Wong, S. F., Wong, K. K. Y. 2006. Continuous dynamic spinal motion analysis. Spine Volume 31, Number 4, pp 414–419

Yeager, M. S., Cook, D. J., Cheng, B. C. 2013. Reliability of computer-assisted lumbar intervertebral measurements using a novel vertebral motion analysis system. Spine J. 14(2):274-81.

CHAPTER THREE

A MULTI-SCALE PIPELINE OF COMPUTATIONAL SIMULATIONS TO MAP MUSCULOSKELETAL DYNAMICS MODEL OF LUMBAR SPINE INTO A KINEMATICS-DRIVEN FINITE ELEMENT MODEL: APPLICATION TO INTERVERTEBRAL DISC BEHAVIOR IN A SUBJECT-SPECIFIC FINIT ELEMENT MODEL

Introduction

Over the past four decades, simulations based on finite element (FE) models of the spine have been an important tool for advancing our understanding of spine biomechanics (Fagan et al., 2000a; Fagan et al., 2000b; Jones et al., 2008, Natarajan et al., 2004; Schmidt et al., 2013). In general, spine FE models combine isolated spinal segments (e.g. lumbar spine or functional spinal units) with detailed material properties of spinal tissues, including the vertebral bone and endplates, the intervertebral discs (IVD), and the surrounding ligaments. Model validation commonly involves *in vitro* experimental methods applied to isolated spinal segments under controlled load and motion conditions that broadly represent human spine biomechanics. However, muscle loads are largely unknown for even the most basic spinal motions, and realistic loading conditions are difficult to apply (Rohlmann et al., 2009).

Simplified representations of spinal tissues and vertebral loading conditions are a common feature in FE models and musculoskeletal dynamics (MSD) simulations of the entire human body. For example, initial FE models used for exploring body-level biomechanics in vehicle crash tests modeled the thoraco-lumbar region as a single rigid segment and did not assign viscoelastic material properties for soft tissues. Without detailed modeling of the lumbar spine, including individual lumbar vertebra and IVD with time-dependent material properties, such models have proven inadequate for predicting spinal injuries in actual crashes and have limited use for understanding organ-level behavior of the spine (Amiri et al., 2018; Guo et al., 2022;

Somasundaram et al., 2019). Similarly, MSD simulations specifically developed for musculoskeletal research impose kinematic constraints for estimating individual vertebral motions that best match overall trunk posture and motion (Alemi et al., 2021). As described in Chapter two, modeling algorithms relying on spinal rhythm definitions to actuate spherical joints that constrain vertebral translation do not replicate physiological load bearing through the vertebrae endplate surfaces and across the IVD. Continued innovations in organ-level FE models are needed to better represent physiological loading conditions in the spine and to assess spine tissue behavior during a broad range of functional activities.

Progressive innovations in FE modeling of the spine are historically linked to development of technologies that enable more precise measures of *in vivo* spine biomechanics. For example, measures of *in vivo* IVD pressures (Wilke et al., 1999; Wilke et al., 2001; Sato et al., 1999) and intervertebral loads (Rohlmann et al., 2014) have enabled alternative approaches for FE model validation that include those *in vivo* parameters. However, because FE models commonly render the lumbar spine in isolation from other body segments, the loading inputs represent average external loads on the spine rather than individual physiological loads. Similarly, modeling approaches based on kinematic inputs (Aiyangar et al., 2014; Anderst et al., 2016; Cheng et al., 2016; Fujii et al., 2007; Kaneoka et al., 1999; Li et al., 2009; Lin et al., 2014; Staub et al., 2015; Wang et al., 2009; Wang et al., 2011; Wang et al., 2020; Yeager et al., 2013) are supported by techniques that use dual-plane fluoroscopy or dynamic magnetic resonance imaging to measure *in vivo* vertebral kinematics (VKS). However, *in vivo* measurement of VKS during dynamic motion is not widely used clinically and common medical imaging systems are limited in the types of motions that can be analyzed. Moreover, kinematic constraints applied to FE models for computational efficiency (Alemi et al., 2021) differ from the kinematics measured within the spinal

units during actual activities of daily living. Alternative approaches for computing VKS during dynamic body-level motions are needed to support these modeling efforts.

Given that optoelectronic motion analysis techniques and MSD simulations are ubiquitous in biomechanical research related to musculoskeletal injuries and disorders (Colyer et al., 2018; Damsguaard et al., 2006; Delp et al., 2007), it would be very advantageous to predict VKS from body-level motions. MSD simulations combined with the reformulated spine model developed in a previous study (Jaradat et al., 2022) (Chapter Two), where the complete details for this approach were fully described in Chapter 2, would provide a new and innovative approach for predicting VKS in the lumbar spine during actual activities of daily living. This modeling approach has potential clinical significance because abnormal VKS are linked to altered IVD pressure (Cunningham et al., 1997; Schmoelz et al., 2006), which is a known feature in subjects with disc degeneration (Sato et al., 1999). Abnormal VKS in the lumbar spine contribute to clinical instability and both conditions are underlying factors in the 15% to 45% annual prevalence of low back pain (Manchikanti et al., 2009; Panjabi et al., 2003).

The purpose of this study was to develop a noninvasive simulation tool that predicts individual VKS from conveniently measured body-level motions and use them in, kinematically-driven, spine tissue FE analysis. The simulation tool consisted of a novel pipeline of multi-scale computational dynamics simulations, 3D modeling, and scripting tools generating a kinematics-driven FE model (KD-FEM) of the lumbar spine. This study uses MSD simulations to predict the VKS and since the general MSD simulations are not designed to calculate realistic VKS, this study incorporated the modified lumbar spine model from a previous work (Jaradat et al., 2022) (Chapter Two), where the complete details for this approach were fully described in Chapter 2, previously identified as the elastic surface nodes (ESN) model. The ESN MSD model removed nonrealistic

kinematic constraints and included elastic IVD behaviors in the spinal units. The subject-specific KD-FEM lumbar vertebrae were actuated by the individual VKS during four activities and mapped automatically by the custom script from the ESN MSD model for the same subject. The KD-FEM lumbar model was created as a general model that can be integrated with other soft tissue FE model for analyzing the effect of VKS during a range of motion. The utility of the pipeline was demonstrated by incorporating an IVD FE model in the pipeline into the KD-FEM at the L_4L_5 level and using it to predict IVD pressures during the four activities. IVD pressures predicted by the pipeline were compared with previously published *in vivo* pressures (Wilke et al., 1999; Wilke et al., 2001) and a default MSD model (Bassani et al., 2017) of the same subject during a range of 0^o to 30^o flexion motion and different four load carrying activities of daily living compared with corresponding pressure predictions from i) *in vivo* study measurements, ii) *in vivo* subject-specific ESN MSD model, and iii) *in vivo* subject-specific default MSD model from a motion capture study (Bassani et al., 2017), where the IVD model was combined with the KD-FEM.

Methods

The general pipeline methods

The general pipeline of multi-scale computational simulations was developed to map the lumbar spine model from subject-specific MSD simulations into an equivalent FE model driven by the same MSD-predicted VKS. It supported integration of different soft tissue models for deformable FE analysis and calculation of IVD pressure for flexion motion and four different standing and load carrying postures. The pipeline included MSD modeling, various 3D modeling and scripting tools, and finite element analysis software (Fig. 3.1).

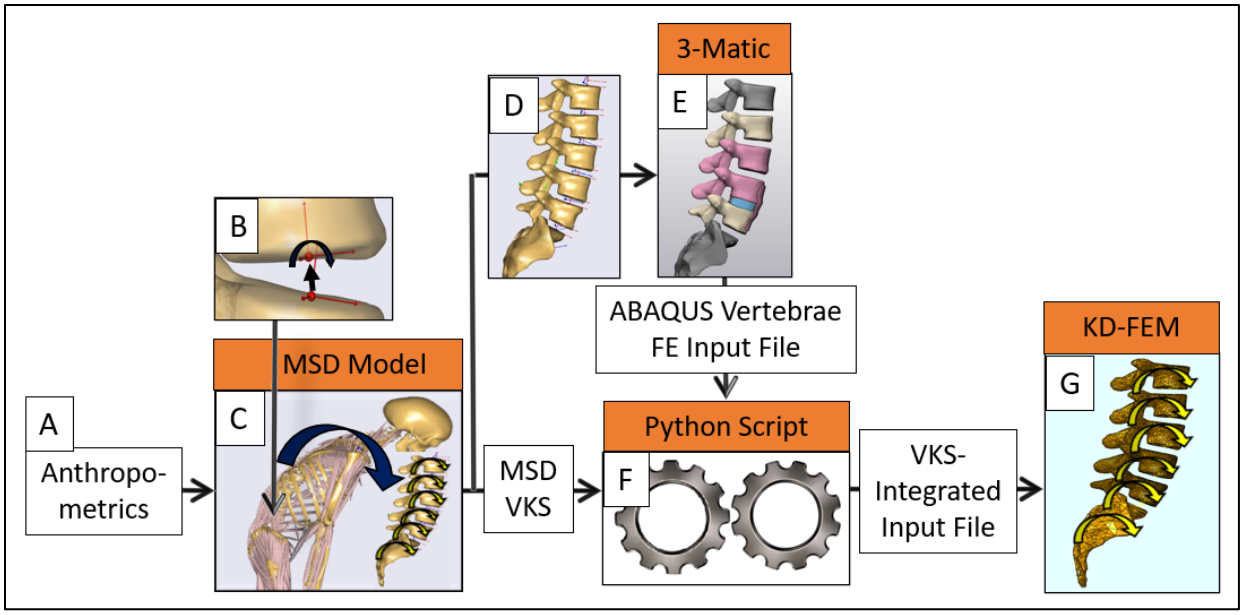

Fig. 3.1. The general pipeline steps included: A) measured subject specific anthropometrics input into B) an elastic surface nodes (ESN) lumbar spine MSD model that C) output individual VKS over the motion range and D) output subject-specific MSD lumbar vertebral geometry at the initial body posture. These results were E) input into 3D modeling software to output vertebrae FE mesh and vertebrae surfaces in a preliminary ABAQUS *Input* file format that was combined with F) the individual VKS by Python custom script and output *Input* file integrated with VKS. The *Input* file was G) run in ABAQUS FE analysis software to create the kinematics-driven FE model (KD-FEM)

Subject-specific MSD model:

A subject-specific MSD model was adapted from the standard full-body model available through the AnyBody Managed Model Repository (©2022 AnyBody Technology A/S, Aalborg, Denmark, AnyBody Software, v7.3), which has anatomical data corresponding to the 50th percentile size for a European male. Subject-specific inputs (anthropometrics) were derived from the 45-year-old healthy male study reported by Wilke et al. (1999; 2001). Measures from this subject (hereafter, *in vivo* measures) were selected because they are associated with IVD pressures acquired by a pressure probe inserted into the subject's L_4L_5 IVD during controlled thoracolumbar-sacrum rotations and load carrying postures that are widely used for modeling validations (Bassani et al., 2017; Alemi et al., 2021; Hicks et al., 2015). The MSD model was

scaled using the scaling method "Scaling-Length-Mass-Fat External Measurements" to match the subject's height, weight, fat percentage (70 kg, 173.9 cm, and 11.81%), and detailed anatomic landmarks reported by *in vivo* study (Wilke et al., 1999; 2001). The landmarks' measurements were converted to match the convention of the MSD system, and scaling factors for the body segments were computed to scale their lengths, widths, and depths (Jaradat et al., 2022) (Chapter Two). The available L_4L_5 sagittal cross-sectional radiographic image was used to compute more precise depth and width scaling factors for the lumbar vertebrae geometries (1.06475 and 1.00636, respectively), and the thorax geometries were also scaled with these same factors (Jaradat et al., 2022) (Chapter Two).

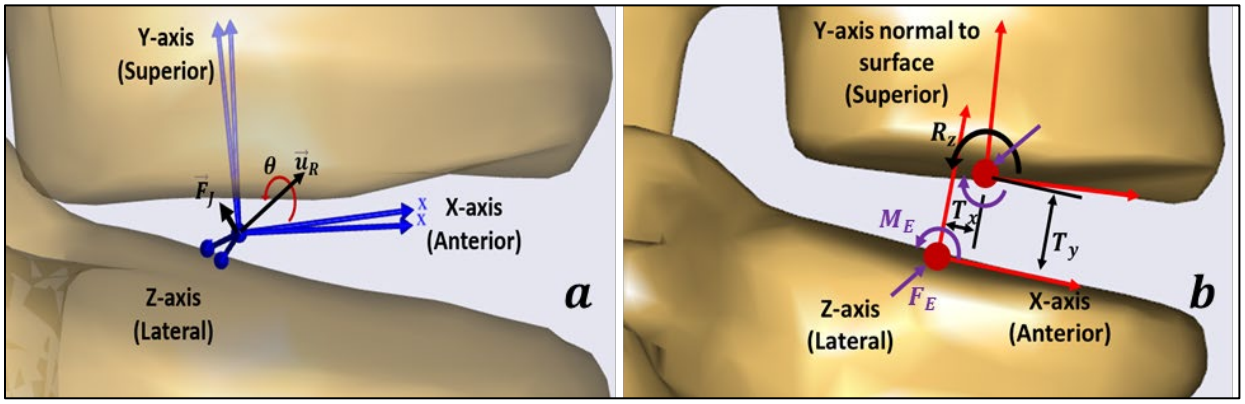

Fig. 3.2a. (Repeated from Fig. 2.1a and Fig. 2.1b) The DJR MSD model includes the spherical joint's two coincident nodes, their local C-sys frames, joint rotation's rotation vector ($\vec{u}_R$) and angle (θ), and non-physiological joint reaction force ($\vec{F}_J$) that supports the unit. **Fig. 3.2b.** The ESN MSD model removed spherical joint (and spinal rhythm), include surface nodes at endplates centers, their surface-aligned C-sys frames (in red), spinal unit VKS measures definitions (in black), and replaced $\vec{F}_J$ with the elastic force $\vec{F}_E$ and moment $\vec{M}_E$ corresponding to IVD stiffness (in purple) (Jaradat et al., 2022) (Chapter Two)

Subject-specific ESN MSD model of the spine:

The existing standard MSD model, with the default lumbar spherical joints and lumbar spinal rhythm (DJR MSD model), was modified to include the previously developed elastic surface

nodes (ESN) MSD model (Fig. 3.2).The ESN MSD model was used to remove non-physical kinematic constraints in the DJR MSD model (Fig. 3.2), which included a default spherical joint definition that produced a joint pivot effect on the relative translation and rotation VKS between the vertebrae and prescribed the sagittal plane rotational VKS through spinal rhythm inputs. The ESN MSD model removed the spherical joint definition and the spinal rhythm constraints for all spinal units ($T_{12}L_1$ to $L_5Sacrum$) to enable elastic behavior in lumbar spinal units and to allow the IVD stiffness, muscles, and ligaments to determine the rotational VKS. The ESN MSD model replaced the non-physiological joint reaction force $\vec{F}_J$, that supports the unit with the elastic forces $\vec{F}_E$ and moments $\vec{M}_E$ corresponding to IVD stiffness (Jaradat et al., 2022) (Chapter Two).

The ESN MSD model was based on novel endplate surface nodes created at the centers of the endplate's surfaces with their aligned C-sys frames (Fig. 3.2b). The VKS measurements in the spinal units ($T_{12}L_1$ to $L_5Sacrum$) were based on these surface nodes and defined as the translation of the upper node and the rotation of the upper node's frame measured from the lower nodes' frame (Fig. 3.2b). This enabled the elastic behavior in the lumbar spinal units, with the ESN MSD model applying the stiffness forces and moments to the surface nodes and calculating their magnitudes during the simulation using the surface nodes' VKS multiplied by the stiffness functions that were fitted from *in vitro* and FE studies (Jaradat et al., 2022) (Chapter Two). The equilibrium configurations (VKS and loads) in the elastic units in the ESN MSD model equalizing loads coming from the whole body were solved using a minimum potential energy solution method. The DJR kinematics were manually and mathematically derived in terms of the surface node, for flexion-extension motion, and prescribed as an initial solution using a novel kinematics driver that engaged the force-dependent kinematics (FDK) solver in the MSD system (Jaradat et al. 2022) (Chapter Two). Both DJR and ESN MSD lumbar models are actuated by the kinematic

input of the total thorax-pelvis rotation that represents the rotation of the thoracolumbar joint, represented by the thorax anatomical frame, relative or measured from the pelvis anatomical frame.

Subject-specific FE Lumbar Model Geometries:

The subject-specific vertebral geometries from the ESN MSD model were imported into 3D modeling software (3-Matic, v14.0, ©2022 Materialise NV, Leuven, Belgium) as STL files and oriented into the initial standing posture defined by the MSD simulation (Fig. 3.1D). The global C-sys from the MSD model was used as the reference for the initial posture's positions and orientations. Vertebral bodies were meshed as rigid bodies and output into a preliminary *Input* analysis file for the FE analysis (ABAQUS, v6.14, Dassault Systemes, Waltham, MA). The *Input* analysis file included the naming scheme from 3-Matic and necessary ABAQUS keywords for the definitions of parts, assembly instances, meshes, volumes, sections, and surfaces.

General pipeline for kinematics-driven FE model (KD-FEM) of the lumbar spine:

The subject-specific KD-FEM lumbar spine was actuated by the individual VKS using a custom script to automatically map the ESN MSD model to the KD-FEM. The KD-FEM of the lumbar spine included the subject-specific vertebrae geometries (as rigid bodies) at the initial standing posture's positions and orientations and was kinematically driven by the VKS predicted by the ESN MSD model. This was accomplished using a custom Python script (Van-Rossum and Drake, 2009) to automatically map the ESN MSD and KD-FEM simulations, integrating the VKS into the preliminary ABAQUS *Input* file (Fig. 3.3) and preparing it to run in ABAQUS CAE (Fig. 3.1F-G). Specifically, the script read the output text file for the range of motion simulated in the ESN MSD model, which includes the time histories of the translational and rotational VKS for the individual lumbar vertebrae. The script transformed the MSD VKS into VKS motion amplitudes

(increments vs time) for each degree of freedom of the upper surface node in the spinal units and wrote text files corresponding to the boundary conditions in ABAQUS format.

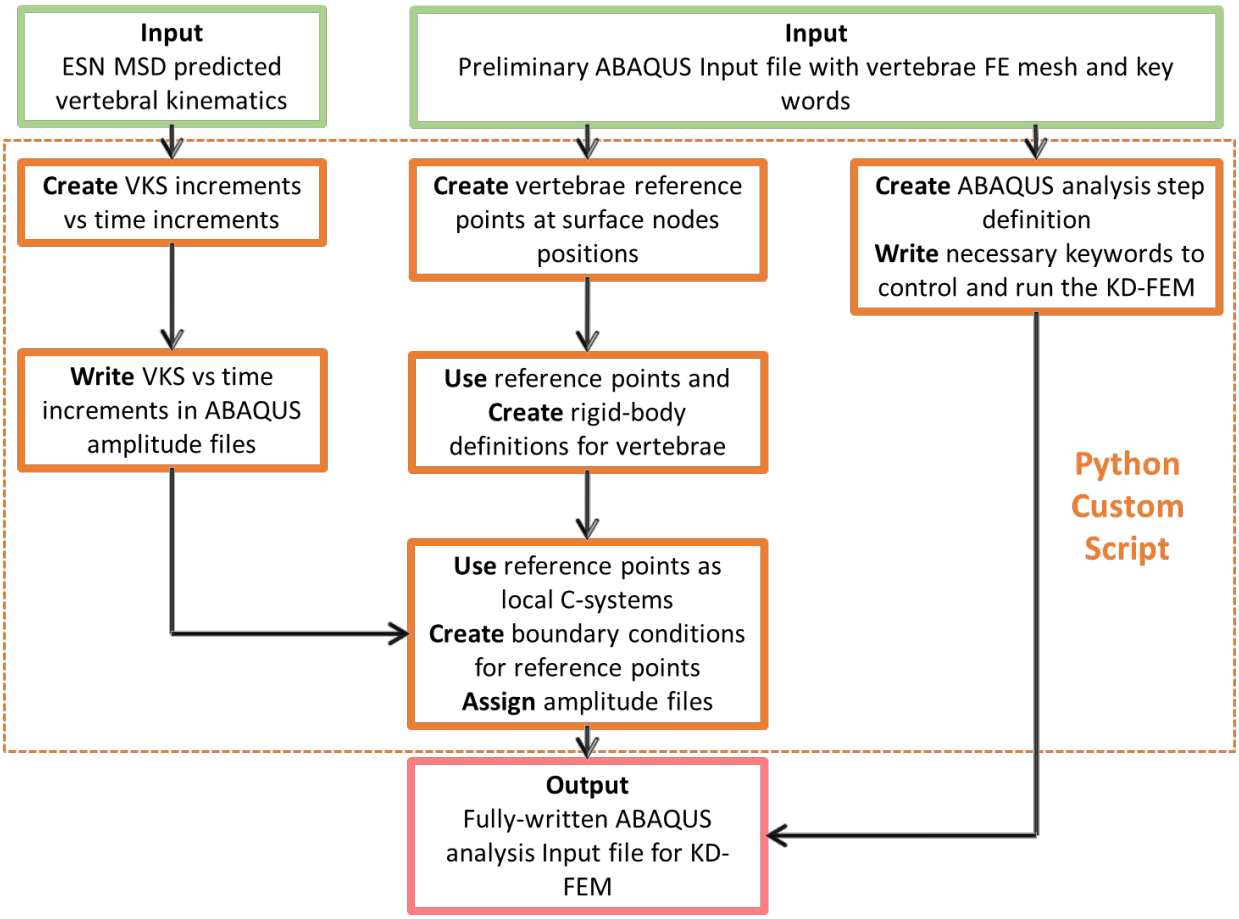

Fig. 3.3. Python mapping script to generate the *Input* file for the KD-FEM. The custom script automatically mapped the ESN MSD and KD-FEM simulations by defining: i) reference points for the rigid body definitions of the vertebral surface meshes in the KD-FEM located at the positions of the vertebral surface nodes from the ESN MSD model; ii) reference points for the local C-sys corresponding to the MSD surface nodes C-sys, iii) boundary conditions for the reference points that were assigned the VKS amplitude files for each DOF, and iv) step increments and other necessary controls to run in ABAQUS CAE

In the next section, the utility of the pipeline was demonstrated by incorporating an IVD FE model into the KD-FEM at the L_4L_5 level and using it to predict IVD pressures during four activities.

General pipeline applications: Assessment of an IVD FE model

IVD behavior during four different standing and load-carrying postures was assessed by integrating a subject-specific IVD FE model into the KD-FEM at the L_4L_5 spinal unit (Fig. 3.4). The general pipeline was run to calculate the VKS during 0° to 30° flexion motion and during three different load carrying activities. The predicted IVD pressures at the L_4L_5 spinal unit were compared to IVD pressures from previously published *in vivo* and motion capture studies for the four activities (Wilke et al., 1999; Wilke et al., 2001; Bassani et al., 2017).

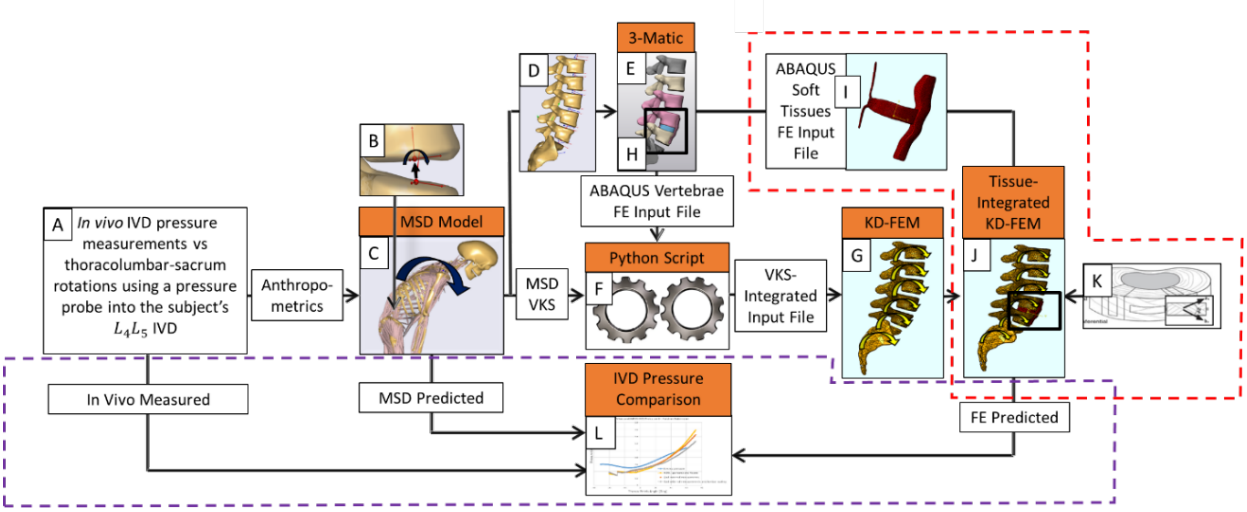

Fig. 3.4. A) *In vivo* measures of anthropometrics and body-level motion of (Wilke et al., 1999; Wilke et al., 2001) were input into the subject-specific ESN MSD model, B-G) and the general pipeline steps were executed. H-I) Soft tissue geometries and FE meshes of L_4L_5 spinal unit created and output into an ABAQUS *Input* file, J) were integrated into the KD-FEM along with K) FE material model definitions for tissue components. L) IVD pressures predicted by the KD-FEM were output for comparison with *in vivo* measures and other lumbar spine MSD models.

Subject-specific geometry of the L_4L_5 spinal unit in the KD-FEM:

The subject-specific L_4L_5 spinal unit was defined to include the $L_4 and\ L_5$ vertebral bones, the endplates, the IVD including the AF and NP, and the anterior longitudinal ligament (ALL) and posterior longitudinal ligament (PLL). The ligaments' role in the analysis was to naturally restrict

the AF from bulging out in the anterior posterior direction. The spinal unit geometry was manually defined by the space between L_4 and L_5 vertebrae at the initial standing posture. This space was defined by importing the bony geometry from the subject-specific ESN MSD model into the 3D modeling software (3-Matic) since an MRI for the *in vivo* study's subject was not available. The endplates thickness was varied from 1.0 to 0.6 mm toward the center, as defined by Pitzen, et al. (2004). The annulus fibrosus (AF) height dimensions were based on the space between vertebrae, and the AF thicknesses in the transverse plane were scaled relative to the subject-specific AF depth and width, as defined by Suárez et al. (2015) (Fig. 3.5 and Table 3.1). The ALL and PLL were assigned a 1.0 mm thickness that conformed to the surface of the L_4 and L_5 vertebrae. Specific surfaces on the soft tissues and vertebrae were created to connect the individual components and assigned a distinct naming scheme.

The geometric volumes were meshed using triangle surface elements and tetrahedron volume elements to accommodate the non-uniform geometries of the spinal unit components (Fig. 3.5a). The FE mesh of the tissue components was output in the ABAQUS *Input* file format that included the parts, instances, and other necessary ABAQUS keywords to run the model. The number of elements at which the FE solution converged to the same magnitudes were about 216,000, 18,000, 14,000, and 9,500 elements for the AF, both endplates, ALL, and PLL, respectively.

The Abaqus *Input* file of the L_4L_5 soft tissues FE model was integrated into the KD-FEM lumbar model (Fig. 3.4J). The spinal unit components were assembled using tie constraints between different soft tissues components and the vertebrae surfaces, with the exception of frictionless contact properties between the ALL and the AF and between the PLL and both vertebrae.

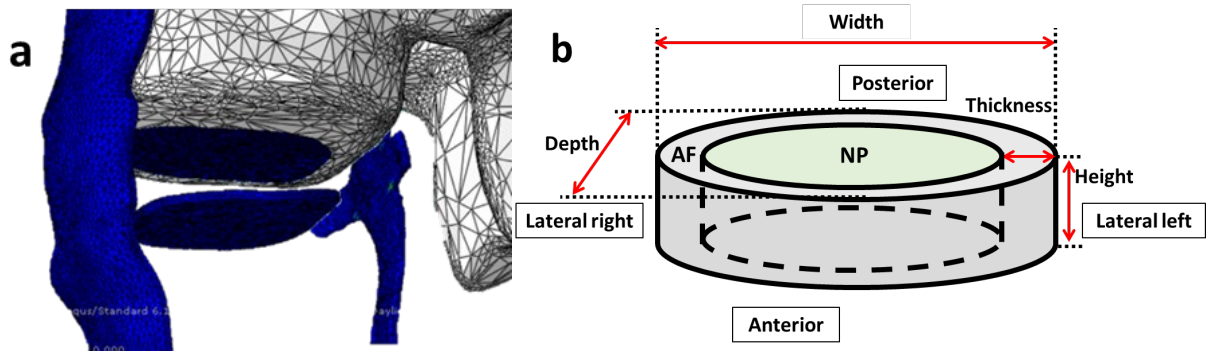

Fig. 3.5a. The FE models and mesh for superior and inferior endplates and anterior and posterior longitudinal ligaments (AF and L_5 are not shown for clarity). **Fig. 3.5b.** AF dimensions at the L_4 and L_5 endplates surfaces' levels in the transverse plane were scaled using ratios relative to the overall width and depth (Table 3.1) measured from the subject-specific radiograph.

Table 3.1

AF thickness ratios (Suárez et al., 2015), dimensions' at L_4 and L_5 endplates surfaces' levels in the transverse planes, and heights at outer periphery (dimensions in mm)

		Anterior	Posterior	Left lateral	Right lateral	Width	Depth
		thickness to depth		thickness to width			
	Ratios	0.145	0.128	0.198	0.186		
L_4 - level	Thickness	5.0	4.4	8.9	8.4	45.0	34.5
L_5 - level	Thickness	4.8	4.2	8.9	8.4	45.0	33.0
	Height	12.2	6.9	11.7	11.6		

Material models of the L_4L_5 spinal unit in the KD-FEM:

The spinal unit components were assigned material properties based on previous studies (Table 3.2). The endplates were assigned a linear elastic isotropic material model (Ayturk et al., 2010). The AF was assigned an anisotropic hyperelastic material model with two families of fibers (Ayturk et al., 2010). The matrix substance was assigned incompressible Yeoh material (third order reduced polynomial) with a strain energy expression as

$$W_{matrix} = C_{10}(I_1 - 3) + C_{20}(I_1 - 3)^2 + C_{30}(I_1 - 3)^3 \quad (3.1)$$

where I_1 is the first invariant of the deviatoric of Cauchy-Green strain tensor (C). The fiber strain energy was represented by exponential function of the fourth ($I_4 = a_0 C a_0$) and sixth ($I_6 = b_0 C b_0$) invariants Cauchy-Green strain tensor.

$$W_{fiber} = \frac{a_3}{b_3}\left(e^{b_3(I_4-1)^2} + e^{b_3(I_6-1)^2} - 2\right) \tag{3.2}$$

where a_0 and b_0 are the direction cosines of the two families of fibers, $C = F^T F$, and F is deformation gradient. The strain energy coefficients of the matrix (C_{10}, C_{20}, C_{30}) and fiber (a_3, b_3) were derived from the experimental tissue testing in the circumferential and axial directions in tension and compression by Ayturk et al. (2010). The total strain energy expression was the sum of the two terms.

$$W = W_{matrix} + W_{fiber} \tag{3.3}$$

This expression was implemented in a Fortran code in ABAQUS using the UANISOHYPER user subroutine. Uniform fiber angles of +/- 30º (circumferential direction) were assigned and the **Orien**t tool was used with a cylindrical C-sys; the fibers were modeled as tension only using conditional statements in the code.

The ligaments were assigned the relatively simple compressible hyperelastic model of Ogden, where the strain energy expression was given by three stretch terms

$$W = \sum_{i=1}^{3}\left[\frac{2\mu_i}{\alpha_i^2}\left(\lambda_1^{\alpha_i} + \lambda_2^{\alpha_i} + \lambda_3^{\alpha_i} - 3\right) + \frac{1}{D_i}(J-1)^{2i}\right] \tag{3.4}$$

where λ_i are the stretch in principal directions, μ_i are the shear moduli, $D_i = 2/K_i$, K_i are the bulk moduli, and J is the Jacobian. The coefficients were derived from an experimental study (Xiao et al., 2011) (Table 3.2).

Table 3.2
Material models' coefficients

Ligaments	μ_1 (MPa)	μ_2 (MPa)	μ_3 (MPa)	α_1	α_2	α_3	D_1 (MPa^{-1})	D_2 (MPa^{-1})	D_3 (MPa^{-1})
ALL	0.177	0.627	-0.357	-3.080	-13.86	-6.8	1	1	1
PLL	0.159	0.770	-0.390	-1.126	-18.54	-9.6	1	1	1
AF	C_{10} (MPa)		C_{20} (MPa)		C_{30} (MPa)		a_3 (MPa)		b_3
	0.0146		-0.0189		0.041		0.03		120
Endplates	E (MPa)		ν		NP	Incompressible fluid, ρ (g/mm^3)			
	23.8		0.4			0.001			

The nucleus pulposus (NP) geometry was defined by the AF and endplates boundaries surrounding the NP space and was not meshed in the KD-FEM. Rather, the **Fluid Cavity** tool in ABAQUS was used to model the NP as pure incompressible fluid with a uniform pressure applied to the AF and endplates boundaries forming the NP space. This tool maintained constant NP volume and enabled computation of the change from the initial applied fluid pressure to maintain constant volume during deformation.

Validation of IVD pressure calculations:

IVD pressures predicted by the pipeline, including the ESN MSD simulation and the KD-FEM, were compared with previously published *in vivo* pressures (Wilke et al., 1999; 2001) and a default DJR MSD model (Bassani et al., 2017) of the same subject. IVD pressures predicted by the different models were compared during a range of 0° to 30° flexion motion and during four different standing and load carrying postures. The IVD pressure in the KD-FEM was calculated as the change in NP fluid pressure during the activity. The IVD pressure in the ESN MSD model was calculated as the average of the two components of the elastic force ($\vec{F}_E$ in Fig. 3.2b) acting perpendicular to endplates surfaces (Jaradat et al., 2022) (Chapter Two). The *in vivo* subject's transverse cross-section area ($18e^{-4}\ m^2$) of L_4L_5 IVD (Wilke et al., 1999; Wilke et al., 2001) and a correction factor (1.54) to account for the NP load carrying contribution were applied

(Brinckmann and Grootenboer, 1991; Nachemson et al., 1960; Bassani et al., 2017). The IVD pressure in the DJR MSD model was reported as the average L_4L_5 IVD pressure, corrected to account for the NP contribution using a correction factor (CF) method (Brinckmann and Grootenboer, 1991; Nachemson et al., 1960) and a quadratic equation (QE) method (Ghezelbash et al., 2016).

The flexion angle definition in the ESN MSD model was based on the system's default input of the thorax-pelvis rotation. This rotation is defined as the rotation of thorax anatomical frame measured from the pelvis anatomical frame (Jaradat et al., 2022) (Chapter Two), where the pressure predictions from the ESN MSD and KD-FEM are all defined based on this rotation. It was necessary to convert the *in vivo* measure pressure data, that is reported relative to the thoracolumbar-sacrum rotation, to this thorax-pelvis rotation, where the methods from a previous study (Jaradat et al., 2022) (Chapter Two) were used. Further, the *in vivo* study does not distinguish the forward and backward flexion motion curves of the *in vivo* study, therefore, the average of the two curves were considered (Jaradat et al., 2022) (Chapter Two). The resulted *in vivo* data curve is shown in Fig. 3.7.

The KD-FE model computations of the IVD pressure

The integration of L_4L_5 spinal unit soft tissue FE models into the KD-FE model allowed the deformable FE computation of the IVD pressure for flexion motion and four different standing and load carrying postures.

KD-FEM of the flexion motion:

The KD-FEM simulation for the 0^o to 30^o flexion motion was conducted in two analysis steps in ABAQUS: the initial configuration step and the motion step. The initial configuration step was defined by the VKS outputs from the ESN MSD simulation for a standing posture at 0^o flexion.

The vertebrae were held fixed at this posture using boundary conditions applied at the reference points associated with each vertebra rigid-body definition. The **Fluid Cavity** tool was used to induce an initial pressure magnitude of 0.732 MPa in the NP, which was the predicted value of the ESN MSD model at this posture and produce initial swelling in the AF and deformation in the ligaments and endplates. The motion step was defined during the 0^o to 30^o of trunk flexion, with the VKS from the ESN MSD simulation used as boundary conditions on the vertebrae reference points to actuate the lumbar KD-FEM. This step started from the initial configuration step and its computed outputs. The fluid cavity pressure changes over the motion, due to the VKS, were predicted by the FE model (Fig. 3.7).

KD-FEM of standing and load carrying postures:

In the *in vivo* study of Wilke et al. (1999; 2001), pressure measurements in several load carrying postures were reported (Fig. 3.8); and in the motion capture study of Bassani et al. (2017) these postures were regenerated by a subject with anthropometrics resembling the *in vivo* study subject's simulated in a matched DJR MSD model to predict the pressures.

The ESN MSD model and KD-FEM were combined to simulate a standing position and three load carrying postures. Three postures (Fig. 3.8): i) standing posture with a load; ii) standing posture holding a 20.0 kg load with arms close to the chest; iii) standing posture holding a 20 kg load with arms extended; and iv) lifting a 20 kg load in a squat position. The FE simulation for each of the load carrying postures was conducted in two analysis steps in ABAQUS software.

The KD-FEM simulation was conducted in two analysis steps in ABAQUS: the initial configuration step and the quasi-static step. The initial configuration step was identical to the initial configuration step in the flexion motion KD-FEM, and all load carrying postures were initiated from the standing posture. The quasi-static step was defined by the ESN MSD simulation

progressing from the single posture standing VKS to the single posture load carrying VKS. To ensure solution convergence, the load carrying VKS were applied incrementally over an arbitrary simulation time (60 sec). The quasi-static analysis excluded the effect of inertia and acceleration forces, which ensured static FE analysis for the load carrying postures (Fig. 3.6).

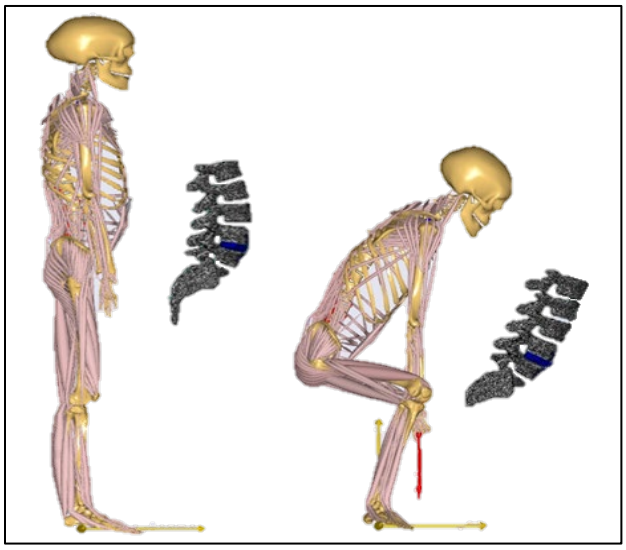

Fig. 3.6. FE analysis of squat load carrying: Initial configuration step at single posture standing MSD VKS, and quasi-static motion step to load carrying posture at single posture squat carrying MSD VKS

Results

Utilizing the general pipeline's methods, the individual VKS were predicted from the body-level motion of 0° to -30° flexion by the *in vivo* subject-matched ESN MSD simulation. From this simulation, the L_4L_5 IVD pressure was computed from the stiffness behavior of the ESN MSD model using the elastic force $\vec{F}_E$ projections perpendicular to the endplate's surfaces. Fig. 3.7 shows the ESN MSD model predicted pressure compared with the *in vivo* measures and with Bassani DJR model pressures over the flexion motion. The ESN curve showed comparability with

an overall RMS value of 0.111 relative to *in vivo* curve; this is comparable with Bassani CF DJR curve with RMS = 0.102 that has higher magnitudes than the QE curve (RMS = 0.223) of about 0.1 to 0.2 MPa over the motion with significant non-smoothness of both curves.

The models showed different non-linearity trends; the KD-FEM model showed the highest nonlinearity with a correlation factor R = 0.7881 while the ESN MSD and *in vivo* curves showed the lowest of R = 0.999 for both curves. The Bassani DJR curves showed in-between R values of 0.991 and 0.993 for the CF and QE curves, respectively, due to their non-smoothness.

The pipeline's 3D modeling and script methods were used to map the ESN MSD lumbar model into its equivalent KD-FEM to enable the deformable FE analysis of the L_4L_5 spinal unit. The applied ESN MSD predicted VKS in the KD-FEM caused changes in the magnitude of the initial IVD pressure due to the deformations induced by the VKS, where the pressure magnitude predicted by the ESN MSD model at standing posture was used as the initial pressure of 0.732 MPa. Fig. 3.7 shows the KD-FEM predicted pressure compared with other curves, which showed a comparable value of the RMS of 0.101. The KD-FEM curve starting from the ESN MSD curve extended around *in vivo* curve closer than the ESN MSD model and approaching it back at higher flexion angle. Small changes in VKS in the L_4L_5 spinal unit during trunk flexion, as computed by the ESN MSD model, produced a non-linear response in the IVD pressure predictions from the KD-FEM that was notably different from the linear response of the ESN MSD model (Fig. 3.7). While both models had an initial IVD pressure of 0.732 MPa at the standing posture (0^o flexion), pressures output by the KD-FEM were decreased over the initial -15^o of thorax-pelvis flexion compared to linearly increasing pressures output by the ESN MSD model.

The KD-FEM predictions of IVD pressure had greater non-linearity (R = 0.788) than the curves from *in vivo* sensors and the MSD models (Fig. 3.7). That deviation was likely due to the

different material models, as already described, and different pressure computation methods in the L_4L_5 spinal unit. The KD-FEM approach used the **Fluid Cavity** tool, which distributed the IVD pressure over the common boundary between the NP, AF and the endplates to capture the effect of the local material deformations at these boundaries. It calculated the change in IVD pressure due to those deformations while maintaining a constant NP volume as an incompressible fluid. In contrast, *in vivo* IVD pressure was measured at the center of NP in the study subject, which could explain the difference in the non-linearity compared with the KD-FEM. The DJR MSD models from Bassani, et al. (2017) had very little non-linearity (R ~ 0.99), possibly due to noise and measurement uncertainty common in optical motion capture systems rather than actual predictions of non-linear IVD pressure variations over the flexion range. The range of IVD pressures predicted by the KD-FEM (0.67 to 1.13 MPa) was similar to the *in vivo* range (0.54 to 1.08 MPa) and the IVD pressures predicted by the ESN MSD model (0.73 to 1.12 MPa).

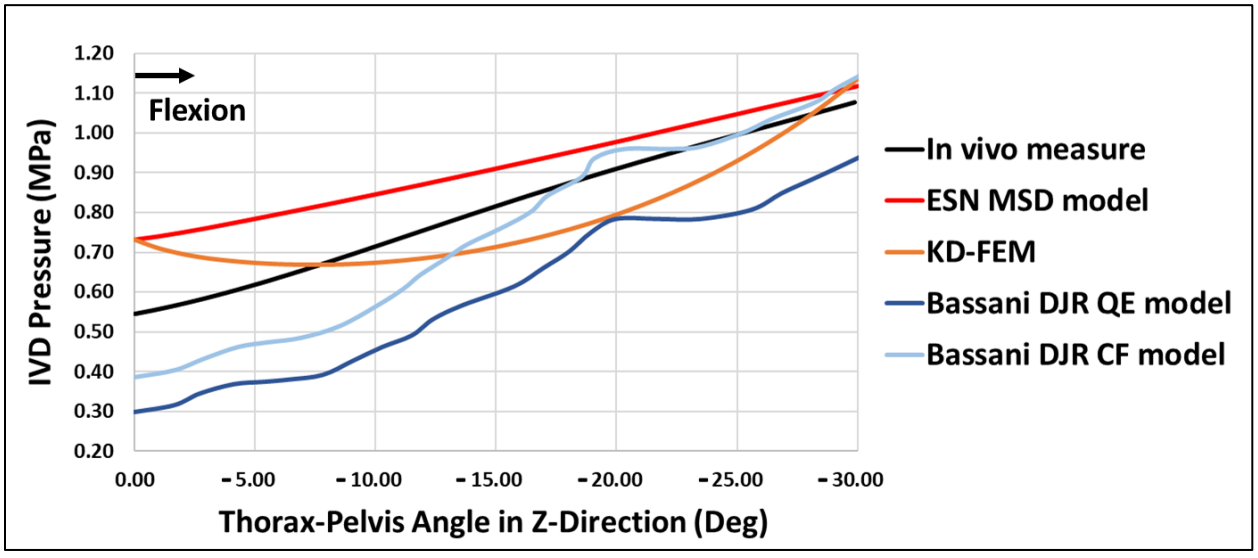

Fig. 3.7. IVD pressure predictions in flexion range of motion

Utilizing the pipeline's methods to predict the IVD pressures at the three load carrying postures, the different methods showed comparable predictions as shown in Fig. 3.8. In standing position, the KD-FEM was assigned the (initial) ESN MSD pressure prediction that was higher than the *in vivo* measures by about 0.2 MPa compared with Bassani DJR models predictions that were lower by 0.1 to 0.2 MPa.

At the close-to-chest load holding position, the KD-FEM prediction was higher about 0.21 MPa than the *in vivo* measure and other models reported magnitudes 0.1 to 0.3 MPa lower with Bassani CF DJR model closest to the *in vivo* measure. For the arms-extended load holding position, the KD-FEM model prediction was the closest to and higher by about 0.1 MPa than the *in vivo* measure while other models reported lower magnitudes with Bassani QE DJR model lowest with about 0.45 MPa lower. At the lifting squat load position, the KD-FEM predictions were the highest and of about 0.21 MPa from the *in vivo* measure while the ESN MSD model was the lowest of about 0.26 MPa from the *in vivo* measure.

The multi-scale pipeline proved sensitive to small changes in VKS. For example, the 0.40 MPa change in IVD pressure in the KD-FEM occurred with -0.12 mm of superior-inferior Y-translation over the flexion range.

Table 3.3
Relationship between L_4L_5 VKS outputs from the ESN MSD model and IVD pressure outputs from the KD-FEM; changes are referenced from the standing 0° flexion posture

	ESN MSD Model		KD-FEM
Activity	Change in X-translation (mm)	Change in Y-translation (mm)	Change in IVD pressure (MPa)
0° to -30° flexion	0.15	-0.12	0.40
Load close to chest	-0.02	-0.04	0.48
Load arms extended	-0.11	-0.10	1.14
Load squat lifting	0.35	-0.21	1.18

In the standing posture, the IVD pressure magnitudes in the ESN MSD model and KD-FEM were identical because the KD-FEM used the initial pressure magnitude predicted by the ESN MSD model. The KD-FEM predicted IVD pressures for the close-to-chest and arms-extended loading postures were 27% lower and 4% higher than the *in vivo* measurements, respectively. These deviations were comparable to the magnitudes predicted by the ESN MSD and DJR MSD (Fig. 3.8). The KD-FEM IVD pressure predictions for the lifting squat load posture were 12% higher than the *in vivo* measurements (Fig. 3.8 and 3.9), although the thorax-pelvis rotation at this position was not reported by the *in vivo* study. Altering the thorax-pelvis flexion angle by 5^{o} (increasing it from 30^{o} to 35^{o}) increased the predicted IVD pressure by approximately 15% (from 1.91 MPa to 2.2 MPa) in the KD-FEM. This showed the sensitivity and responsivity of the pipeline's methods to critical parameters in a load carrying posture.

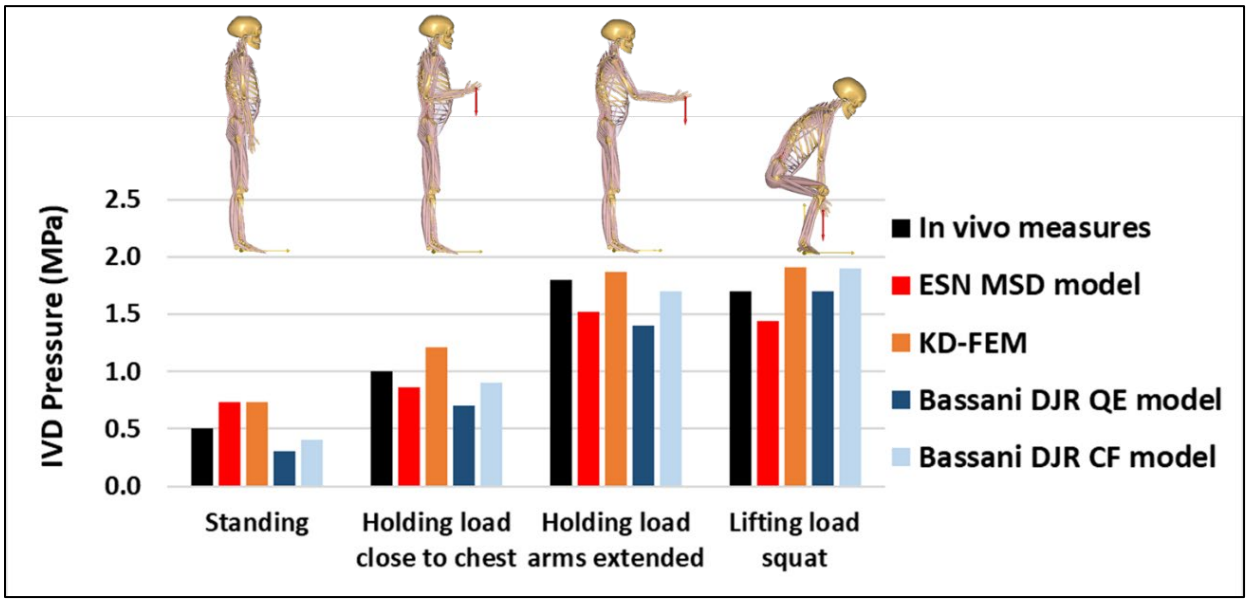

Fig. 3.8. IVD pressure predictions in standing and loading postures

Fig. 3.9 demonstrate the responsivity of the pipeline's modeling methods to different parameters of the simulations' models. The thorax-pelvis rotation at the squat load lifting posture

was varied from 30° to 35° flexion, which resulted in a 0.04 MPa and 0.32 MPa increase in the ESN MSD and KD-FE models predictions, respectively.

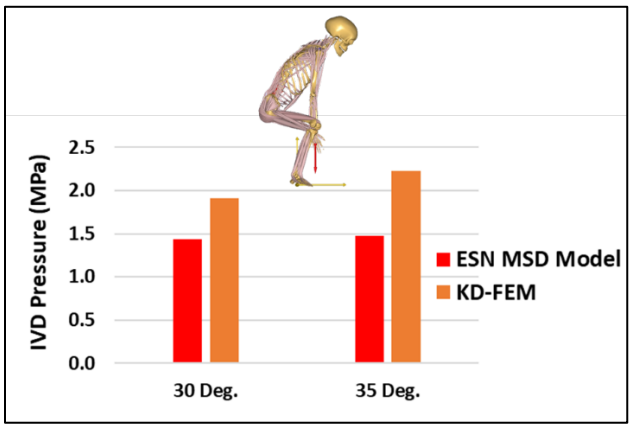

Fig. 3.9. IVD pressure variation, in L_4L_5 unit, with thorax-pelvis angle at squat load lifting posture

Discussion and conclusions

The multi-scale pipeline of computational simulations developed in this study used subject-specific models and body-level motions to non-invasively assess spine tissue behavior. The general pipeline (Fig. 3.1) combined the ESN MSD model's capability for calculating VKS during activities of daily living with the KD-FEM's capability for analyzing deformation of soft tissues in the lumbar spine. Specifically, it successfully mapped subject-specific anthropometrics and lumbar VKS predicted by the ESN MSD model into its equivalent KD-FEM with identical kinematic behaviors for both models. Multi-scale attributes of the pipeline were demonstrated, including the use of body-level motion inputs acquired during activities of daily living to generate individual VKS defining organ-level (spinal unit) motions. In addition, IVD behavior was modeled as spinal unit forces and moments in an MSD framework and modeled as tissue-level stresses and strains in a FE modeling framework. The scripting tool automated the mapping procedure, which

has implications for error reduction and time-savings and represents a necessary step toward future clinical implementation.

The basic concept interlaced through this multi-scale pipeline was that vertebral kinematics occurring with body-level motions are the physical cause of internal loads and deformation in spine soft tissues. The general pipeline directly mapped the VKS and subject-specific anatomy into the KD-FEM, which supported integration of material models to predict soft tissue behavior. As proof-of-concept, this pipeline supported analysis of IVD behavior in different load-carrying postures associated with common activities of daily living. Specifically, the KD-FEM predicted IVD pressures that were comparable to *in vivo* measures and previous published models (Fig. 3.7). While the current study assigned published material models for the vertebral endplates, the AF and NP, and longitudinal ligaments (Table 3.2), this pipeline can be easily generalized to other tissue properties and activities. For example, it has potential for analysis of alternative soft tissue models representing endplate or disc properties that are altered due to aging or degenerative diseases (Ibarz et al., 2013).

Inclusion of elastic material properties in the L_4L_5 spinal unit produced a non-linear response in KD-FE models that was notably different from the linear response of the ESN MSD model, with an initial decrease in IVD pressure over the initial -15^o of thorax-pelvis flexion (Fig. 3.7). This response was likely due to the initial wedge shape of the L_4L_5 IVD and higher deformation in the posterior quadrant (Fig. 3.10) with the spinal unit in extension (0^o flexion). During the initial flexion motion up to -15^o thorax-pelvis angle, local changes in the VKS of the L_4L_5 spinal unit (2.41^o reduction in the local relative extension angle in the sagittal plane in L_4L_5 unit) reduced the strain in the AF and consequently lowered the NP pressure predicted by the KD-FEM. However, with increasing flexion beyond -15^o, the decreased superior-inferior (SI) distance

between the L_4L_5 vertebrae caused the IVD pressure in the KD-FEM to increase back to the same magnitude of the ESN MSD model at -30^o flexion.

Although the effect of altered shear stiffness on IVD pressure was beyond the scope of the current study, it was evident that small changes in VKS have implications for the shear loads and stiffness affecting the IVD pressure predictions (Table 3.3). The ESN MSD model mainly depended on the compressive stiffness to compute the pressure, with only a small contribution from the shear stiffness to overall optimization solution. However, the VKS (X-translations) output from the ESN MSD model directly influenced the deformation of the AF in the KD-FEM and altered the IVD pressure accordingly. Considering that both compressive and shear stiffness are commonly altered by aging or degenerative changes to disc tissue properties (Ferguson et al., 2003; Vo et al., 2016) this multi-scale pipeline is suitably formulated for future work on that topic.

The KD-FEM supported multi-scale modeling in a manner that was different than the approach used in conventional, stand-alone MSD models. The KD-FEM captured the role of the AF to distribute the IVD loads over the vertebrae endplate surfaces and impact IVD pressures due to compressive and shear loads. Specifically, it captured the effects of local tissue behavior in the L_4L_5 spinal unit through detailed geometric and material models that are well-characterized in the scientific literature, including the distinct properties of the AF matrix and fibers, the endplates, and the longitudinal ligaments (Table 3.2). In contrast, the MSD models used the joint reaction force (DJR MSD) or elastic forces (ESN MSD) computed by the MSD system. Those forces were oriented perpendicular to the endplate's surfaces, but were exerted as a point average, and without including the elasticity in the shear directions in the ESN MSD model or the elasticity in all directions in the DJR MSD models (Jaradat et al., 2022) (Chapter Two).

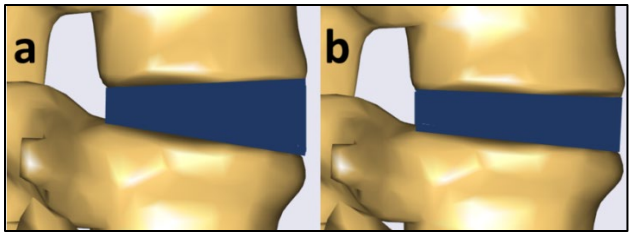

Fig. 10. The reduction in the IVD wedge shape, in L_4L_5 unit, in flexion from 0º (a) to -30º (b) of thorax-pelvis angle

This multi-scale computational pipeline was robust to changes in both motion and load boundary conditions, including trunk flexion (Fig. 3.7) and static loads (Fig. 3.8). Unlike load-driven FE modeling approaches in which load carrying postures alter the loads generated at the L4-L5 spinal unit, the approach used in the current study was dependent upon the sensitivity of the VKS in the ESN MSD model to static loads, which in turn, altered the IVD pressure predictions in the KD-FEM. This sensitivity was assessed by applying different load boundary conditions to the ESN MSD model. As expected, adding the 20 kg external load to the ESN MSD model in the various load-carrying postures altered the predicted VKS and the corresponding IVD pressure calculations in the KD-FEM. For example, simply adding 20 kg in a standing posture (holding load close to chest) produced an 66% increase in IVD pressure relative to the standing position (without load). IVD pressure predictions from the KD-FEM were comparable to *in vivo* measurements of disc pressure in those load-bearing postures (Fig. 3.8).

The modeling approach used in this multi-scale pipeline has both strengths and limitations. i) All models (KD-FEM, ESN MSD, and DJR MSD) were subject-specific for the same subject used to generate the *in vivo* data, which supported direct comparison of model outputs and provided a considerable advantage for validating the pipeline outputs. ii) This modeling approach did not require detailed imaging to generate a validated subject-specific anatomical model. Rather, critical subject-specific anatomy (e.g., body-level scaling of the musculoskeletal system, organ-level

scaling of the IVD) was combined with generalized parameters from the scientific literature (e.g., predefined bone shapes within the MSD software, thickness of AF and ligaments). iii) Motion capture of body-level postures *in vivo* were sufficient for predicting VKS in the ESN MSD model using stiffness functions and for actuating the KD-FEM. iv) Comparison of the *in vivo* IVD pressure measurements and pressure predictions from the ESN MSD model provided verification for the VKS, which were predicted using the stiffness functions in that model.

Works Cited

Aiyangar, A.K., Zheng, L., Tashman, S., Anderst, W.J., Zhang, X. 2014. Capturing three-dimensional in vivo lumbar intervertebral joint kinematics using dynamic stereo-X-ray imaging. J. Biomech. Eng. 136 (1), 011004.

Alemi, M. M., Burkhart, K. A., Lynch, A. C., Allaire, B. T., Mousavi, S. J., Zhang, C., Bouxsein, M. L., Anderson, D. E. 2021. The influence of kinematic constraints on model performance during inverse kinematics analysis of the thoracolumbar spine. Front. Bioeng. Biotechnol. 9:688041.

Amiri, S., Naserkhaki, S., Parnianpour, M. 2018. Modeling and validation of a detailed FE viscoelastic lumbar spine model for vehicle occupant dummies. Computers in Biology and Medicine. 99: 191-200.

Anderst, W.J., West, T., Donaldson, W. F., Lee, J. Y., Kang, J. D. 2016. A Longitudinal study of the six degrees of freedom cervical spine range of motion during dynamic flexion/extension and rotation after single-level anterior arthrodesis. Spine (Phila Pa 1976). 41(22).

Ayturk, U. M., Garcia, J. J., Puttlitz, C. M. 2010. The micromechanical role of the annulus fibrosus components under physiological loading of the lumbar spine. Journal of Biomechanical Engineering, Vol. 132 / 061007-1.

Bassani, Ta., Stucovitz, E., Qian, Z., Briguglio, M., Galbusera, F., 2017. Validation of the AnyBody Full Body Musculoskeletal Model in Computing Lumbar Spine Loads at L4L5 Level". 2017, April, Journal of Biomechanics 58 (2017) 89-96.

Cheng, B., Castellvi, A. E., Davis, R. J., Lee, D. C., Lorio, M. P., Prostko, R. E. 2016. Variability in flexion extension radiographs of the lumbar spine: a comparison of uncontrolled and controlled bending. Int. J. Spine Surg. 10:20.

Colyer, SL., Evans, M., Cosker, DP., Salo, AIT. 2018. A Review of the Evolution of Vision-Based Motion Analysis and the Integration of Advanced Computer Vision Methods Towards Developing a Markerless System. Sports Med Open. 4(1):24.

Cunningham, B. W., Kotani, Y., McNulty, P. S., Cappuccino, A., McAfee, P. C. 1997. The effect of spinal destabilization and instrumentation on lumbar intradiscal pressure: an *in vitro* biomechanical analysis. Spine (Phila Pa 1976). 22(22):2655-63.

Damsgaard, M., Rasmussen, J., Christensen, S. T., Surma, E., De Zee, M. 2006. Analysis of musculoskeletal systems in the AnyBody Modeling System, Simulation Modelling Practice and Theory. Volume 14, Issue 8, Pages 1100-1111.

Delp, S. L., Anderson, F. C., Arnold, A. S., Loan, P., Habib, A., John, C. T., Thelen, D. G. 2007. OpenSim: open-source software to create and analyze dynamic simulations of movement. IEEE transactions on biomedical engineering, 54(11), 1940-1950.

Fagan, M. J., Julian, S., Mohsen, A. M. 2002a. Finite element analysis in spine research. Proceedings of The Institution of Mechanical Engineers Part H 216, 281–298.

Fagan, M. J., Julian, S., Siddall, D. J., Mohsen, A. M. 2002b. Patient-specific spine models. Part1: Finite element analysis of the lumbar intervertebral disc: A material sensitivity study. Proceedings of The Institution of Mechanical Engineers PartH216, 299–314.

Fujii, R., Sakaura, H., Mukai, Y., Hosono, N., Ishii, T., Iwasaki, M. 2007. Kinematics of the lumbar spine in trunk rotation: in vivo three-dimensional analysis using magnetic resonance imaging. Eur. Spine J. 16, 1867–1874.

Ghezelbash, F., Shirazi-Adl, A., Arjmand, N., El-Ouaaid, Z., Plamondon, A. 2016. Subject-specific biomechanics of trunk: musculoskeletal scaling, internal loads and intradiscal pressure estimation. Biomech. Model. Mechanobiol. 15 (6), 1699–1712.

Guo, L-X., Zhang, C. 2022. Development and Validation of a Whole Human Body Finite Element Model with Detailed Lumbar Spine, World Neurosurgery.

Jaradat, M. G., Harman, M. K., McHenry, T. P., Yao, H. 2022. Predicting non-constrained vertebral kinematics in musculoskeletal dynamic simulations from body-level extension-flexion motion: Validation of a reformulated lumbar spine model. Journal of Biomechanical Engineering, In Submission.

Jones, A. C., Wilcox, R. K. 2008. Finite element analysis of the spine: Towards a framework of verification, validation and sensitivity analysis. Medical Engineering and Physics30, 1287–1304.

Kaneoka, K., Ono, K., Inami, S., Hayashi, K. 1999. Motion analysis of cervical vertebrae during whiplash loading. Spine, volume 24, number 8, pp 763-770.

Li, G., Wang, S., Passias, P., Xia, Q., Li, G., Wood, K. 2009. Segmental in vivo vertebral motion during functional human lumbar spine activities. Eur. Spine J.18, 1013–1021.

Lin, C-C., Lu, T-W., Wang, T-M., Hsu, C-Y., Hsu, S-J., Shih, T-F. 2014. In vivo three-dimensional intervertebral kinematics of the subaxial cervical spine during seated axial rotation and lateral bending via a fluoroscopy-to-CT registration approach. Journal of Biomechanics 47(2014) 3310-3317.

Manchikanti, L., Singh, V., Datta, S., Cohen, S. P., & Hirsch, J. A. 2009. Comprehensive review of epidemiology, scope, and impact of spinal pain. Pain physician, 12(4), E35-70.

Natarajan, R. N., Williams, J. R., Andersson, G. B. J. 2004. Recent Advances in Analytical Modeling of Lumbar Disc Degeneration, Spine: Volume 29 - Issue 23 - p 2733-2741.

Nachemson, A. 1960. Lumbar intradiscal pressure. Experimental studies on postmortem material. Acta Orthop. Scand. Supplementum 43, 1–104.

Panjabi, M. M. 2003. Clinical spinal instability and low back pain. Journal of electromyography and kinesiology, 13(4), 371-379.

Pitzen, T., Schmitz, B., Georg, T., Barbier, D., Beuter, T., Steudel, W. I., Reith, W. 2004. Variation of Endplate Thickness in the Cervical Spine. Eur. Spine J. 13: 235–24.

Rohlmann, A., Pohl, D., Bender, A., Graichen, F., Dymke, J. 2014. Activities of Everyday Life with High Spinal Loads. PLoS ONE 9(5): e98510.

Rohlmann, A., Zander, T., Rao, M., Bergmann, G. 2009. Realistic loading conditions for upper body bending. JBiomech; 42:884–90.

Sato, K., Kikuchi, S., Yonezawa, T. 1999. In vivo intradiscal pressure measurement in healthy individuals and in patients with ongoing back problems. Spine 24(23):2468–74.

Schmidt, H., Galbusera, F., Rohlmann, A., Shirazi-Adl, A. 2013. What have we learned from finite element model studies of lumbar intervertebral discs in the past four decades? Journal of Biomechanics, Volume 46, Issue 14, Pages 2342-2355.

Schmoelz, W., Huber, J. F., Nydegger, T., Claes, L., Wilke, H. J. 2006. Influence of a dynamic stabilization system on load bearing of a bridged disc: an *in vitro* study of intradiscal pressure. Eur Spine J. 15(8):1276-85.

Somasundaram, K., Zhang, L., Sherman, D., Begeman, P., Lyu, D., Cavanaugh, JM. 2019. Evaluating thoracolumbar spine response during simulated underbody blast impact using a total human body finite element model. Journal of the Mechanical Behavior of Biomedical Materials. 100.103398.

Staub, B. N., Holman, P. J., Reitman, C. A., Hipp, J. 2015. Sagittal plane lumbar intervertebral motion during seated flexion-extension radiographs of 658 asymptomatic non degenerated levels. J Neurosurg Spine 23:731–738.

Suárez, H. E. J., Gomez, L., García, J.J. 2015. A finite element model of the L4-L5-S1 human spine segment including the heterogeneity and anisotropy of the discs. Acta of bioengineering and biomechanics / Wroclaw University of Technology. 17(2):15-24.

Van-Rossum, G., Drake, F. L. 2009. Python 3 Reference Manual. CreateSpace, Scotts Valley, CA.

Wang, H., Zhou, C., Yu, Y., Wang, C., Tsai, T.-Y., Han, C. 2020. Quantifying the ranges of relative motions of the intervertebral discs and facet joints in the normal cervical spine. J. Biomech. 112:110023.

Wang, S., Xia, Q., Passias, P., Li, W., Wood, K., and Li, G., 2011, "How Does Lumbar Degenerative Disc Disease Affect the Disc Deformation at the Cephalic Levels In Vivo?," Spine, 36(9), pp. E574–E581.

Wang, S., Xia, Q., Passias, P., Wood, K., and Li, G., 2009, "Measurement of Geometric Deformation of Lumbar Intervertebral Discs Under In-Vivo Weightbearing Condition," J. Biomech., 42(6), pp. 705–711.

Wilke, H-J., Neef, P., Caimi, M., Hoogland, T., Claes, L., 1999. New In Vivo Measurements of Pressures in the Intervertebral Disc in Daily Life. SPINE Volume 24, Number 8, pp 755–762, 1999.

Wilke, H-J., Neef, P., Hinz, B., Seidel, H., Claes, L., 2001. Intradiscal Pressure Together with Anthropometric Data – A Data Set for Validation of Models". Clinical biomechanics 16 supplement No. 1 (2001) S111-S126.

Xiao, Z., Wang, L., Gong, H., Zhu, D., Zhang, X. 2011. A non-linear finite element model of human L4-L5 lumbar spinal segment with three-dimensional solid element ligaments. Theoretical and applied mechanics letters 1, 064001.

Yeager, M. S., Cook, D. J., Cheng, B. C. 2013. Reliability of computer-assisted lumbar intervertebral measurements using a novel vertebral motion analysis system. Spine J. 14(2):274-81.

CHAPTER FOUR

MULTI-LAYERED MULTI-PHASE CANAL FINITE ELEMENT MODEL OF LUMBER SPINE KINEMATICALLY-DRIVEN BY MUSCULOSKELETAL DYNAMICS-PREDICTED VERTEBRAL KINEMATICS FROM BODY-LEVEL MOTION: APPLICATION TO L_4 VERTEBRAL FORAMEN STENOSIS ANALYSIS

Introduction

The soft tissues of the human spine are sensitive to small stresses and deformation that are caused by the relative kinematics between vertebrae. The spinal canal tissues are also sensitive to the narrowing of a stenotic canal. However, clinical assessments are insufficient for detecting stenosis risks arising from the vertebral-level kinematics induced during common ranges of motion. Patient-reported symptoms are generally associated with basic body postures, and CT-myelography and MRI imaging are used to detect cord or cauda equina pressure at certain postures under applied axial compression (Willen et al., 1997; Costandi et al., 2015). However, radiological changes are not always predictive of clinical symptoms and heightened risks of low back pain and sciatica with progressive stenosis and clinical instability are difficult to predict (Denteneer et al., 2017; Fritz et al., 2005). There are few tools for quantifying changes in stenotic spines at the tissue-level during dynamic motion and for predicting the risks that consider its future progression.

Existing computational models of the spinal canal commonly include simplifications for computational efficiency (Alemi et al., 2021), and therefore, do not capture detailed changes at the tissue level caused by stenosis. Moreover, they are generally load-driven models that use average loads applied as contact forces rather than displacement-driven models that use vertebral kinematics to generate deformations and pressure in the canal (Schonstrom et al., 1988). Introduction of new methods for measuring *in vivo* vertebral kinematics (VKS), such as dynamic magnetic resonance imaging or dual-plane fluoroscopy, has heightened awareness about the

critical role of VKS in pathological conditions (Lin et al., 2014; Anderst et al., 2016; Wang et al., 2011; Fujii et al., 2007; Staub et al., 2015; Li et al., 2009; Aiyangar et al., 2014; Kaneoka et al., 1999; Wang et al., 2009; Cheng et al., 2016; Wang et al., 2020; Yeager et al., 2013). However, these measurements are not widely used in clinical work frames and the imaging systems are limited in the types of motions that can be analyzed. Musculoskeletal dynamics simulations (MSD) are an alternative approach that have the potential advantages of being non-invasive and able to predict individual VKS from body-level motions corresponding to daily activities. This modeling approach has potential clinical significance for aiding detection of clinical instability in the lumbar spine and altered IVD behavior.

The purpose of this study was to quantify risks to spinal canal tissues due to the vertebral kinematics and progressive canal narrowing (stenosis). The approach integrates a detailed multi-layered multi-phase lumbar canal soft tissues FE model into a lumbar vertebrae kinematics-driven FE model (KD-FEM) created using a pipeline of computational simulations developed in previous study (Jaradat et al., 2022b) (Chapter Three). The pipelines methods map the subject-specific MSD vertebrae model into its equivalent FE model actuated with the MSD-predicted VKS from body-level motion to be used to conduct deformable spine FE tissue analysis.

This approach will enable distinct computation and detection of changes in five proposed stenosis measures: i) the anterior-posterior (AP) dura and cauda equina diameters; ii) the transverse cross-sectional area of the dura and cauda equina; iii) the transverse cross-sectional area aspect ratio for both dura and cauda equina; iv) the mechanical stress, strain, and pressure in dura and cauda equina, v) cerebrospinal fluid pressure (CSF), in addition to the contact between the dura and cauda equina. These measures were detected at two locations on the dura and cauda equina, including at the L_4 vertebral foramen level and at the center of L_4L_5 IVD level. These stenosis

measures support detection of minute changes resulting from the VKS over a range of body motions. Model outputs included the stenosis measures during 0^o to 30^o trunk flexion motion and comparison of three clinically relevant degrees of progressive stenosis of the bony vertebral foramen at the L4 level.

Methods

A detailed lumbar canal FE model was created in this study and integrated into a general kinematics-driven FE model (KD-FEM) of lumber spine from a previous study (Jaradat et al., 2022b) (Chapter Three) developed for spine soft tissue FE analysis (Fig. 4.1a G & Fig. 4.1b J). The KD-FEM was created using a simulation tool (Jaradat et al., 2022b) (Chapter Three) that consisted of a pipeline of computational simulations, 3D modeling, and script tools developed to automate the processes (Fig. 4.1a). The pipeline maps a subject-specific MSD lumbar spine model, which consists of lumbar vertebrae driven by vertebral kinematics (VKS), into its equivalent KD-FEM. This mapping utilizes the FE modeling capability of deformable material analysis that is not available in MSD systems that are based on rigid body dynamics. The KD-FEM consisted of lumbar vertebrae specific to the subject of the MSD model driven by vertebral kinematics (VKS) predicted by the MSD model from body-level motion (Fig. 4.1a G) (Jaradat et al., 2022b) (Chapter Three).

The MSD simulations was used to enable the tissue-level assessment of spinal canal behavior corresponding to body-level daily-life activities from which the MSD system computes the individual VKS of the lumbar spine (Fig. 4.1a C). The existing MSD lumbar model was modified in a previous study (Jaradat et al., 2022a) (Chapter Two) in order to compute realistic VKS and was named the elastic surface nodes (ESN) MSD lumbar model (Fig. 4.1a B & C).

The pipeline's methods use i) the MSD model available through the AnyBody Managed Repository (©2022 AnyBody Technology A/S, Aalborg, Denmark) modified to the ESN MSD model, ii) 3-Matic 3D modeling software available through Materialise innovation suite (©2022 Materialise NV, Leuven, Belgium); iii) programing language Python (Van Rossum, G. & Drake, F.L., 2009. Python 3 Reference Manual, Scotts Valley, CA: CreateSpace); and iv) ABAQUS the FE software (v6.14, Dassault Systemes, Waltham, MA) (Jaradat et al., 2022b) (Chapter Three).

The custom Python script was designed (Jaradat et al., 2022b) (Chapter Three) to reduce the lengthy, numerous, and susceptible-to-error mapping process steps. The script integrates the ESN VKS into the KD-FE model as kinematics boundary conditions and prepare the model's Input file ready to be run in ABAQUS FE software (Fig. 4.1a F).

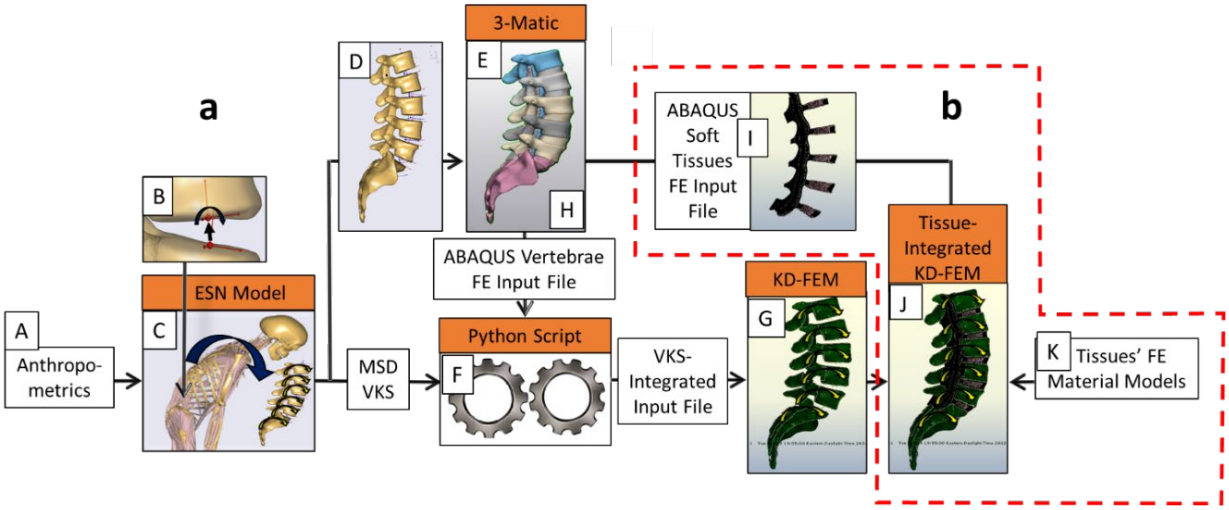

Fig. 4.1a. The general pipeline's steps, inputs, and outputs: A) measured subject specific anthropometrics, B) elastic surface nodes (ESN) lumbar spine MSD model (Jaradat, et al., 2022a) (Chapter Two), C) input anthropometrics into ESN MSD model and output individual VKS over motion range, D) output subject-specific ESN lumbar vertebral geometry (STL file) at initial posture and E) input into 3-Matic 3D modeling software; output vertebrae surface FE mesh in a preliminary ABAQUS Input file, F) input individual VKS and ABAQUS Input file into Python script and output Input file integrated with the VKS, G) Run Input file in ABAQUS FE package to create the kinematics-driven FE model (KD-FEM); **Fig. 4.1b.** H) create the geometries of canal components and IVDs in 3-Matic software based on vertebrae at initial posture, I) output the geometries and FE mesh into an ABAQUS Input file format, J) integrate the canal components and IVDs into the KD-FEM, and K) implement FE material models for tissue components.

The ESN MSD lumbar spine model

The ESN MSD lumbar model was modified from the standard human body MSD model with the anatomical data that corresponds to the 50th percentile size of the European male. This existing model included the constraints of spherical joints and spinal rhythm in lumbar spine and was named the default joint and rhythm (DJR) MSD lumbar model. The DJR MSD model (Fig. 4.2a) was modified to remove the non-physical vertebral kinematics constraints and include the elastic behavior of the lumbar spinal units (Jaradat et al., 2022a) (Chapter Two). The spherical joint and its pivot constraint on the VKS relative translation and rotation were removed; the spinal rhythm and its prescribing of the rotational VKS as system input were also removed.

The ESN MSD model was created based on novel surface nodes created at the centers of the endplates' surfaces and with associated C-sys frames aligned (x-z plane) parallel to the endplates' surfaces (Fig. 4.2b). Elastic forces $\vec{F}_E$ and moments $\vec{M}_E$ were modeled between the surface nodes, and their magnitudes were computed by multiplying the measured VKS by stiffness functions fitted from *in vitro* and FE studies (Jaradat et al., 2022b) (Chapter Three). The VKS of the spinal unit were defined and measured as the translation of the upper surface node and the rotation of its C-sys frame measured from the lower surface node's C-sys frame (Fig. 4.2b). The thorax-pelvis rotation was used as the kinematic input that actuates the lumbar model in the MSD system; this rotation is defined as the thoracolumbar joint or the thorax anatomical frame rotation relative to the pelvis anatomical frame.

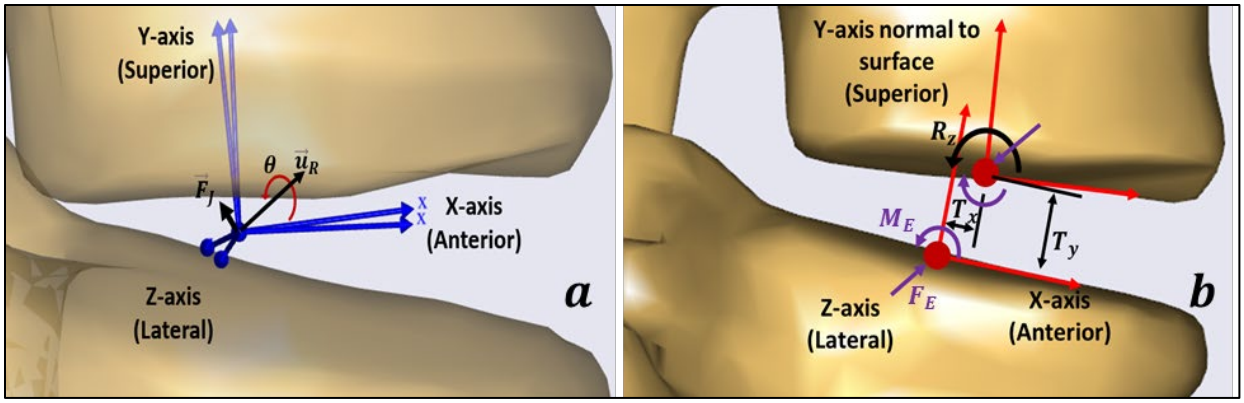

Fig. 4.2a. Spinal units in the DJR MSD model include the spherical joint's two coincident nodes, their local C-sys frames, joint rotation's rotation vector and angle, and joint reaction force. **Fig. 4.2b.** Spinal units in the ESN MSD model include surface nodes at endplates centers, their surface-aligned C-sys frames (in red), spinal unit VKS measures definitions (in black), and stiffness forces and moments (in purple) (Jaradat et al., 2022a) (Chapter Two).

The subject-specific ESN MSD model

The ESN MSD model was matched to the *in vivo* study's subject of Wilke et al. (1999; 2001) for its validation in a previous study (Jaradat et al., 2022a) (Chapter Two), where the *in vivo* measured IVD pressure during body-level motions were used in the validation methods. In this study, the ESN MSD model was also matched to the *in vivo* subject using the same methods of a previous study (Jaradat et al., 2022a) (Chapter Two)and adapting tools of the MSD system, where model was matched to the subject's height, weight, and fat percentage (70 Kg, 173.9 cm, and 11.81% respectively). Further, the detailed subject's anatomical landmarks were used to compute precise scaling factors for different individual body segments, and the available sagittal cross-section image was utilized to determine scaling factors for the lumbar vertebrae geometries (Jaradat et al., 2022a) (Chapter Two). The matching of the ESN MSD model to the *in vivo* subject led to a mapped KD-FE lumbar model that is also matched to the *in vivo* subject enforced by the pipeline's methods (Jaradat et al., 2022b) (Chapter Three).

Geometries and FE mesh

The 3D modeling 3-Matic software was used to create the geometries and mesh of lumbar spine. For the KD-FEM vertebrae, the subject-specific lumbar vertebrae geometries were imported from the MSD model at the standing 0^{o} flexion posture into the 3D modeling software 3-Matic (STL files) (Fig. 4.1a D). The 3-Matic software's meshing tools were used to create surface meshes for the vertebrae that were used in rigid-body definitions the FE analysis and output them in a preliminary ABAQUS Input analysis file (Fig. 4.1a E). The Input file included the necessary ABAQUS keywords for the definitions of parts, assembly instances, meshes, volumes, sections, and surfaces. The naming scheme for these surfaces created in 3-Matic was used in the FE analysis for the attachments and contacts of the vertebrae with soft tissues components (Jaradat et al., 2022a) (Chapter Two).

For the spinal canal and IVD, an MRI for the *in vivo* subject was not available, therefore in this study, the 3-Matic software was used to manually create the geometries for the lumbar spine canal constituents based on the space between the vertebrae and estimated from general lumbar canal images (Fig. 4.1a E). Fig. 4.3 shows the different geometries of the constituents; the posterior longitudinal ligament (PLL) and ligamentum flavum (LF) were modeled with a uniform thickness of 1 mm, and the dura sac-like matter and cauda equina were modeled with uniform (circular) diameters, for simplicity. The dura outer diameter and cauda equina diameter were roughly estimated as 6.5 and 4 mm, respectively, with a uniform thickness of 0.5 mm for the dura matter. The two fat layers were modeled simply based on the space between the dura outer surface and other components in the canal, as shown in Fig. 4.3. The annulus fibrosus (AF) and nucleus pulposus (NP) depth and width ratios were considered from the study of Suárez et al. (2015).

The 3-Matic software's meshing tools were used to create the volume mesh for the canal constituents and output them in an ABAQUS canal tissue Input analysis file (Fig. 4.1 I). The Input file includes the necessary ABAQUS keywords for the definitions of parts, assembly instances, meshes, volumes, sections, and surfaces. The naming scheme for these surfaces created in 3-Matic was used in the FE analysis for the attachments and contacts of the vertebrae with soft tissues components. This Input file was integrated into the KD-FEM creating the full lumbar kinematics-driven FE spine model with canal and IVD soft tissues geometries and mesh (Fig. 4.1b J). The number of elements at which the FE solution converged to the same magnitudes were about, 73,000, 95,500, 80,000, 62,500, 56,000, 90,000 and 216,000 elements for the PLL, sum of all parts of LF, Cauda equina, dura matter, posterior fat layer, anterior fat layer, and L_4L_5 AF respectively. The other units' AFs were modeled with an average of about 40,000 elements per unit to reduce computational run time.

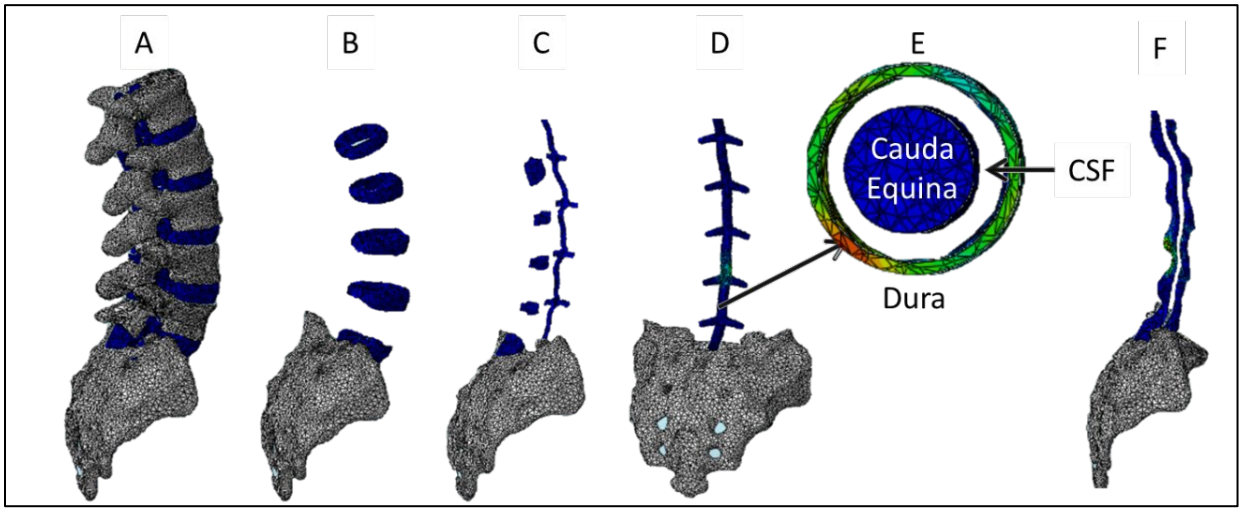

Fig. 4.3. A) Detailed lumbar spine, B) IVDs, C) Ligamentum Flavum components and posterior longitudinal ligament, D) Dura sack-like matter including the CSF and cauda equina, E) Cross-sectional area of dura showing the cauda equina and CSF cavity, and F) Anterior and posterior canal fat layers

FE material properties

The spinal canal constituents and IVDs were assigned FE material models based on studies from literature. The ligaments were assigned the isotropic hyperelastic model of Ogden with the strain energy expression given by

$$W = \sum_{i=1}^{3}\left[\frac{2\mu_i}{\alpha_i^2}\left(\lambda_1^{\alpha_i} + \lambda_2^{\alpha_i} + \lambda_3^{\alpha_i} - 3\right) + \frac{1}{D_i}(J-1)^{2i}\right] \quad (4.1)$$

where $D_i = 2/K_i$, λ_i are the stretches in the principal directions, μ_i are the shear moduli, J is the Jacobian, and K_i are the bulk moduli. The equation coefficients were used from experimental data (Xiao et al., 2011) (Table 4.1).

Table 4.1
Material model coefficients

	μ_1 (MPa)	μ_2 (MPa)	μ_3 (MPa)	α_1	α_2	α_3	D_1 (MPa^{-1})	D_2 (MPa^{-1})	D_3 (MPa^{-1})
PLL/LF	0.159	0.770	-0.39	-1.126	-18.54	-9.60	1	1	1
AF	C_{10} (MPa)		C_{20} (MPa)		C_{30} (MPa)		a_3 (MPa)		b_3
	0.0146		-0.0189		0.041		0.03		120
	End-plates	Fat	Dura	CE	Bone				NP & CSF
E (MPa)	23.80	0.48	70.00	0.003	350	Incompressible fluid,			
ν	0.40	0.50	0.50	0.50	0.25	$\rho\ (g/mm^3)$			0.001

For the annulus fibrosis, the anisotropic hyperelastic model with two families of fibers were used, where the matrix substance was modeled with the isotropic hyperelastic incompressible Yeoh material of the third order reduced polynomial with a strain energy expression of

$$W_{matrix} = C_{10}(I_1 - 3) + C_{20}(I_1 - 3)^2 + C_{30}(I_1 - 3)^3 \quad (4.2)$$

and as a function of the first invariant I_1 of the deviatoric of Cauchy-Green strain tensor C. The fibers were modeled with an exponential strain energy expression

$$W_{fiber} = \frac{a_3}{b_3}\left(e^{b_3(I_4-1)^2} + e^{b_3(I_6-1)^2} - 2\right) \quad (4.3)$$

and as a function of $I_4 = a_0 C a_0$ and $I_6 = b_0 C b_0$ the fourth and sixth invariants of the Cauchy-Green strain tensor. The constants a_0 and b_0 are the direction cosines of the two fibers families, $C = F^T F$, F is the deformation gradient, and total strain energy expression is given by

$$W = W_{matrix} + W_{fiber} \tag{4.4}$$

The equations coefficients were determined from an experimental study (Ayturk, et al., 2010) (Table 4.1). The coefficients a_3 and b_3 were used (Ayturk et al., 2010) from experimental tissue data in the circumferential and axial directions in tension and compression. The ABAQUS Fortran code "Uanisohyper" user subroutine was used to implement this model with the use of a cylindrical coordinate system and **Orient** tool. Uniform fiber angles of +/- 30º (circumferential direction) were assigned with tension only fiber constraint created in the code.

The NP was modeled as pure incompressible fluid using the **Fluid Cavity** tool in ABAQUS that applies uniform pressure on the AF and endplates boundary surfaces forming the NP space. The **Fluid Cavity** tool maintains constant volume during the deformation and computes the changes in fluid pressure necessary to maintain the constant volume; therefore, there was no geometry or FE mesh model for the NP. The fat, dura, and cauda equina were modeled with linear elastic models from the published studies of Gonzalez-Gutierrez et al. (2014), Zwirner et al. (2019), and Bartlett et al. (2020), respectively (Table 4.1). The Cerebrospinal fluid (CSF) filling the space between the dura and the cauda equina was modeled using the same **Fluid Cavity** tool in ABAQUS as pure incompressible fluid with an initial pressure of 1.76 KPa within reported ranges in literature (Bo et al., 2020).

Boundary constraints and contact for spine components

The tie constraints (full attached) were defined in ABAQUS to govern the relative attachment between PLL and IVDs, PLL and adjacent fat layer, fat layers and dura, LF and

adjacent fat layer, and AFs and the vertebrae. Similarly, tie constraints were defined between the tips of nerve root areas (on the dura and cauda equina) and the corresponding vertebrae on the same level to support the nerves and ensure they followed the spine motion. Surface contact in ABAQUS was created between PLL and vertebrae and between dura and cauda equina, which is probable during motion or canal narrowing. Careful attention was considered when choosing the master and slave surfaces and their meshes. The adjustment of the slave surface nodes was not allowed to avoid over-distortion of the elements close to the surface.

L_4 vertebrae foramen stenosis modeling

Three clinically relevant degrees of progressive stenosis of the bony vertebral foramen at the L_4 were defined from published studies (Aebli et al., 2013; Bajwa et al., 2013). That is, relative to a non-stenotic vertebral foramen, the anterior-posterior dimension of the foramen was reduced by 1.57 mm and by 2.8 mm based on clinical relevance (Fig. 4.4). The foramen region was assigned deformable bone properties (Table 4.1) and assigned arbitrary thermal expansion properties to induce the different degrees of bony stenosis in the foramen through temperature variation. The assigned temperature magnitude, as boundary condition in ABAQUS, was determined by trial and error to induce the required stenosis dimensions (Fig. 4.4).

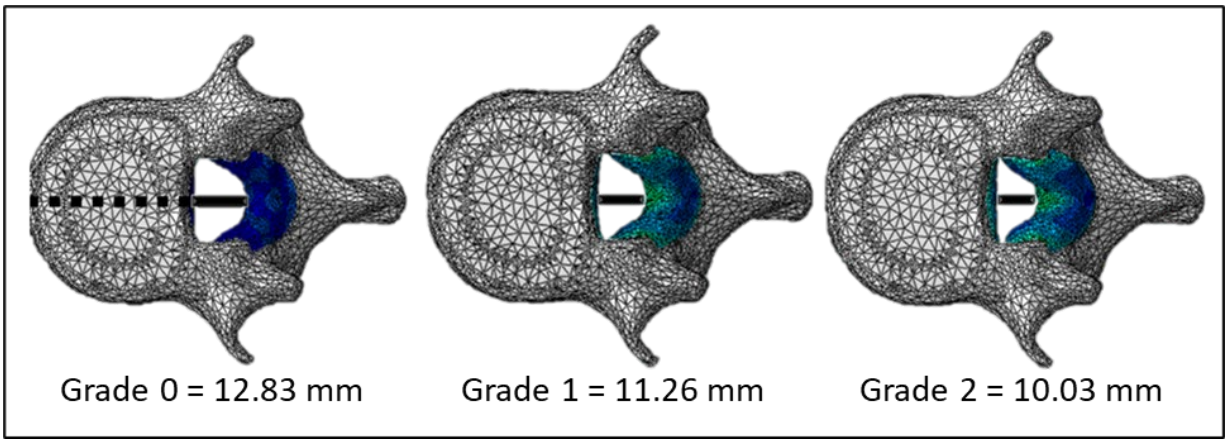

Fig. 4.4. Stenosis induced in L_4 foramen (colored) region modeled with deformable bone properties. First vertebrae on left shows the anterior-posterior vertebral body distance (VBD) (dotted line) and the spinal canal distance (SCD) (Solid line); SCD was decreased from stenosis Grade 0 (non-stenotic), Grade 1, and Grade 2 (passing critical distance)

Definitions of stenosis measures:

Several distinct measures of stenosis were defined to support the detection of the minute changes resulting from the VKS over a range of body motions (Table 4.2 and Fig. 4.5). The first three measures were detected at two transverse levels, including at the L_4 vertebral foramen level and at the center of the IVD of L_4L_5 unit level (Fig. 4.6).

Table 4.2
Definitions of stenosis measures

	Dura	Cauda equina
Anterior-posterior (outer) diameter	a	c
Transverse cross-section (elliptic) area	$\pi ab/4$	$\pi cd/4$
Transverse cross-section area aspect ratio	a/b	c/d
Cerebrospinal fluid (CSF) pressure		
Mechanical stress, strain, and pressure	The maximum magnitude in the portions of the dura and cauda equina starting, roughly, from the superior surface of the L_3L_4 IVD to the inferior surface of the L_4L_5 IVD (Fig. 4.6)	

b and d are the lateral diameters (Fig. 4.5)

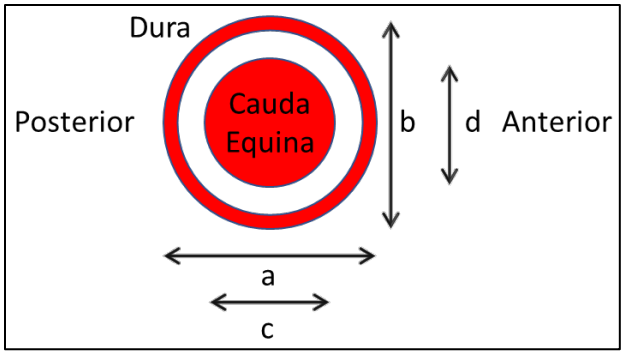

Fig. 4.5. Dimensions definitions of the dura and cauda equina

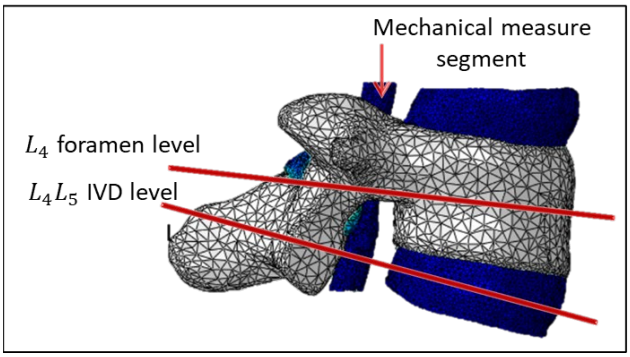

Fig. 4.6. The measuring levels for the first three stenosis measures and the dura and cauda equina segments for the mechanical measure (other canal component hidden for clarity)

The FE analysis steps

The FE simulation was conducted in three FE simulation steps, where the initial swellings in the IVDs were created in step one, the stenosis narrowing in L_4 central foramen created in step two, and the flexion motion was conducted in step three.

Step one – initial configuration step:

The 0º thorax-pelvis flexion standing posture at which the KD-FEM was mapped from the ESN MSD model was the initial posture from which the motion started. In this step, the vertebrae were held fixed at this posture during the simulation, using boundary conditions applied at the

vertebrae reference points, and the initial pressures in the IVDs and the CSF were applied to induce the bulging and initial deformations in the ligaments and other components at the standing posture.

The magnitudes of the initial pressures applied to the NP cavities were the IVD pressure predictions of the ESN MSD model at the initial standing posture and equal to 0.734, 0.938, 1.013, 0.732, and 1.416 MPa for the L_1L_2 to $L_5Sacrum$ units, respectively. The **Fluid Cavity** tool was used to apply the initial pressure for L_4L_5 IVD on the NP boundary surfaces, and the **Load** tool was used to apply the initial pressure for the other IVDs directly on the AF internal surface that forms the NP cavity; this was to lower the computational run time that the **Fluid Cavity** tool requires. An initial fluid pressure of 1.76 KPa was applied to the CSF cavity to induce pressure between the dura and cauda equina. This value was a rough estimate within the ranges reported by Bo et al. (2020).

Step two – creating stenosis in the L_4 vertebral foramen:

The vertebrae were maintained fixed at the 0° flexion standing posture for this step, and temperature magnitude were applied to the deformable bony foramen as a boundary condition to induce the central canal narrowing. The Torg-Pavlov ratio was used to set the critical anterior-posterior distance within the vertebral foramen signaling stenosis. This ratio is defined as the ratio of the spinal canal distance (SCD) to the vertebral body distance (VBD) in the anterior-posterior direction (Fig. 4.4). In this study, the stenotic Torg-Pavlov ratio for L_4 was 0.31 estimated from the study of Aebli et al. (2013) and Bajwa et al. (2013) and the critical anterior-posterior foramen distance was 11.18 mm. Three grades of foramen narrowing were modeled as shown in Fig. 4.4.

Step three – flexion motion simulation:

In this step, the VKS predicted by the ESN MSD model over the rang of 0° to -30° thorax-pelvis flexion were applied as boundary conditions to the vertebrae reference points. For the L_4L_5

unit where the stenosis measure is measured, the initial IVD pressure magnitudes changed based on the **Fluid Cavity** tool computations during motion. For the other spinal units and to lower the computation time, the initial IVD pressures applied in step two were varied linearly, over the flexion range, to the ESN pressure prediction at 30°, which were equal to 1.11, 1.29, 1.34, and 1.67 MPa for L_1L_2, L_2L_3, L_3L_4, and $L_5Sacrum$ units, respectively. The coupled KD-FEM was run for each of the three stenosis grades and the stenosis measures were computed (Figs. 4.7-10 & Table 4.3).

Results

The simulation results of the detailed lumbar canal model integrated with KD-FEM enabled the distinct computation and detection of the changes in the proposed stenosis measures, in dura and cauda equina, and the comparison between the three clinically relevant degrees or grades of progressive stenosis of the bony vertebral foramen at the L_4 level. These stenosis measures supported the detection of minute changes, at the L_4 vertebral foramen and the center of L_4L_5 IVD levels, resulting from the VKS over the body motion of 0° to -30° thorax-pelvis flexion. Fig. 4.7 shows the percent of change of the anterior-posterior (AP) diameters during flexion at L_4 or L_4L_5-IVD levels for the dura or cauda equina calculated by the general equation

$$\%\ of\ AP\ diameter\ change = \frac{D_i - D_0}{D_0} 100\% \tag{4.5}$$

where D_i is the current measured AP diameter during flexion and D_0 is the non-stenotic AP diameter at the standing initial posture.

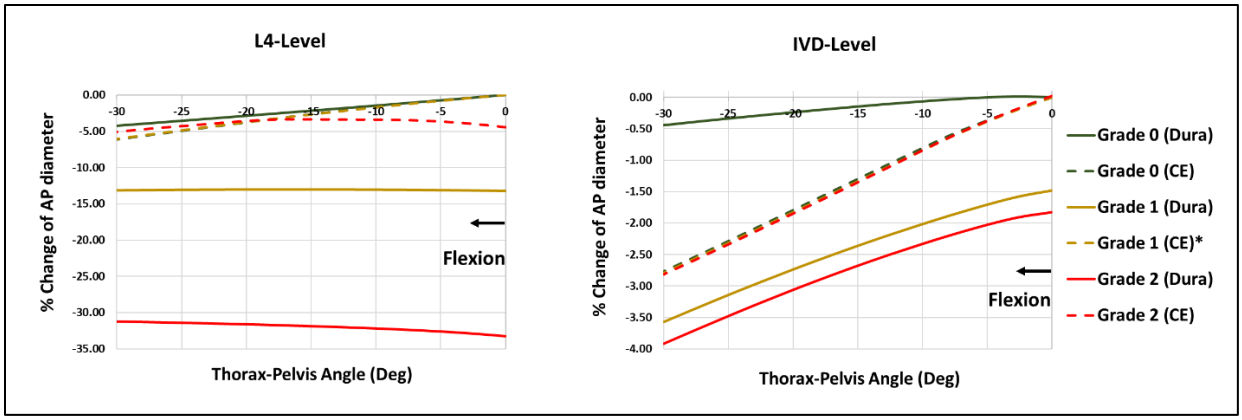

Fig. 4.7. Percent of AP diameter change relative to Grade 0 (non-stenotic) diameter at standing posture in dura and cauda equina (CE) at L_4 and L_4L_5-IVD levels.
*Curve under the green and red dotted curves

Fig. 4.8 shows the change percentage of the transverse cross-section aspect ratio during flexion at L_4 or L_4L_5-IVD levels for the dura or cauda equina calculated by the general equation

$$\%\ change\ of\ aspect\ ratio = \frac{AR_i - AR_0}{AR_0} 100\% \quad (4.6)$$

where AR_i is the current measured aspect ratio during flexion and AR_0 is the non-stenotic aspect ratio at the standing initial posture.

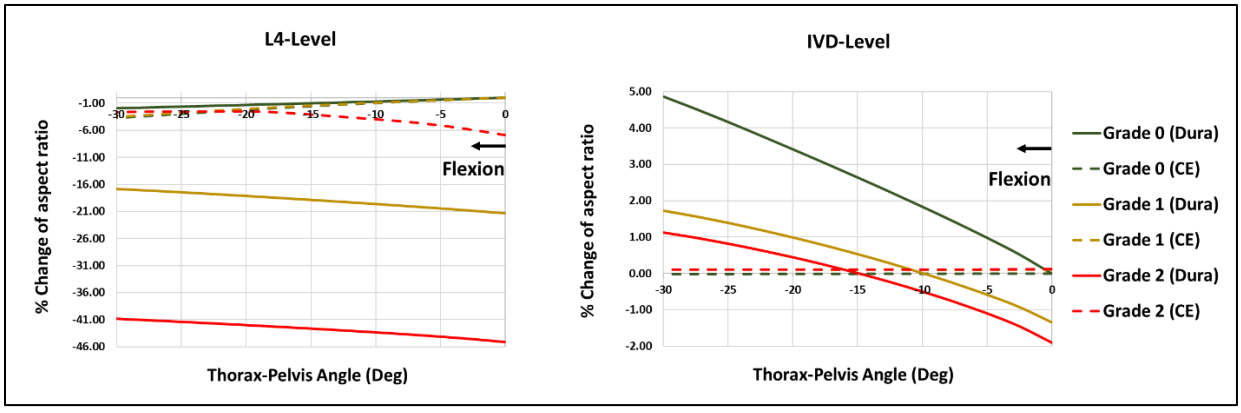

Fig. 4.8. Percent of transverse cross-section aspect ratio change relative to Grade 0 (non-stenotic) aspect ratio at standing posture in dura and cauda equina (CE) at L_4 and L_4L_5-IVD levels

Fig. 4.9 shows the change percentage of the transverse cross-sectional area during flexion at L_4 or L_4L_5-IVD levels for the dura or cauda equina calculated by the general equation

$$\%\ change\ of\ area = \frac{A_i - A_0}{A_0} 100\% \tag{4.7}$$

where A_i is the current measured area during flexion and A_0 is the non-stenotic area at the standing initial posture.

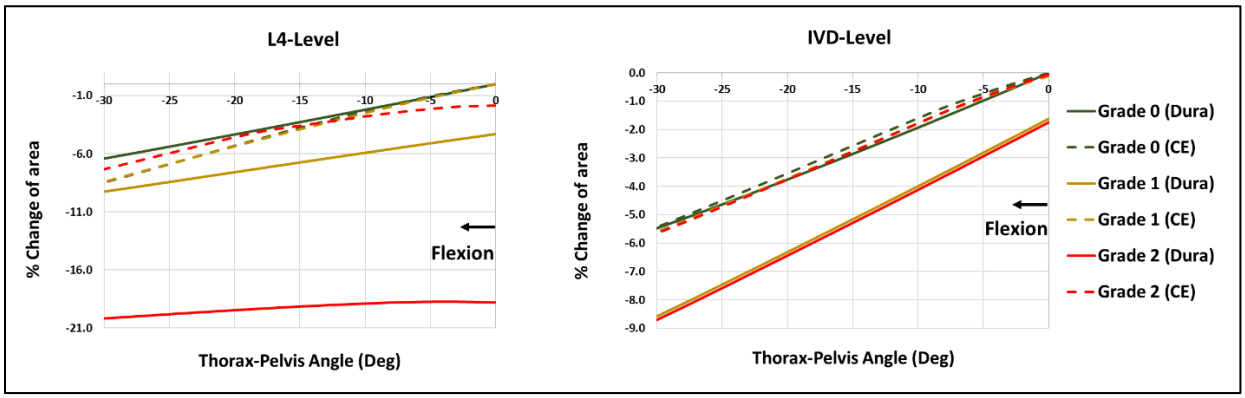

Fig. 4.9. Percent of transverse cross-sectional area change relative to Grade 0 (non-stenotic) area at standing posture in dura and cauda equina (CE) at L_4 and L_4L_5-IVD levels

The maximum logarithmic strain measure curves (Fig. 4.10) showed irregularities over the flexion motion, with the exception of the grade 2 stenosis curve for the dura, which was smooth. The grade 2 curves were at a higher strain at 0° than the other cases, increasing in magnitude in the cauda equina and decreasing in magnitude in the dura with increasing flexion. The non-stenotic and first grade curves behaved similarly in the cauda equina, whereas they were at different magnitudes at 0° in the dura and converged at larger flexion angles.

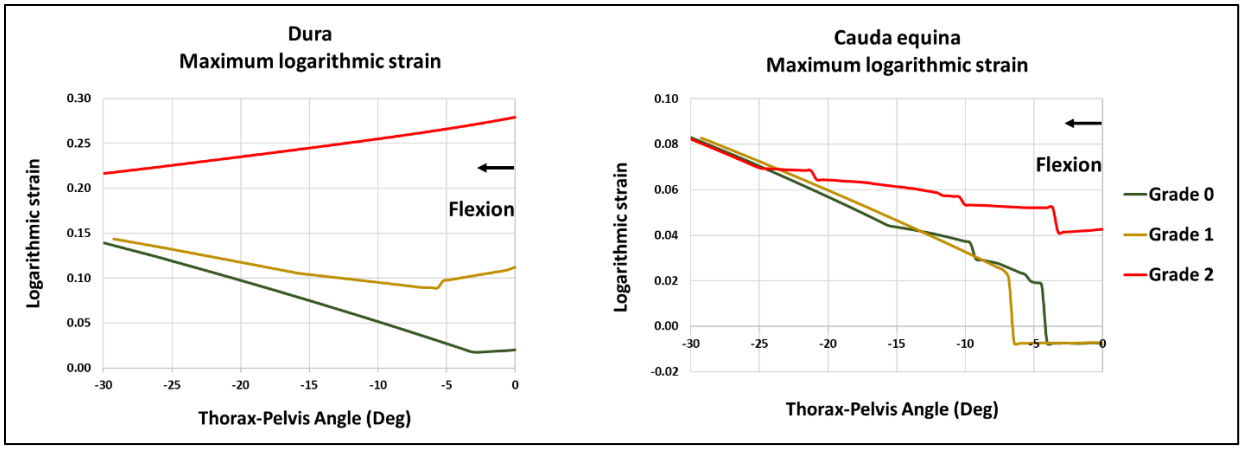

Fig. 4.10. Maximum absolute logarithmic strain variation in flexion motion

The numbers in Table 4.3 show the differences between the curves' magnitudes of Figs. 4.7-10 at the end of motion of -30° flexion and at the start of motion of 0° standing posture; the figure also shows the squares of the correlation factors for the curves over the whole range of motion which indicate the degree of linearity of the stenosis measures.

Table 4.3
Percent change difference for the stenosis measures (percent at -30° minus percent at 0°) and the square of the curves' correlation factors in brackets

	AP Diameter % & (R^2)		Aspect ratio % & (R^2)		Area % & (R^2)		Max. Log. strain	
L_4 level	Dura	CE	Dura	CE	Dura	CE	Dura	CE
Non stenotic	-4.21 (0.9998)	-6.13 (0.9948)	-1.93 (0.9988)	-3.73 (0.9922)	-6.43 (0.9999)	-8.43 (0.9959)		
Stage one	-0.11 (0.1849)	-6.02 (0.9964)	4.48 (0.9968)	-3.54 (0.9901)	-4.92 (0.9999)	-8.43 (0.9982)		
Stage two	1.98 (0.9530)	-0.62 (0.1848)	4.29 (0.9916)	4.22 (0.8236)	-1.37 (0.9355)	-7.33 (0.9602)		
IVD level								
Non stenotic	-0.44 (0.9674)	-2.77 (0.9982)	4.86 (0.9976)	-0.01 (0.9888)	-5.45 (0.9994)	-5.45 (0.9984)		
Stage one	-2.09 (0.9925)	-2.79 (0.9990)	3.07 (0.9847)	0.00 (0.2079)	-6.98 (0.9999)	-5.61 (0.9991)		
Stage two	-2.08 (0.9897)	-2.84 (0.9992)	3.04 (0.9781)	-0.02 (0.5610)	-6.95 (0.9999)	-5.65 (0.9993)		
Non stenotic							0.12	0.073
Stage one							0.03	0.073
Stage two							-0.06	0.04

Discussion and conclusions

The methods and outcomes of this study demonstrated the quantification of risks on spinal canal tissues due to vertebral kinematics and progressive canal narrowing. The study enabled the distinct computation and detection of changes in the proposed stenosis measures of the anterior-posterior diameters, transverse cross-sectional areas, transverse cross-sectional aspect ratios, the mechanical stress, strain, and pressure, cerebrospinal fluid pressure (CSF), and contact between the dura and cauda equina. The detailed canal FE model enabled the quantification and modeling of three stages of canal narrowing, and the simulation pipeline' methods enabled the integration of the canal model into the VKS driven FE model, which enabled the studying of the VKS effect on stenotic canal tissues. This study demonstrated the general applicability of the pipeline and the KD-FEM model, developed in a previous study (Jaradat et al., 2022b) (Chapter Three), and the possibility of applying the computational methods to different spine tissues, such as the spinal canal constituents.

The AP diameter results reflected physical behavior of the canal due to narrowing and motion shown in Fig. 4.7. At the initial standing posture, the results showed the followings. The dura was affected by the narrowing stages more significantly than the CE as indicated by the start of the solid yellow and red curves in both levels. This was due to the function of the CSF and its space that protect the CE from excessive stress and deformation in the canal. However, the dura was affected less at the IVD level due to the distance from the narrowed foramen, occurring at L_4-level, partially regaining its non-stenotic diameter. The CE was affected more in the second stage due to the contact between the dura and CE occurring at this stage, as indicated by the dotted red curve, however, this was less evident in the IVD level away from the contact.

During flexion motion, the stenosis measures change as the lumbar curvature, the vertebrae positions and orientations, and the contact pressures change. The lower grades of stenosis impose less restrictions on the motion and deformation of the dura and the cauda equina during motion; this resulted in less change in the AP diameter at L_4-level in grade 2 stenosis (Fig. 4.7). At the IVD level, the IVD bulging inside the foramen reduced during flexion motion as the initial IVD wedge shape angle is reduced; this led to less changes in the AP diameter compared with the L_4-level.

At standing posture, the aspect ratio results reflected similar behavior at both levels (Fig. 4.8), to the AP diameter results. During motion, the lateral diameter was reduced in the dura for all stages due to the pressure that the fat layers exert at the lateral side of the dura; this led to the increase in percent change in the aspect ratio that is calculated by division by the lateral diameter. The CE showed less change due to the CSF function. At the IVD level, the increase in dura aspect ratio was less due to the more space available for the lateral dimension far from the stenosis restrictions.

The cross-sectional area results reflected physical behavior of the canal due to narrowing and motion shown in Fig. 4.9. The curves showed decreasing trend compared with the increasing trend of the aspect ratio curves; this is due that the lateral diameter is multiplied by the AP diameter in the area calculations.

The maximum absolute strain could occur at different elements for each time step. In general, the strain increased with the motion and degree of stenosis except for the extreme case of second stage at the L_4 level, where it started at higher magnitudes but decreased in the dura, which can be caused by the reduction of IVD bulging. The mechanical measures like the strain and stress needs more deliberate insight and investigation to fully understand their behavior and location of occurrence of the maximum and its indications. In rough comparison, the maximum strain in the

cauda equina was within *in vitro* tests that reported material collapse starting at about 0.35 strain value by Nishida et al. (2015) for pig spine. Further work is needed to compare the values computed by this research methods with human *in vitro* tests in similar loading and motion conditions.

Works Cited

Aebli, N., Wicki, A. G., Rüegg, T. B., Petrou, N., Eisenlohr, H., Krebs, J. 2013. The Torg-Pavlov ratio for the prediction of acute spinal cord injury after a minor trauma to the cervical spine. Spine J;13(6):605-12.

Aiyangar, A.K., Zheng, L., Tashman, S., Anderst, W.J., Zhang, X. 2014. Capturing three-dimensional in vivo lumbar intervertebral joint kinematics using dynamic stereo-X-ray imaging. J. Biomech. Eng. 136 (1), 011004.

Anderst, W.J., West, T., Donaldson, W. F., Lee, J. Y., Kang, J. D. 2016. A Longitudinal study of the six degrees of freedom cervical spine range of motion during dynamic flexion/extension and rotation after single-level anterior arthrodesis. Spine (Phila Pa 1976). 41(22).

Ayturk, U. M., Garcia. J. J., Puttlitz, C. M. 2010. The Micromechanical Role of the Annulus Fibrosus Components Under Physiological Loading of the Lumbar Spine. Journal of Biomechanical Engineering, Vol. 132 / 061007-1.

Bajwa, N. S., Toy, J. O., Ahn N. U. 2013. Application of a correlation between the lumbar Torg ratio and the area of the spinal canal to predict lumbar stenosis: a study of 420 postmortem subjects. J Orthop Traumatol; 14(3): 207–212.

Bartlett, R. D., Eleftheriadou, D., Evans, R., Choi D., Phillips, J. B. 2020. Mechanical properties of the spinal cord and brain: Comparison with clinical-grade biomaterials for tissue engineering and regenerative medicine. Biomaterials 258 120303.

Bø, S. H., Lundqvist, C. 2020. Cerebrospinal fluid opening pressure in clinical practice – a prospective study. J Neurol; 267(12): 3696–3701.

Cheng, B., Castellvi, A. E., Davis, R. J., Lee, D. C., Lorio, M. P., Prostko, R. E. 2016. Variability in flexion extension radiographs of the lumbar spine: a comparison of uncontrolled and controlled bending. Int. J. Spine Surg. 10:20.

Costandi, S., Chopko, B., Mekhail, M., Dews, T., Mekhail, N. 2015. Lumbar spinal stenosis: therapeutic options review. Pain Pract;15(1):68-81.

Cunningham, B. W., Kotani, Y., McNulty, P. S., Cappuccino, A., McAfee, P. C. 1997. The effect of spinal destabilization and instrumentation on lumbar intradiscal pressure: an *in vitro* biomechanical analysis. Spine (Phila Pa 1976). 22(22):2655-63.

Fujii, R., Sakaura, H., Mukai, Y., Hosono, N., Ishii, T., Iwasaki, M. 2007. Kinematics of the lumbar spine in trunk rotation: in vivo three-dimensional analysis using magnetic resonance imaging. Eur. Spine J. 16, 1867–1874.

Gonzalez-Gutierrez, J., Scanlon M. G. 2014. Rheology and mechanical properties of fats. research gate, publication/245542288.

Jaradat, M. G., Harman, M. K., McHenry, T. P., Yao, H. 2022. Predicting non-constrained vertebral kinematics in musculoskeletal dynamic simulations from body-level extension-flexion motion: Validation of a reformulated lumbar spine model. Journal of Biomechanical Engineering, In Submission (a).

Jaradat, M. G., Harman, M. K., McHenry, T. P., Yao, H. 2022. Multi-Scale Pipeline of computational simulations utilizing musculoskeletal dynamics predicted vertebral kinematics in lumbar spine soft tissue analysis: Application to intervertebral disc FE analysis. Journal of Biomechanics, In Submission (b).

Kaneoka, K., Ono, K., Inami, S., Hayashi, K. 1999. Motion analysis of cervical vertebrae during whiplash loading. Spine, volume 24, number 8, pp 763-770.

Li, G., Wang, S., Passias, P., Xia, Q., Li, G., Wood, K. 2009. Segmental in vivo vertebral motion during functional human lumbar spine activities. Eur. Spine J.18, 1013–1021.

Lin, C-C., Lu, T-W., Wang, T-M., Hsu, C-Y., Hsu, S-J., Shih, T-F. 2014. In vivo three-dimensional intervertebral kinematics of the subaxial cervical spine during seated axial rotation and lateral bending via a fluoroscopy-to-CT registration approach. Journal of Biomechanics 47(2014) 3310-3317.

Manchikanti, L., Singh, V., Datta, S., Cohen, S. P., & Hirsch, J. A. 2009. Comprehensive review of epidemiology, scope, and impact of spinal pain. Pain physician, 12(4), E35-70.

Nishida, N., Kanchiku, T. Ohgi, J., Ichihara, K., Chen, X., Taguchi, T. 2015. Mechanical properties of nerve roots and rami radiculares isolated from fresh pig spinal cords. Neural Regen Res; 10(11): 1869–1873.

Panjabi, M. M. 2003. Clinical spinal instability and low back pain. Journal of electromyography and kinesiology, 13(4), 371-379.

Sato, K., Kikuchi, S., Yonezawa, T. 1999. In vivo intradiscal pressure measurement in healthy individuals and in patients with ongoing back problems. Spine 24(23):2468–74.

Schmoelz, W., Huber, J. F., Nydegger, T., Claes, L., Wilke, H. J. 2006. Influence of a dynamic stabilization system on load bearing of a bridged disc: an *in vitro* study of intradiscal pressure. Eur Spine J. 15(8):1276-85.

Schonstrom, N., Hansson, T. 1988. Pressure changes following constriction of cauda equina. An experimental study in situ. Spine (Phila Pa 1976). 13(4):385-8.

Staub, B. N., Holman, P. J., Reitman, C. A., Hipp, J. 2015. Sagittal plane lumbar intervertebral motion during seated flexion-extension radiographs of 658 asymptomatic non degenerated levels. J Neurosurg Spine 23:731–738.

Wang, H., Zhou, C., Yu, Y., Wang, C., Tsai, T.-Y., Han, C. 2020. Quantifying the ranges of relative motions of the intervertebral discs and facet joints in the normal cervical spine. J. Biomech. 112:110023.

Wang, S., Xia, Q., Passias, P., Li, W., Wood, K., and Li, G., 2011, "How Does Lumbar Degenerative Disc Disease Affect the Disc Deformation at the Cephalic Levels In Vivo?," Spine, 36(9), pp. E574–E581.

Wang, S., Xia, Q., Passias, P., Wood, K., and Li, G., 2009, "Measurement of Geometric Deformation of Lumbar Intervertebral Discs Under In-Vivo Weightbearing Condition," J. Biomech., 42(6), pp. 705–711.

Wilke, H-J., Neef, P., Caimi, M., Hoogland, T., Claes, L., 1999. New In Vivo Measurements of Pressures in the Intervertebral Disc in Daily Life. SPINE Volume 24, Number 8, pp 755–762, 1999.

Wilke, H-J., Neef, P., Hinz, B., Seidel, H., Claes, L., 2001. Intradiscal Pressure Together with Anthropometric Data – A Data Set for Validation of Models". Clinical biomechanics 16 supplement No. 1 (2001) S111-S126.

Willén J., Danielson, B., Gaulitz A., Niklason, T., Schönström, N., Hansson, T. 1997. Dynamic effects on the lumbar spinal canal: axially loaded CT-myelography and MRI in patients with sciatica and/or neurogenic claudication. Spine (Phila Pa 1976); 22(24):2968-76.

Xiao, Z., Wang, L., Gong, H., Zhu, D., Zhang, X. 2011. A non-linear finite element model of human L4-L5 lumbar spinal segment with three-dimensional solid element ligaments. Theoretical and applied mechanics letters 1, 064001.

Yeager, M. S., Cook, D. J., Cheng, B. C. 2013. Reliability of computer-assisted lumbar intervertebral measurements using a novel vertebral motion analysis system. Spine J. 14(2):274-81.

Zwirner, J., Scholze, M., Waddell, J. N., Ondruschka, B., Hammer, N. 2019. Mechanical Properties of Human Dura Mater in Tension – An Analysis at an Age Range of 2 to 94 Years Johann. Scientific Reports 9:16655.

CHAPTER FIVE

CONTRIBUTIONS AND CONCLUSIONS

This dissertation addressed the technical gap that simulations of body-level motions have proven inadequate for understanding organ-level behavior of the spine, such as individual VKS and IVD pressure, or predicting stenosis risks. The broad objective of this dissertation research was to develop an analytical tool for understanding spine tissues' behavior in response to VKS and spine pathology over a range of body postures. It proposed, developed, and demonstrated a novel pipeline of computational models based on the prediction of individual VKS from measurable body-level motions, using MSD simulations to drive the vertebrae in corresponding spine FE models. This objective was achieved by accomplishing the following three aims.

Aim 1

In Aim 1, a reformulated elastic surface node (ESN) lumbar model was developed for use in MSD simulations. The ESN MSD model modified the lumbar spine in an existing MSD model by removing non-physiological kinematic constraints and including elastic IVD behavior. Two lumbar spine models were compared: i) the default joint and rhythm (DJR) MSD model that was included in the standard full-body MSD model; and ii) the ESN MSD model that was reformulated from the DJR MSD model to address the technical parameters limiting VKS and IVD pressure calculations. Both the DJR and ESN MSD models were scaled using subject-specific anthropometrics and were validated to predict published *in vivo* VKS and IVD pressures in the lumbar spine during trunk flexion/extension. The reformulated ESN MSD lumbar spine model supported prediction of VKS and IVD pressures during dynamic motion and has potential for identifying biomechanical factors contributing to abnormal IVD pressures and clinical instability.

Aim 2

In Aim 2, the subject-specific ESN MSD model of the lumbar spine was integrated into a novel simulation pipeline that automatically maps it to a kinematics-driven FE model (KD-FEM). The KD-FEM consists of the lumbar vertebrae that were scaled to the subject-specific geometries and actuated by the subject-specific vertebral kinematics from the ESN MSD model for different activities. The work in Aim 2 utilized the ESN MSD model and the predicted individual VKS and IVD pressure in spine soft tissue FE modeling to further understanding of the tissues' behavior during motion. The key outcome of this work was to establish a novel pipeline of simulations, 3D modeling, and scripting tools, to automatically map the subject-specific ESN MSD lumbar model into an equivalent kinematics-driven FE model (KD-FEM). The KD-FEM consisted of the lumbar vertebrae that are scaled to the subject-specific geometries and actuated by the individual VKS from the ESN MSD model for different activities. This approach was in contrast with the common methods of assessing spine tissues behavior using load-driven FE models. The simulation pipeline was validated for its ability to predict *in vivo*, subject-specific IVD pressures at the L4-L5 vertebral level during flexion motion and load carrying postures. That is, IVD pressures calculated in the subject-specific KD-FEM combined with the ESN MSD lumbar spine model developed in Aim 1 were compared to: i) *in vivo* IVD pressure measurements from a published study; and ii) IVD pressure calculations from a subject-specific default MSD model that included body-level motion inputs from an *in vivo* motion capture study of different activities.

Aim 3

In Aim 3, a detailed multi-layered multi-phase lumbar canal FE model was integrated into the KD-FEM to quantify risks to spinal canal tissues due to VKS and progressive canal narrowing (stenosis). This approach contrasts with commonly oversimplified canal models in literature. This

approach enabled distinct computation of proposed stenosis measures: cerebrospinal fluid pressure, cauda equina deformation and related stresses/pressure/strains, and dura-equina contact, Model outputs included the stenosis measures during trunk flexion motion and comparison of three clinically relevant degrees of progressive stenosis of the bony vertebral foramen at the L4 level.

The technical aspects of this dissertation presented a versatile computational modeling tool that provided an alternative approach for computing individual VKS during dynamic body-level motions. It generated analytical assessments representing spine soft tissue pathology and enabled dynamic quantification of risks during motion. It validated the use of MSD systems for computing realistic VKS from body-level motions, using them to actuate FE models of the lumbar spine, and capturing the impact of pathological conditions like progressive stenosis. In future work, algorithms representing specific tissues can be embedded into the KD-FEM pipeline, such as IVD models or detailed canal geometry, which functioned as an independent approach for evaluating those models under load and motion conditions with realistic VKS.

The broader innovation of this dissertation was its potential for identifying biomechanical factors contributing to clinical instability, abnormal intervertebral disc pressures, and risks due to abnormal vertebral kinematics and progressive stenosis. The simulation pipeline was intended to be coupled with traditional symptoms-based clinical assessments. In future work, the simulation pipeline can be generalized for a larger variety of body types and daily activities and validated for robust application in a clinical work frame. Implementation would require only minimal patient inputs of simple anthropometrics measurements, rudimentary vertebral geometries from available clinical radiographs or MRI scans, and simple motion captured postures or ranges of motion. In this manner, it has potential to aid patient education related to activity precautions and support decisions for treatment options.